Modeling Audio Circuits Containing Typical Nonlinear Components with Wave Digital Filters

Ólafur Bogason

Department of Music Research
Schulich School of Music
McGill University
Montreal, Canada

April 2018

A thesis submitted to McGill University in partial fulfillment of the requirements of the degree of Master of Arts

Abstract

Musicians and audio producers like vintage audio gear and for good reasons. The most beloved songs and sounds of the past were made on gear that now has become vintage. Examples of such gear are guitar pedals and amplifiers used by Jimi Hendrix (e.g., the Arbiter Fuzz Face) and the Mini-Moog synthesizer used by numerous artists since its debut in 1969. Unfortunately vintage gear is often expensive, hard to come by, impractical to transport and difficult to maintain.

In order to replicate audio circuits that produce the sounds that vintage gear is famous for, multiple techniques from both industry and academia exist. Most techniques result in a model derived from the audio circuit. The field centered around modeling analog audio gear, in particular audio circuits, is called virtual analog.

Simulating audio circuits tends to have further constraints than the generic simulation of electronic circuits. Constraints include the need for real-time user input and simulation. Wave digital filters, originally intended for the design of digital filters, have received growing attention by the virtual analog research community because they deal elegantly with the aforementioned design restrictions.

A brief overview of the state of the art in virtual analog research is provided along with context on wave digital filters as applied to virtual analog modeling. Behavior of wave digital filters under time-varying conditions is studied and three nonlinear components commonly found in audio circuits are introduced into the formalism. By modeling larger, nontrivial audio circuits the newly derived models are applied in a realistic context. Simulations are compared to tried-and-true generic circuit simulation software.

Résumé

Les musiciens et les producteurs audio aiment le matériel audio vintage pour de bonnes raisons. Les chansons et les sons les plus appréciés du passé ont été réalisés sur des appareils qui sont devenus des pièces de musée. Des exemples de ces dispositifs sont les pédales de guitare et les amplificateurs utilisés par Jimi Hendrix (par exemple, l'Arbiter Fuzz Face) et le synthétiseur Mini-Moog utilisé par de nombreux artistes depuis ses débuts en 1969. Malheureusement, les appareils d'époque sont souvent coûteux, difficiles à trouver, peu pratiques à transporter et difficiles à entretenir.

Afin de simuler les circuits audio qui produisent les sons réputés des dispositifs 'vintage' de nombreuses techniques de l'industrie et du milieu universitaire existent. La plupart de ces techniques produisent un modèle dérivé du circuit audio. Le champ d'étude centré autour de la modélisation d'équipements audio analogiques, en particulier des circuits audio, est appelé "analogique virtuel".

La simulation de circuits audio tend à obeir à d'autres contraintes que la simulation générique de circuits électroniques. Les contraintes incluent la nécessité d'une entrée utilisateur en ligne et d'une simulation en temps réel. Le WDF (Wave Digital Filter), initialement destiné à la conception de filtres numériques, a reçu l'attention croissante de la communauté virtuelle de recherche analogique parce qu'il traite élégamment les restrictions conceptuelles susmentionnées.

Un bref aperçu de l'état de l'art en recherche analogique virtuelle est fourni avec une mise en contexte des WDF appliqués à la modélisation analogique virtuelle. Le comportement des WDF dans des conditions variant dans le temps est étudié et trois composants non linéaires généralement présents dans les circuits audio sont introduits dans le formalisme. En modélisant des circuits audio non triviaux plus grands, les modèles nouvellement établis sont appliqués dans un contexte réaliste. Les simulations sont comparées à celles du logiciel de simulation de circuit générique SPICE.

Acknowledgments

First I wish to thank my supervisor Dr. Philippe Depalle for his support, great humor and encouragement throughout my studies at McGill. At the same time I gratefully acknowledge McGill University and the Schulich School of Music for their financial aid.

A special acknowledgment goes out to Dr. Kurt James Werner. Both for having supplied me with tools needed to plot WDF schematics and provided many useful comments and suggestions during the development of this manuscript. We also shared a paper at DAFx17 on a topic that sprung from research of this thesis.

I extend my sincere gratitude to the faculty and peers at the music technology department at McGill. I would also like to thank my roommates at the "Heart of the Plateau" and my friends and colleagues at Genki Instruments for uplifting yet maturing times during the arduous writing period.

Last, but most importantly, I wish to thank my family, in particular my loving parents, Bogi Þór Siguroddsson and Linda Björk Ólafsdóttir, for all their support and encouragement.

Contents

List of Figures

List of Tables

List of Acronyms

ABC	Amplifier bias current
AC	Alternating current
APD	Anti-parallel diodes
BE	Backward Euler
BJT	Bipolar junction transistor
BLT	Bilinear transform
CMOS	Complementary metal oxide semiconductor
DC	Direct current
DSP	Digital signal processing
FE	Forward Euler
FET	Field effect transistor
IGFET	Insulated-gate field-effect transistor
JFET	Junction field effect transistor
KCL	Kirchoff's current law
KVL	Kirchoff's voltage law
LTI	Linear time-invariant (system)
MNA	Modified nodal analysis
MOSFET	Metal-oxide semiconductor field effect transistor
NSI	Nonlinear system identification
ODE	Ordinary differential equation
OTA	Operational transconductance amplifier
RC	Resistor-Capacitor
SISO	Single-input, single-output
SPICE	Simulation program with integrated circuit emphasis

VA	Virtual analog
VCCS	Voltage controlled current source
WDF	Wave digital filter

List of Notations

a_i	Incident wave at i-th port
b_i	Reflected wave at i-th port
H_i	Kirchoff-domain transfer function at i-th port
i_i	Current at i-th port
I	Identity matrix
R_i	Port-resistance at i-th port
$\mathbf{S}$	Scattering matrix
S_i	Reflectance at i-th port
v_i	Voltage at i-th port.
v_{source}	Voltage source. Lower-case used for signal sources.
V_{source}	Voltage source. Upper-case used for constant (DC) sources.
$\Phi_{\mathcal{S}_n}$	n-port series adaptor
$\Phi_{\mathcal{P}_n}$	n-port parallel adaptor

Chapter 1

Introduction

1.1 Context

The most beloved songs and sounds of the past were made on gear that now has become vintage. Vintage gear tends not only to be expensive and hard to come by, but also impractical to transport, difficult to maintain and does not fit into a modern workflow. Recent years have seen a sustained interest from musicians and producers to have access to tools that produce similar sounds to the ones vintage gear is famous for. In order to replicate the sounds, multiple techniques, from both industry and academia, have been proposed.

The end result is most often a piece of software that is portable, inexpensive to maintain and becoming progressively capable of producing sounds that are similar or identical to the gear it attempts to replicate. The field centered around modeling analog audio gear, in particular audio circuits, is termed Virtual Analog (VA). Example of research carried out by VA researchers include the modeling of guitar effect pedals [1–9], guitar pickups [10], guitar amplifiers [11–15], synthesizer filters [16–19], source signal generators [20, 21] and electro-mechanical systems [22, 23]. Further examples can be found in recent review articles on the topic [24–27].

In this thesis we focus our attention on audio circuits and how to model and simulate them accurately. Audio circuits are simply electronic circuits where the information being processed is sound. Electronic circuits, as viewed from the perspective of circuit theory, encode one-dimensional algebraic nonlinear integro-differential equations. As no general-

izable closed-form solutions exist for such grouped equations, electronic circuits have been used in the past to solve them. Devices that consist of circuits used to solve equations with no direct analytical solution are commonly known as "analog computers" [28].

There is a large body of knowledge on how to derive dynamical analogies between electronic circuits and other lumped physical systems, such as acoustic or mechanical ones [29, 30]. The theory of electrical circuits, circuit theory, is quite mature [31] and so transforming other lumped physical systems into electric circuits may yield valuable insight. Once in the electronic circuit domain, the system may be analyzed using the advanced theoretical tools that have been developed in circuit theory. Furthermore, the process of modeling a multiphysics system, such as a loudspeaker can be simplified if a system is modeled in its entirety within a single domain [32].

The numerical simulation of electronic circuits has been in active research since at least the early 1970s [33]. Owing to the importance of interactive user control and real-time performance, the simulation of audio circuits by use of numerical methods poses further restrictions on the generic method of circuit simulation [34]. A crucial part of most generic circuit solvers, such as SPICE, is the varying time-step mechanism that in and of itself hinders real-time deterministic simulations of audio circuits.

Because it deals elegantly with the aforementioned complexities and restrictions, the wave digital filter (WDF) formalism [35] has received growing attention by the VA research community, e.g., [12, 25, 36–47]. WDFs were however not intended for the modeling of audio circuits and several restrictions in applying the formalism to general audio circuits have previously been identified [25]. The most inhibiting ones were the inability to model circuits whose topology is not separable into series and/or parallel connections, e.g., the Sallen-Key filter [48] or the Fender Bassman tonestack [49], and the lack of generalized techniques to model circuits containing multiple nonlinearities. Nonlinear components are widely regarded as pieces within audio circuits that form the distinctive sound they produce [50]. The practical usefulness of a circuit modeling framework that is unable to handle multiple nonlinearities is thus limited.

By incorporating modified nodal analysis (MNA) from circuit theory [51] recent work

has made simulating linear circuits of arbitrary topologies using WDF techniques possible [44]. Leveraging results from that work, a systematized method for handling multiple multi-port nonlinearities has been proposed as well [43]. Collectively these two theoretical advancements allow us to consider the proposed research.

1.2 Contributions

An overview of VA research is presented with an emphasis on current research trends in WDFs and nonlinear system identification (NSI) [52]. NSI belongs to a family of signal processing techniques that formulate a representation of systems (e.g., guitar pedal) given only input–output signal pairs and no direct physical description. This family of techniques is adequate for modeling audio gear when it is composed of a large number of elements or if the equations describing the underlying physics are not readily available. NSI has been applied to a wide variety of virtual analog modeling problems, such as loudspeaker emulation [53], audio circuit emulation [18, 50, 54] and guitar pickup modeling [10]. Comparing WDF and NSI provides us with a broader understanding of the different techniques used to model analog audio equipment.

The original contributions of this thesis can be broadly separated into three parts. Namely we study the modeling and simulation of time-varying systems using WDFs. What follows is an introduction of nonlinear components commonly found in audio circuits into the formalism. Building upon these developments we derive WDF structures for three circuits that contain nonlinear component hitherto not simulated using the formalism.

1.2.1 Simulating Time-Varying Systems using Wave Digital Filters

Similar to classical network theory [55], traditional WDF theory assumes that the system being modeled (circuit) is studied under linear time-invariant (LTI) conditions. Since musicians frequently interact with their devices, for example by turning knobs and switches, the LTI assumption is almost never met when modeling audio circuits.

To stimulate the discussion a WDF simulation of a trivial RC circuit, with varying resistance, is carried out. It is shown that the simulation becomes highly inaccurate if standard

WDF theory is followed blindly. Modeling linear circuits under time-varying conditions follows with an emphasis on concepts such as passivity, stability, WDF-specific design choices and discretization of lumped systems with highly-damped poles [56].

1.2.2 Common Nonlinearities

Three nonlinear components commonly found in audio circuits are reviewed, and details on how to incorporate them within the WDF formalism provided. The nonlinear components include the Zener diode (§4.1) and a family of field-effect transistors (FETs) (§4.2). Linear behavioral models of the operational transconductance amplifier (OTA) are provided along with a nonlinear extension in order to model the characteristic clipping of OTAs (§4.3).

1.2.3 Case Studies

By using the WDFs formalism to model larger, nontrivial audio circuits we get an opportunity to apply the derived nonlinear models in a realistic context. The FET Booster in §5.1 acts as our first foray into modeling audio circuits using WDFs. The circuit contains a JFET transistor, a three-terminal nonlinear device which we model as a two-port component within the resulting WDF structure [45]. The auto-wah/temporal envelope filter in §5.2 contains multiple nonlinearities, such as OTAs, operational amplifiers, diodes and bipolar junction transistors (BJTs). The importance of choosing a suitable numerical discretization scheme becomes apparent when modeling the section of the circuit that implements the temporal envelope tracking. In that section two diodes operate as switches. That configuration is known to cause highly inaccurate simulations when discretized using the standard discretization scheme employed in WDFs [56]. In the third and final case study we model the filter circuit of the venerable Korg MS-20 synthesizer [57] (§5.3). The circuit contains multiple nonlinearities, including operational amplifiers, OTAs and diodes. For all the case studies we compare simulations of the derived WDFs to results obtained from the ubiquitous circuit simulation software SPICE (Appendix C).

1.3 Structure of the Thesis

Chapter 2 presents a review of the relevant background literature, current trends in VA research and provides a brief overview of the theory behind WDFs and its recent developments. In Chapter 3 time-variant conditions are discussed in the context of WDFs. Chapter 4 proposes models of a Zener diode, the FET family of transistors and a nonlinear behavioral model of an OTA. Several case studies are conducted in Chapter 5 and Chapter 6 discusses potential research directions and concludes.

In Appendix §A we derive Kirchoff's voltage and current laws, discuss similarities between lumped dynamical systems and outline popular numerical schemes and s-to-z-plane mappings. Classic WDF building blocks, required to simulate common audio circuits, such as the ones modeled in this thesis, are listed in Appendix §B. The essential algorithm behind the ubiquitous circuit simulation software SPICE is briefly discussed in Appendix §C while Appendix §D provides links to calculations related to Chapter 5.

Chapter 2

State of the Art

2.1 Virtual Analog

Recent years have seen sustained interest by musicians, producers and artists in digital models of analog music equipment and instruments. This interest is partly driven by the desire to have tools that fit into a modern workflow and at the same time replicate the sought after sounds of expensive analog audio equipment.

Released in 1994 by the Swedish music technology company Clavia, Nord Lead was the first commercial product to advertise *virtual analog synthesis* [58]. Ever since then virtual analog, or VA, has been a key selling point for many commercial products, as well as an active area of research within the field of music technology.

2.1.1 Goals of Virtual Analog Research

In [23] Parker proposed that VA research can be thought of as addressing three main goals

1. Emulation – to produce exact digital copies of particular analog systems.
2. Artifact reduction – to produce digital sound processing or generation blocks that behave like their ideal continuous-time equivalents. This is achieved by reducing or eliminating the undesirable side-effects of digital signal processing, such as aliasing or frequency warping in s-to-z-plane mappings (§A.3).

3. Analog feel – to produce techniques or structures that bring some complexity, unpredictability and emergence of behaviors from the analog realm into digital systems.

In this thesis we concentrate on emulating audio circuits. Electronic circuits are commonly represented by *(circuit) schematics*. Schematics indicate how components are interconnected and provide information regarding the operating conditions a circuit is subject to. The networks that indicate how components are connected together are also known as the *topology* of the circuit. When analyzing schematics, components are commonly idealized as *lumped element models* (§A.1). While nonlinear components, such as diodes and transistors, are known to heavily influence the characteristic sounds produced by audio devices, nonidealities (linear and/or nonlinear) in real-world devices have also been shown to affect their resulting sound [50].

In order to evaluate the quality of the derived digital model, comparing simulations to an actual analog device should be carried out whenever possible. Accurately modeling all nonidealities and nonlinearities of real-world audio circuits requires access to the original audio device, which may be difficult and/or expensive to obtain. Given that researchers have access to a particular device, the comparison itself is no easy task. To limit the complexity in the comparison phase VA researchers generally assess the quality of their models by comparing simulations to the tried-and-true circuit simulation software SPICE (§C).

We compare simulations of derived WDF models to the same circuits simulated using SPICE. In practice, further treatment, such as measurement of individual components and/or listening tests are often necessary to accurately model individual audio circuits.

2.1.2 Methods of Virtual Analog Research

Most real-world audio gear is made up of highly-coupled nonlinear systems. Forming an accurate mathematical model of such systems poses substantial research challenges. Virtual analog engineers use a plethora of ad hoc and systematic modeling techniques that can be separated into two broad groups. “Black box” modeling aims to mimic the behavior of a reference system without making assumptions about its behavior while “white box” modeling approaches form mathematical models by directly exploiting the structure and

physics of a given system. “Grey box” approaches also exist, which as the name suggests, combine the two [9, 12].

2.1.3 Black Box Modeling

Methods that belong to the class of black box approaches in VA modeling aim to mimic the behavior of a reference system, such as an analog circuit as closely as possible without making any assumptions on its inner workings. Among the approaches that have been proposed in the literature include amplitude-dependent convolution methods [59, 60], efficient, accurate and alias-free source signal generators [16, 61, 62] and nonlinear system identification.

Nonlinear System Identification

Linear time-invariant (LTI) systems are completely characterized by a single impulse response h. The output of the system is then obtained by convolving the impulse response with a given input x

$$y(t) = (h * x)(t) = \int_{-\infty}^{+\infty} h(\tau)x(t-\tau)d\tau \tag{2.1}$$

To completely characterize systems that are nonlinear time-invariant one needs an infinite series of multi-dimensional impulse responses

$$y(t) = \sum_{m=0}^{+\infty} F_{\mathrm{m}}[x](t) \tag{2.2}$$

where F_{m} are functionals (functions of functions) defined as

$$F_0[x](t) = h_0, \tag{2.3}$$

$$F_i[x](t) = \int_{\tau_1} \cdots \int_{\tau_i} h_i(\tau_1, \ldots, \tau_i)\, x(t-\tau_1) \cdots x(t-\tau_i)\, d\tau_1 \cdots d\tau_i \quad i > 0. \tag{2.4}$$

$h_m : (\tau_1, \ldots, \tau_m) \mapsto (\tau_1, \ldots, \tau_m)$ is a m-variable function called the mth-order Volterra kernel [50]. First approaches of nonlinear system modeling were derived from the work of Vito Volterra in the 19th century who proved that equation (2.2) indeed fully characterizes

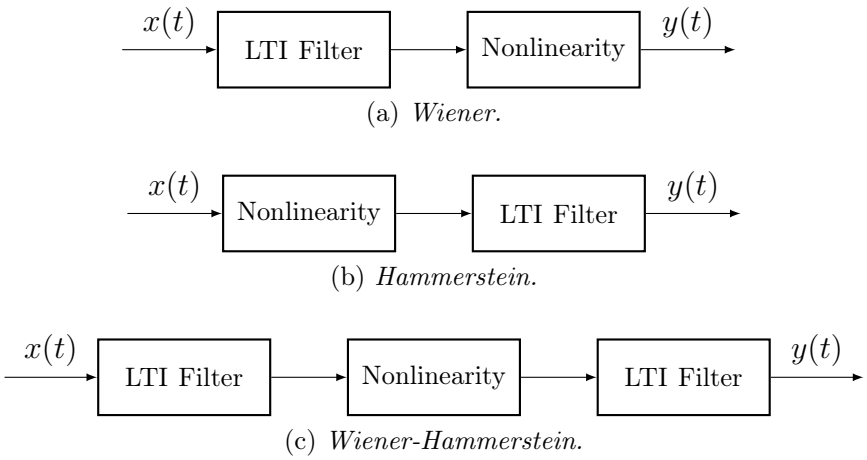

(a) *Wiener.*

(b) *Hammerstein.*

(c) *Wiener-Hammerstein.*

Figure 2.1 *Example of Block-Based Models*

a nonlinear time-invariant system.

Models based directly on the Volterra series are not common in practice. Not only do they contain prohibitively many parameters to describe a reference system but the computational complexity due to the multi-dimensional nature of the impulse responses increases exponentially with number of kernels. Common simplifications include truncating the infinite series to a finite length and having the memory of the kernels (length in time) finite.

Today, most nonlinear system identification problems reduce to (a) choose appropriate discrete model of a simplified Volterra series and (b) employ some model identification method to extract the Volterra kernels/system parameters.

Block-Based Models

Various truncated versions of the Volterra series have been proposed in the literature. These truncated versions have been collectively termed "block-based models". Such models are constructed by using some combination of LTI filters (memory linear blocks) and nonlinear algebraic functions (memoryless nonlinear blocks). Research into nonlinear system modeling has been ongoing since the 1950s. Norbert Wiener was one of the first to specifically study the problem of parameter estimation of nonlinear systems as applied to the Volterra

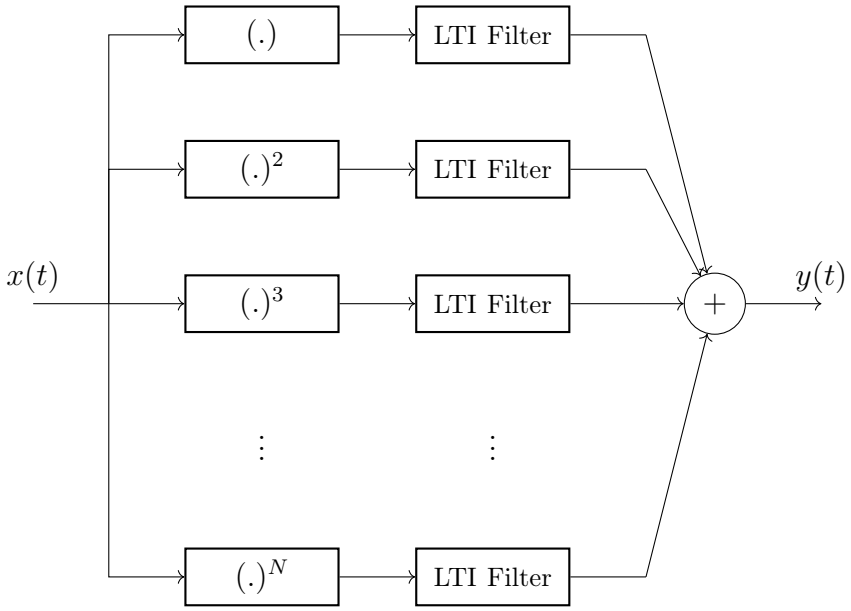

Figure 2.2 *Generalized Hammerstein Model*

series [63]. Wiener approximated the Volterra series as a cascade of a memoryless nonlinear block and a LTI filter (Fig 2.1a).

Other examples of block-based models include the Hammerstein model which swaps the LTI filter and nonlinear analytic function (Figure 2.1b) and the Wiener-Hammerstein model which is a Wiener model cascaded with an additional LTI filter (Figure 2.1c). The generalized (polynomial) Hammerstein is a block-based model that is a summation of several parallel Hammerstein models (Figure 2.2). Block-based models with feedback have also been studied in the literature [52]. A mathematical treatment on the type of systems one can expect to accurately approximate using finite Volterra series (and simplifications) is vigorously studied by Boyd and Chua in [64].

Identification Methods

Once a suitable nonlinear model based on the Volterra kernels or block-based representation has been chosen, the problem reduces to estimating the kernels/parameters of the nonlinear system. This is traditionally done by exciting the system using some known excitation signal, such as an impulse train [52], chirp [65] or random signals [66]. The corresponding

output is recorded and an adequate mathematical framework is employed to derive the kernels/system parameters from the input–output pair.

Nowadays the most widespread identification methods are based on correlation [52]. These methods have been extended to multiple-input, multiple-output systems. Drawbacks related to the estimation of power and cross-spectral densities limit their accuracy in practice [50].

A promising method that sidesteps the issues related to the estimation of power densities has been proposed by Farina and his collaborators [65, 67]. The method is based on a logarithmic swept-sine excitation and deconvolution to extract higher-order impulse responses of each distortion order. The nonlinear model used is the generalized/polynomial Hammerstein block-based model. The swept-sine identification method has been explored in more detail by Novak and others [68–70].

Nonlinear System Identification in Virtual Analog Modeling

Nonlinear system identification has been applied widely in a musical setting such as in the modeling of weakly nonlinear audio systems [71], the modeling of loudspeakers [53], the simulation of synthesizer filter circuits [18, 50, 54], guitar effects [1, 72, 73], guitar pickups [10] and guitar amplifiers [12, 74]. Custom algorithms based on block-based models with a dedicated adaptable nonlinear section have also been proposed [7, 75].

NSI methods can be very powerful when modeling audio systems that have no obvious physical model available or they are considered too complex. Virtually all nonlinear time-invariant systems can be modeled if sufficient orders of distortion coefficients (number of Volterra kernels) are chosen. The block-based models are well suited for modeling systems whose nonlinear subsystems can be identified and separated from the linear part.

Notwithstanding the prospects of being able to fully characterize a dynamic nonlinear system using mere input–output signal pairs, characterizing time-varying systems using NSI is largely an unsolved problem. Since the vast majority of audio circuits are in fact time-varying, NSI techniques are only truly applicable in cases where time-invariance is an

accurate assumption, e.g., when emulating a guitar pickup [10]. Limiting the computational complexity is also an enduring problem since the number of parameters grows exponentially with distortion terms [50].

2.1.4 White Box Modeling

White box modeling is a set of techniques that aim to exploit the structure and physics of a system when deriving a digital model. Because such methods result in models that are based on the physics of a given reference system, white box modeling is also referred to as "physical modeling".

The most trivial white box modeling technique is based on the direct discretization of a transfer function [49, 76, 77]. As is well known in engineering, the transfer function representation assumes LTI and zero initial states [78] (§A.2) and merely encapsulates a global view from input to output. After a transfer function is digitized the conservation of energy and stability of the resulting digital filter is not generally guaranteed in the time-varying case [79, 80]. Since most audio gear has to be modeled as time-varying systems, the intrinsic limitations of transfer function based approaches have inspired the research community to look for novel methods.

Today, various frameworks and paradigms exist to deal with the solution of the derived algebraic differential equations. The state space formalism from control engineering [81] is currently the most prominent systematic modeling paradigm within VA modeling.

State-space Modeling

First attempts to apply the state space formalism from control theory in a musical setting came from early sound synthesis work [82]. In that work the authors understood the potential physical modeling approaches have when applied in sound synthesis applications. Namely robustness under time-variance and improved simulation accuracy when compared to other methods. Examples of the state-space approach as applied in a musical context include applications to wind instruments [83] and guitar effects [3, 12, 84]

The nodal DK is a systematic method to derive nonlinear state-space systems from circuit schematics [85, 86]. The method applies time-discretization to reactive elements after which a state-space system is populated using modified nodal analysis (MNA) [51]. Nonlinearities are treated as dependent current sources. The nodal DK method has been applied, with some extensions, to the simulation of a time-varying guitar effect pedals [4,87] and guitar preamp [5].

In [88] Holters and Zölzer pointed out the intrinsic limitations of the nodal DK approach. Specifically that every node in the circuit has to be connected, nodes cannot connect to nonlinearities alone and that not all electrical elements may be represented as current sources. They proposed a generalized modeling framework that sidesteps the limitations of the nodal DK method. Instead of the MNA an analysis technique similar to the sparse tableau approach is applied [89], after which the derived system equations are discretized. The caveat is an increase in matrix size/computational cost compared to the nodal DK method. As is often the case in engineering, the nonlinear part of the state-space representation is either solved using iterative solvers or table lookup.

Port-Hamiltonian Approach

Another versatile framework for virtual analog modeling is the port-Hamiltonian approach. It offers a systematic way of analysis, control and simulation of complex physical systems [90].

The approach is centered around the modeling of source components, energy storage components, dissipative components and their interconnections. Differential algebraic equations are commonly represented by a port-Hamiltonian system, a state-space like representation of a physical system according to its internal energy flow. Due to the emphasis on flow of energy and its conservation, the port-Hamiltonian formalism (if applied properly) insures power balance and thus passivity in continuous-time. The continuous-time port-Hamiltonian system can be discretized using either explicit or implicit numerical schemes that guarantee passivity and thus stability in the digital realm. Recent publication explores the use of an ad hoc second-order numerical scheme that digitizes the Hamiltonian gradient

and results in an accurate, guaranteed-passive simulation [91].

In the context of VA modeling, Falaize and his collaborators have used the port-Hamiltonian approach to model parts of electro-mechanical pianos [92, 93], guitar effect pedals [94, 95] and loudspeakers [96–98].

The port-Hamiltonian approach holds great promise when applied to the modeling of a combination of lumped and distributed multiphysics systems under a unified framework. The caveat is that each system must be derived by hand as no systematized method currently exists.

2.2 Wave Digital Filters

Wave digital filters are another white box modeling framework that has gained increased attention by the virtual analog research community. Notable merits of WDFs include their inherent modularity, excellent numerical and energetic properties [22] and systematic derivation.

2.2.1 History

WDFs were developed out of the scattering formalism as applied to classical circuit theory [31]. In classical circuit theory the description of the network is given by Kirchoff variables (voltage and current) along with the interconnection of components as expressed by impedance and admittance matrices. Conversely the scattering formalism uses incident- and reflected waves as signal variables while impedance and admittance matrices are replaced by the so called scattering matrix. The scattering formalism was independently developed in microwave applications where it is used still to this day [99].

WDFs were first publicly mentioned in a German patent filed by Alfred Fettweis in 1970 as a way to translate an analog filter design into a digital filter [100]. During the early days, researchers, with Fettweis the most active among them, were mostly interested in establishing the basic theory. For example by studying the digital equivalent of passivity and energetic properties [101], looking at the effects of roundoff noise and attenuation on

the filters [102] and properly formulating how to deal with topologies and the adaptation of ports, a central topic in WDFs [103]. By 1986 when the landmark article "Wave digital filters: Theory and practice" was published [35], WDFs were already a mature field of research, having found a wide field of application well beyond their original scope [104–106].

WDFs were first recognized in the music technology community as early as 1986 [107] when Smith recognized their connection to Digital Waveguides [108]. Since then WDFs have been applied in the simulation of piano hammers [109,110] and other lumped acousto-mechanical systems [22, 36, 111]. Recently, they have been increasingly applied in the simulation of audio circuits [13, 14, 41, 45, 112–114] which is the focus point of this thesis.

2.2.2 Fundamental Principles

To every WDF there is a corresponding lumped analog reference system traditionally represented by a circuit schematic. Similarly to electrical circuits as studied in circuit theory, WDFs contain electrical components and networks that connect them together. A critical part of the WDF approach is that the energetic properties of a given reference circuit are preserved throughout the discretization. In other words, the topology of the reference circuit is always inherited by the resulting digital filter structure. Furthermore an energy-preserving spectral transform is commonly used to digitize reactive components [22]. The versatile energy-conservation law from circuit theory, Tellegen's theorem, is consequently inherited as well [115].

When modeled under the lumped matter discipline (§A.1), electrical components and their interconnections can be fully characterized by the behavior at their ports [55]. Each port has two terminals as shown in Figure 2.3. One of the terminals is traditionally labeled to have positive potential while the remaining one is negative. In the Kirchoff domain, ports are characterized by a port voltage that is measured as the potential difference between the positive and negative terminals and a port current that flows into the positive and out of the negative terminal (Figure 2.3a).

Ports in the wave domain are similarly characterized by an incident and reflected wave as well as a *port resistance* R_0 as shown in Figure 2.3b. The port resistance determines the

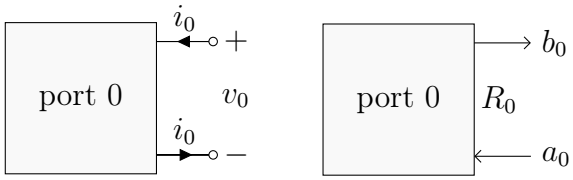

(a) *Kirchoff domain* (b) *Wave domain*

Figure 2.3 *Generic One-Port*

reflectance and transmittance at each port and collectively port resistances determine the transfer of energy inside the structure. In practice the port resistances can be set to any nonzero value, although traditionally the values are assumed to be positive real.

Complications arise when the behavior of reactive components, i.e., that of capacitors, is numerically estimated to be processed by a computer. Although it has been shown that multiple s-to-z mappings (§A.3) can be used to digitize reactive components in WDFs [56,116], WDF theory has traditionally favored the standard bilinear transform [35].

When Kirchoff variables are used as signal variables, the resulting signal processing blocks are known to contain *directed delay-free loops* (signal flow paths that form loops without passing through a delay). A filter structure containing delay-free loops will not be recursively computable and result in a computer program with potentially expensive matrix inversion routines.

At each port in the wave domain we have an additional free parameter at our disposal, the port resistance. Fettweis recognized this fact and by choosing adequate values for each port resistance, directed delay-free loops could be split-up, making the resulting structure computable in a recursive manner [35].

Wave Variables

Wave variables are obtained through a linear transformation from a voltage–current pair to a wave incident and reflected at the port. The wave formulation is analogous to that of traveling waves as used in other areas of music technology, such as digital waveguides [108,117]. In the theory of digital waveguides the sampling period has a physical interpretability re-

lated to the speed of sound and the length of the waveguide.

Virtually infinite wave variable representations exist, with voltage, current and power-normalized waves being the most common. The parametric wave definition is useful tool that was introduced recently [116]. By varying the positive real parameter ρ, a family of transforms that include the standard voltage, powerful-normalized and current waves may be obtained

$$\rho \triangleq \begin{cases} 1 & \text{for voltage waves} \\ \frac{1}{2} & \text{for power-normalized waves} \\ 0 & \text{for current waves} \end{cases} . \tag{2.5}$$

At port 0 in a circuit a linear transformation from the Kirchoff domain $\mathcal{K}$ to the Wave-domain $\mathcal{W}$ is defined as

$$\begin{bmatrix} a_0 \\ b_0 \end{bmatrix} = R_0^{\rho} \begin{bmatrix} R_0^{-1} & 1 \\ R_0^{-1} & -1 \end{bmatrix} \begin{bmatrix} v_0 \\ i_0 \end{bmatrix} = \Phi_{\mathcal{KW}} \begin{bmatrix} v_0 \\ i_0 \end{bmatrix} . \tag{2.6}$$

Given that $\det\left(\Phi_{\mathcal{KW}}\right) = -2R_0^{2\rho-1} \neq 0$ or $R_0 \neq 0$, the inverse transform becomes

$$\begin{bmatrix} v_0 \\ i_0 \end{bmatrix} = \frac{1}{2} R_0^{-\rho} \begin{bmatrix} R_0 & R_0 \\ 1 & -1 \end{bmatrix} \begin{bmatrix} a_0 \\ b_0 \end{bmatrix} = \Phi_{\mathcal{WK}} \begin{bmatrix} a_0 \\ b_0 \end{bmatrix} . \tag{2.7}$$

When the inverse transform exist we always have $\Phi_{\mathcal{WK}}\,\Phi_{\mathcal{KW}} = \Phi_{\mathcal{KW}}\,\Phi_{\mathcal{WK}} = I$, irrespective of the value of ρ.

Reflectance is a concept used to describe how a wave is reflected back and transmitted through a given port. It can also be thought of as the wave domain transfer function. At a given port 0 the instantaneous and steady state reflectances are defined as

$$s_0(t) \triangleq \frac{b_0(t)}{a_0(t)} = \frac{\frac{v_0(t)}{i_0(t)} - R_0}{\frac{v_0(t)}{i_0(t)} + R_0}, \tag{2.8}$$

$$S_0(s) \triangleq \frac{B_0(s)}{A_0(s)} = \frac{\frac{V_0(s)}{I_0(s)} - R_0}{\frac{V_0(s)}{I_0(s)} + R_0} = \frac{Z_0(s) - R_0}{Z_0(s) + R_0}, \tag{2.9}$$

where $Z_0(s)$ is known as impedance in circuit theory. The reflectance can be seen as a Möbius transform [118] from the complex Kirchoff s-plane to the complex wave s-plane.

Example of a Delay-Free Loop

Discretizing a capacitor using standard methods provides us with an opportunity to see first hand how a delay-free loop arises and the way in which wave-variables can be used to split it up. A LTI capacitor with capacitance C is fully characterized at a port 0 by

$$i_0(t) = C\frac{dv_0}{dt} \tag{2.10}$$

and is described in the Laplace domain as

$$I_0(s) = CsV_0(s), \tag{2.11}$$

$$Z_0(s) = \frac{V_0(s)}{I_0(s)} = \frac{1}{sC}. \tag{2.12}$$

Applying the bilinear transform, $s = f_{BT}(z)$ (§A.3) to (2.11) we obtain

$$v_0[n] = v_0[n-1] + \frac{1}{\mu_0 C}(i_0[n] + i_0[n-1]) \tag{2.13}$$

where μ_0 is a free parameter associated with the bilinear transform (A.3) that can be set to any nonnegative value. It becomes apparent when viewing (2.13) that the output signal (voltage/current) of the capacitor is dependent on its input signal (current/voltage) [119]. Computing this difference-equation recursively is thus impossible. If we describe the same capacitor in the wave domain we obtain the following reflectance relationship

$$S_0(s) = \frac{1 - R_0 Cs}{1 + R_0 Cs}, \tag{2.14}$$

$$S_0(f_{BT}(z)) = \frac{(1 - \mu_0 R_0 C) + (1 + \mu_0 R_0 C)z^{-1}}{(1 + \mu_0 R_0 C) + (1 - \mu_0 R_0 C)z^{-1}}. \tag{2.15}$$

Choosing $R_0 = \frac{1}{\mu_0 C}$, the reflectance becomes

$$S_0(f_{BT}(z)) = z^{-1} \tag{2.16}$$

and the difference equation

$$b_0[n] = a_0[n-1]. \tag{2.17}$$

Finding a suitable expression for a port resistance such that the reflected wave is completely determined by the incident wave from the previous timestep is called adapting a port. Any port of a connection, such as a series connection, can also be adapted. An adapted port of a given connection is also known as *reflection-free* and in the WDF nomenclature the connection is known as an *adaptor*.

2.2.3 Connection Trees

WDFs, with properly chosen port resistances, result in recursively computable algorithms. As such they have found a natural representation by means of tree structures [44, 120–122]. Visualizing a WDF as a tree structure, also known as a *connection tree*, begins by choosing a suitable component or adaptor as the *root* of the tree. The remaining structure is allowed to organize itself into subtrees and branches that hang below the root. A connection tree contains leaves (components) and adaptors (connections), i.e., series adaptors, noted by $\mathcal{S}$ and parallel adaptors, noted by $\mathcal{P}$.

The port of the root that faces the remainder of the tree is often unadaptable. In that case, the ports of every leaf and adaptor facing-up towards the root of the tree are adapted. This, in turn, will force the port of the root to become adapted.

A single computational cycle may be visualized as gathering the inputs from leaves (i.e., sources and reactive elements) and advancing them towards the root through the respective adaptors. The incident wave at the root is processed by the root element, after which a reflected wave is fed back down the tree.

Example of Connection Trees

In order to explain how we derive connection trees from schematics we study the simple passive circuit shown in Figure 2.4. We glance at the schematics and look for ways to separate the circuit into individual components connected in series and parallel connections. For this simple circuit we see that components Z_3 and Z_4 are connected in series. This

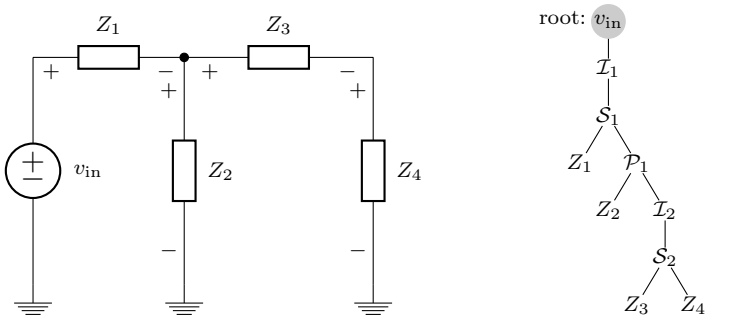

(a) Schematics (b) Connection Tree

Figure 2.4 *Example Circuit*

component pair is connected in parallel with Z_2. The component subset $Z_2 \parallel (Z_3 + Z_4)$ is connected in series with Z_1, that is connected in series with the ideal voltage source v_{in}. This description of the circuit is encoded in the connection tree in Figure 2.4b. We have the inverter adaptors $\mathcal{I}_1$ and $\mathcal{I}_2$ such that polarities in the circuit match in both the Kirchoff- and wave-domains, as defined in Figure 2.3 and §B.1.

It is interesting to compare WDF connection trees to state-spaces, in particular with respect to computational complexity. It is well known that the dimension of a state-space transition-matrix grows linearly with the number of reactive elements M. Matrix inversion, an integral part of the state-space formalism, may be achieved at $O(M^2)$ complexity. It is thus rather expensive to add reactive elements to a state-space model. Conversely adding an algebraic component incurs no added computational cost as no new state is added to the state-vector. The cost is independent on a circuit's topology.

On the other hand inserting any component, algebraic or reactive, into a WDF simulation incurs the same cost, depending on the topology of the reference circuit. Inserting the component is less expensive if it is tied via series or parallel connection to other components, as opposed to a more complex topology.

2.2.4 Adaptors for Arbitrary Topologies

While the scattering behavior of multiport series and parallel adaptors has been known in the WDF literature since the 1970s [103], the issue with deriving the scattering matrix of

more complicated topologies was first recognized by Martens and Meerkötter [123]. They used a graph-theoretic approach to find the scattering matrix of an adaptor with complicated topology, relying on the orthogonality of the reference circuit for their derivation. Although their method was a step in the right direction, it could not be used to derive scattering matrices for circuits containing common audio circuit devices, such as op amps, OTAs, or controlled sources. Most audio circuits could thus not be modeled using standard WDF techniques.

The derivation of a scattering matrix for an arbitrary topology was outlined by Werner *et al.* in [44] and explained in further detail in [116]. The method is based around MNA, which is a systematic way to keep track of physical quantities in a circuit [51]. The method becomes automatable by *stamping* components into a MNA matrix. MNA component stamps also work with the nodal DK-method for deriving nonlinear state-space systems [86].

To derive an arbitrary scattering matrix, Thévenin sources are placed at each port of a $\mathcal{R}$-type (rigid) adaptor and a MNA matrix [51] is populated. Details on how to populate a MNA matrix are readily available in the literature [14, 44, 45, 51]. By treating incident and reflected waves at the same time by grouping them together as vectors $\boldsymbol{b}$ and $\boldsymbol{a}$, a scattering matrix $\mathbf{S}$ describing the relationship between all waves, $\boldsymbol{b} = \mathbf{S}\,\boldsymbol{a}$, given by

$$\mathbf{S} = \mathbf{I} + 2\,\mathbf{R}^{\rho}\,[\mathbf{0} \quad \mathbf{I} \quad \mathbf{0}]\,\mathbf{X}^{-1}\,[\mathbf{0} \quad \mathbf{I} \quad \mathbf{0}]^{\intercal}\,\mathbf{R}^{1-\rho} \tag{2.18}$$

where $\mathbf{R}$ is a diagonal matrix containing the port resistances, $\mathbf{X}$ is the fully populated MNA matrix and ρ is a parameter used to distinguish between wave variables (2.5).

An important detail of this approach is that controlled sources are absorbed into the scattering matrix itself. Absorbing sources into matrices is common practice when populating MNA matrices [51]. In classical WDF theory, absorbing algebraic components (e.g., sources, resistors) into adaptors is also common practice [35]. Doing so yields scattering matrices with ports that can be adapted and placed in a connection tree. Absorbing sources into larger scattering matrices is what enables the modeling of linear circuits of arbitrary topologies.

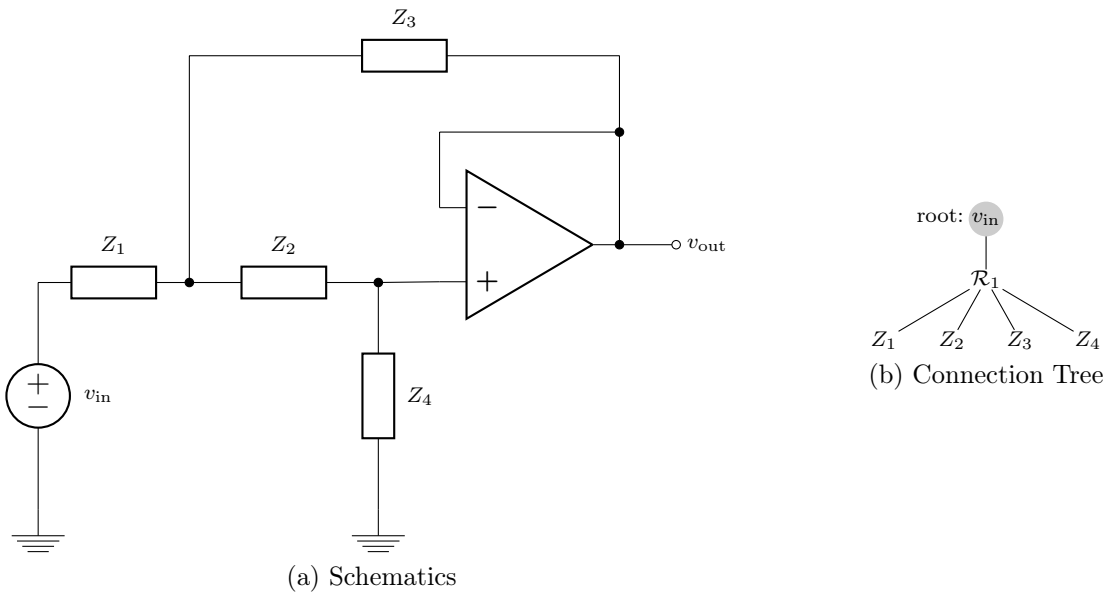

(a) Schematics

(b) Connection Tree

Figure 2.5 *Generic Sallen-Key Filter*

An example of a circuit with a topology that cannot be separated into series and/or parallel connection is the generic Sallen-Key filter circuit (Figure 2.5). First we make the simplification that the op amp is modeled as ideal (nullor) B.1.2. Looking at the schematics we notice that it is in fact impossible to separate most of the circuit into series or parallel connections. Instead we must place a rigid-adaptor $\mathcal{R}_1$ between the circuit elements. We choose the unadaptable ideal voltage source v_{in} as the root of the tree. Note that if we assume that Z_1 is a resistor we could also group v_{in} and Z_1 together to form a resistive voltage source. The resistive voltage source could then be placed at the root of a different 4-port rigid adaptor.

2.2.5 Nonlinearities

The theory of simulating circuits containing up to one nonlinearity began with the work of Meerkötter and Scholz [124]. Researchers have been able to go beyond this limitation in special cases by exploiting topologies of reference circuits [40, 46, 125, 126] or adding fictitious unit delays to yield computable structures [11, 112].

Methods on how to handle multiple nonlinearities in WDFs have been proposed in the past. Some have involved the introduction of ad-hoc unit delays [46, 126, 127], simplifica-

tion of nonlinear devices [40, 114], or ad-hoc [19] or systematic [128] global iteration. A systematized method, sidestepping the aforementioned limitations, was proposed in [43]. The method works by grouping nonlinearities into a single vector that is interfaced with the rest of the circuit by use of an $\mathcal{R}$-type adaptor (2.18). The method is completely general and accommodates circuits of all topologies. An implicit relationship between a vector of nonlinearities and the remaining structure is resolved using the so called K method [83], table lookup or a Newton-Raphson iterative solver [14, 129].

The problem framework can be written as

$$\boldsymbol{a}_i = g(\boldsymbol{b}_i), \tag{2.19}$$

$$\begin{bmatrix} \boldsymbol{b}_i \\ \boldsymbol{b}_e \end{bmatrix} = \begin{bmatrix} \mathbf{S}_{11} & \mathbf{S}_{12} \\ \mathbf{S}_{21} & \mathbf{S}_{22} \end{bmatrix} \begin{bmatrix} \boldsymbol{a}_i \\ \boldsymbol{a}_e \end{bmatrix} \tag{2.20}$$

where g is a static nonlinear function that operates on the wave variables. $\boldsymbol{a}_i$ and $\boldsymbol{b}_i$ are the waves internal to the nonlinearities vector, $\boldsymbol{a}_e$ and $\boldsymbol{b}_e$ are waves that connect to the remaining (external) structure. $\mathbf{S}$ is the scattering matrix of the $\mathcal{R}$-type adaptor. By using wave variables the dimension of the zero-finding function is made linear with respect to the number of ports of nonlinear components [22]. This is generally not the case for Kirchoff-variables.

However, the above formulation has one major flaw. Most nonlinear components are described in the Kirchoff domain and so (2.19) would be more convenient in practice if it were written in terms of voltages and currents rather than wave-variables. Fortunately wave variables are related to Kirchoff variables by a linear transformation (B.1). Rewriting it in vector form we have the voltage–reflected-wave pair written in terms of current–incident-wave pair

$$\begin{bmatrix} \boldsymbol{v} \\ \boldsymbol{b} \end{bmatrix} = \begin{bmatrix} \mathbf{C}_{11} & \mathbf{C}_{12} \\ \mathbf{C}_{21} & \mathbf{C}_{22} \end{bmatrix} \begin{bmatrix} \boldsymbol{i} \\ \boldsymbol{a} \end{bmatrix}. \tag{2.21}$$

Now imagine that we have a voltage–current relation at each nonlinear component port, denoted with a subscript c. The remaining ports of the scattering matrix $\mathbf{S}$ are said to be external to the nonlinear components, denoted with a subscript e. Referring the interested

reader to the full derivation in the literature [43] we express the derived problem statement in terms of auxiliary matrices $\mathbf{E}, \mathbf{F}, \mathbf{M}, \mathbf{N}$ (defined in terms of $\mathbf{C}$ and $\mathbf{S}$)

$$\begin{cases} \boldsymbol{i}_c = f(\boldsymbol{v}_c) \\ \boldsymbol{v}_c = \mathbf{E}\boldsymbol{a}_e + \mathbf{F}\boldsymbol{i}_c \\ \boldsymbol{b}_e = \mathbf{M}\boldsymbol{a}_e + \mathbf{N}\boldsymbol{i}_c \end{cases}, \tag{2.22}$$

where the auxiliary matrices, connecting internal and external wave-variables are defined as

$$\mathbf{H} = (\mathbf{I} - \mathbf{C}_{22}\mathbf{S}_{11})^{-1}, \tag{2.23}$$

$$\mathbf{E} = \mathbf{C}_{12}(\mathbf{I} + \mathbf{S}_{11}\mathbf{H}\mathbf{C}_{22})\mathbf{S}_{12}, \tag{2.24}$$

$$\mathbf{F} = \mathbf{C}_{12}\mathbf{S}_{11}\mathbf{H}\mathbf{C}_{21} + \mathbf{C}_{11}, \tag{2.25}$$

$$\mathbf{M} = \mathbf{S}_{21}\mathbf{H}\mathbf{C}_{22}\mathbf{S}_{12} + \mathbf{S}_{22}, \tag{2.26}$$

$$\mathbf{N} = \mathbf{S}_{21}\mathbf{H}\mathbf{C}_{21}. \tag{2.27}$$

The structure is still not recursively computable due to the directed delay-free loop that originates in $\boldsymbol{i}_c = f(\boldsymbol{v}_c)$. The loop can be resolved using the K method [83], table lookup or Newton-Raphson iterative solver.

Newton-Raphson Iterative Solver

In the remainder of this thesis we employ a Newton-Raphson iterative solver to resolve directed delay-free loops whenever we encounter them. Further details on the Newton-Raphson iterative solver can be found in a number of references, for example [129, 130]. The real valued function h for which we would like to find the root of is given by

$$h(\boldsymbol{v}_c) = \mathbf{E}\boldsymbol{a}_e + \mathbf{F}\boldsymbol{i}_c - \boldsymbol{v}_c \tag{2.28}$$

The initial guess $\boldsymbol{v}_c^{(0)}[n]$ at sample n must be chosen depending on the situation at hand. Two possible initial guesses were proposed in [129]

$$\boldsymbol{v}_c^{(0)}[n] = \mathbf{E}\boldsymbol{a}_e[n-1] + \mathbf{F}f(\boldsymbol{v}_c[n-1]), \tag{2.29}$$

$$\boldsymbol{v}_c^{(0)}[n] = \mathbf{E}\boldsymbol{a}_e[n] + \mathbf{F}f(\boldsymbol{v}_c[n-1]). \tag{2.30}$$

2.2.6 Simulating Time-Varying Systems

WDFs were traditionally used to digitize LTI systems, in particular passive circuits. Given that most audio circuits cannot accurately be modeled as time-invariant systems the LTI assumption should limit the usefulness of the paradigm. Despite that, the WDF literature is quite sparse on the topic while results obtained in practice suggest that WDFs are in certain cases able to simulate time-varying system at least as accurately as SPICE [116,131].

Earliest remarks on simulating time-varying systems in the WDF literature can be found in a set of papers by Strube in 1982 [132, 133]. Strube was interested in modeling the time-varying vocal-tract, that has traditionally been modeled as a collection of coaxial cylinders of varying length and radii. Strube extended the formalism to model systems under time-varying conditions in both space and time. This meant that the underlying structure of reactive elements and transmission lines were severely altered. Strube concluded that by extending the framework in this manner, stability could no longer be guaranteed when standard WDF theory is applied (e.g., voltage waves, LTI components, series/parallel connections).

Three years later, Kubin [134, 135] formulated a proof of stability under time-varying conditions using traditional WDF blocks. The caveat was that power-normalized waves had to be employed as wave variables. In 2005 Bilbao [136] gave a time-varying generalization of all-pass filters built using WDF principles. A first-order all-pass filter was formulated in the wave domain as an ideal voltage source connected in series with a capacitor. The time-varying parameter of the filter was the capacitance. It was proven that the derived DSP structure remained stable if and only if power-normalized waves are used. Proof of stability of a second-order all-pass filter structure, composed of a capacitor/inductor connected in series/parallel, was also provided. This time both reactances were varied. Again

the stability of the abstract DSP algorithm hinged on the choice of wave variables used.

An inherent property of power-normalized wave variables is the guarantee that instantaneous power at each port is independent of the port resistance. That is the instantaneous power at a given port 0 with port resistance $R_0(t)$

$$p_0(t) = v_0(t)\, i_0(t) = \frac{1}{4} R_0^{1-2\rho}(t)\, (a_0^2(t) - b_0^2(t)). \tag{2.31}$$

If we choose $\rho = 1/2$ (power-normalized waves) the instantaneous power indeed becomes independent of the port resistance. This in conjunction with the fact that series/parallel adaptors (or other passive connections [135]) are unitary when power-normalized waves are used (§B.2.4) are the key elements that are involved in the proof of stability. It should be noted that stability is a feature of the abstract DSP structure and does not guarantee, in and of itself, that the algorithm accurately simulates a real-world physical device.

In the following chapter we will explore the inherent limitations of the paradigm further with respect to time-varying conditions. We show why adequate simulation results have been obtained in practice and present novel design strategies that allow an algorithm designer to make better design choices when modeling time-varying systems using WDFs.

2.3 Summary

In this chapter we have reviewed the state of the art in virtual analog modeling, paying special attention to methods that are currently being used to model and digitize audio circuits. Examples of "black-box" and "white-box" modeling techniques were provided with a special emphasis on nonlinear system identification and wave digital filters. The fundamental theory of wave digital filters was reviewed and the ways in which the formalism has recently been extended to model almost all audio circuits. Finally the topic of simulating time-varying systems within the formalism was briefly reviewed.

Later in this thesis we will directly apply the theory when we model several real-world audio circuits using the wave digital filter formalism.

Chapter 3

Time-Varying Conditions and Wave Digital Filters

Being able to accurately simulate time-varying systems is essential if one wishes to model audio circuits using WDFs. In this chapter we explore relevant topics to simulating time-varying systems. In particular we explain why following the traditional WDF paradigm blindly may result in inaccurate simulation when time-varying systems are emulated. We concentrate on the effects of choosing wave-variables and connection trees, followed by a discussion on selecting a suitable discretization method and a discussion on time-varying reactive components.

We begin with a case study; a clear example where following the traditional WDF paradigm results in an inaccurate simulation.

3.1 A Simple Case Study

In this example we look at a passive RC filter circuit (see Figure 3.1a). For the sake of simplicity, let's assume that the input is a unit-step and all components are ideal ones. After some time the capacitor has fully charged up, no current flows and the circuit has converged to a pseudo-DC solution. At that time changing the value of the resistance R should have no influence on the output voltage v_{out}. This particular RC circuit implements a lowpass filter. If we choose $R = 1\,\Omega$ and $C = 0.01\,\text{F}$ we get a time constant of $\tau = RC = 0.01\,\text{s}$. The unit-step responses in voltage and current are displayed in Figure 3.2. Now we would

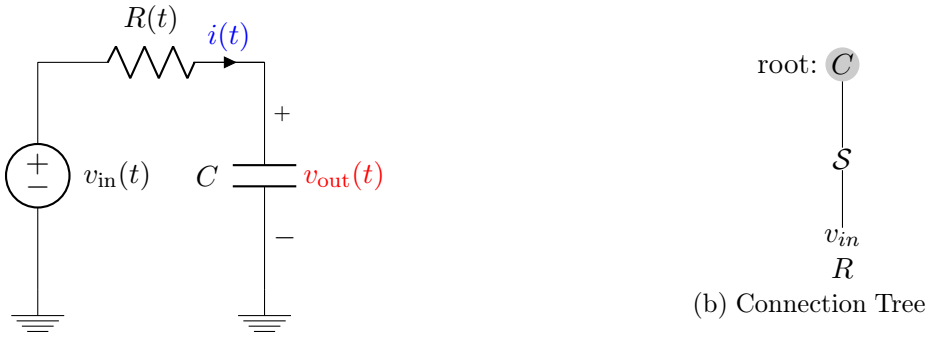

(a) Schematic

(b) Connection Tree

Figure 3.1 *RC Circuit*

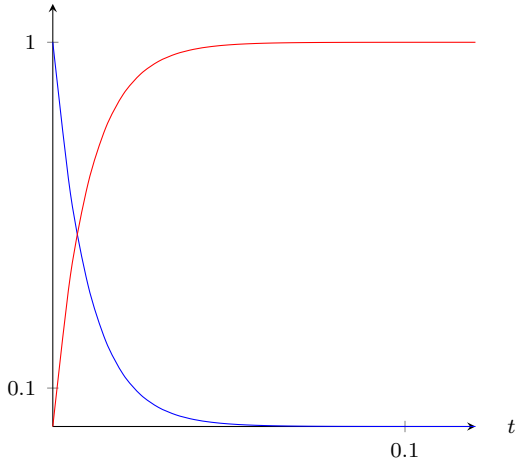

Figure 3.2 *Unit-Step Responses.* v_{out} [V] *and* i_{out} [A]

like to change the resistance R and observe how our WDF algorithm fares. In order to keep things simple we define the resistance to evolve as a step function so that it changes values after *sufficient time*, chosen here arbitrarily as 10τ, has passed

$$R(t) = \begin{cases} 1\,\Omega, & t < 10\,\tau \\ 10\,\Omega, & t \geq 10\,\tau \end{cases}. \tag{3.1}$$

Although $R(t)$ is indeed discontinuous at 10τ when we discretize it we shouldn't have aliasing if 10τ is assumed an integer number of the sampling period. Next we derive a connection tree for the circuit schematic shown in Figure 3.1a. We combine the resistor and ideal voltage source into a resistive voltage source and notice that it is connected in

series with the capacitor. We then create a simple connection tree, discretize the capacitor using the standard bilinear transform and choose it as the root of the connection tree.

We carry out a simulation of the circuit using the unit-step function as an input signal while the value of the resistor is varied in accordance with (3.1). The output is taken to be v_{out} and it is simulated for the three most common wave variables: current, voltage and power-normalized waves. It is compared to a SPICE simulation of the same circuit and time-varying resistor (Figures 3.3-3.5).

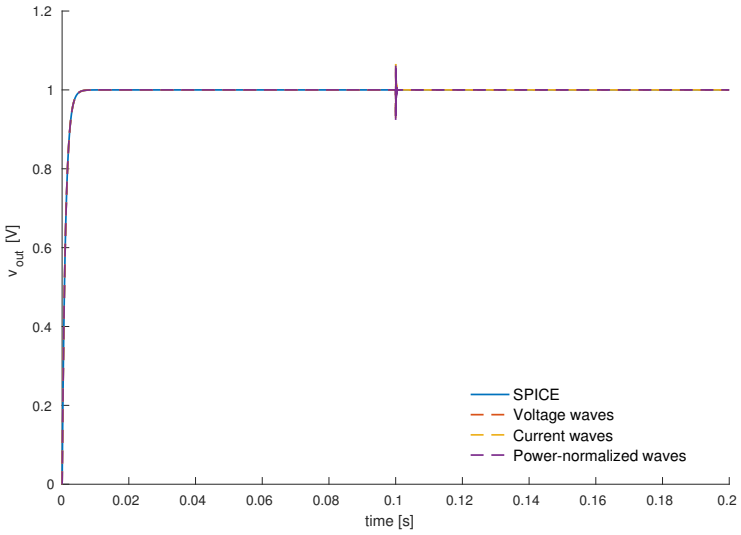

Figure 3.3 *Unit-Step Response v_{out}*

Glancing at Figure 3.3 we notice that the initial responses of the system are identical up to numerical errors. When the resistor's value is changed ($t = 10\tau = 0.1\,\text{s}$) we notice that there is a spike in the voltage. A zoom-in of the response is shown in Figure 3.4.

Both current- and power-normalized waves exhibit the same damped sinusoidal behavior while the SPICE simulation as well as the voltage wave WDF simulation remain constant regardless of the change in resistance. For the current i_{out} we even get a more dramatic behavior from both simulations employing current or power-normalized waves (Figure 3.5).

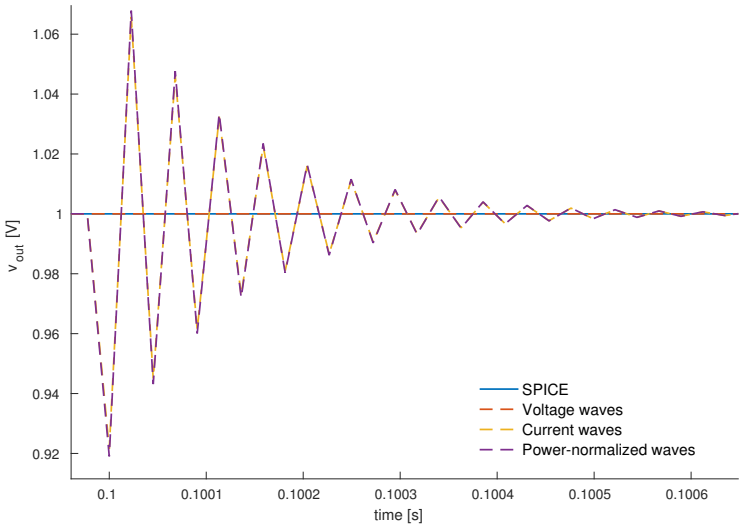

Figure 3.4 *Zoomed-In Unit Step Response v_{out}*

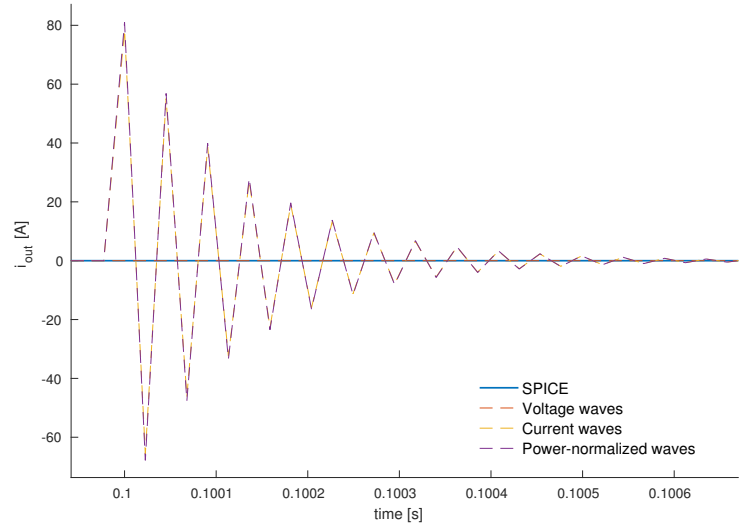

Figure 3.5 *Zoomed-In Unit Step Response i_{out}*

From this simple example we have seen that following traditional WDF theory blindly may have unforeseen side effects under time-varying conditions. It should be noted that the resistance is discontinuous and so the negative effects may be amplified.

3.2 s-to-z Mappings and Proper Numerical Schemes

In traditional WDF theory reactances are discretized using the standard bilinear s-to-z mapping (Table A.2). The underlying assumptions of virtually all s-to-z transforms is that the system being modeled is LTI and in steady-state. In WDF theory discretization is done locally, meaning that each component of the system is discretized separately. In the above example the capacitor is the only reactive element. If we use the bilinear transform, where μ_0 is a tunable parameter (§A.3), to obtain the difference equation for an unadapted capacitor we get (B.10)

$$b[n] = -\frac{1-\mu_0 R_0 C}{1+\mu_0 R_0 C} b[n-1] + \frac{1-\mu_0 R_0 C}{1+\mu_0 R_0 C} a[n] + a[n-1] \tag{3.2}$$

In the previous example the capacitor is placed at the root of a connection tree and so its port resistance becomes dependent on time $R_0[n] = R[n]$. We arrive at the following difference equation.

$$b[n] = -\frac{1-\mu_0 R[n] C}{1+\mu_0 R[n] C} b[n-1] + \frac{1-\mu_0 R[n] C}{1+\mu_0 R[n] C} a[n] + a[n-1] \tag{3.3}$$

It is a well known fact that the bilinear transform is in fact derived from the trapezoidal rule for numerically estimating definite integrals [137, 138]. In the derivation LTI conditions is assumed as parameters are varied with time, similar to what happened in the above example.

It is simple to apply the trapezoidal rule in order to discretize an ideal capacitor with

a constant capacitance C, but time varying port resistance $R_0(t)$ at a given port 0.

$$i_0(t) = C\frac{dv_0}{dt}, \tag{3.4}$$

$$\frac{i_0(t)}{C} = \frac{dv_0}{dt}, \tag{3.5}$$

$$\frac{1}{2}R_0^{-\rho}(t)\ C^{-1}(a_0(t) - b_0(t)) = \frac{d}{dt}\left(\frac{1}{2}R_0^{1-\rho}(t)a_0(t) + \frac{1}{2}R_0^{1-\rho}(t)b_0(t)\right). \tag{3.6}$$

Now we can use the trapezoidal rule to approximate the expression on the left

$$\int_{\mathrm{T}(n-1)}^{\mathrm{T}n} \frac{1}{2}R_0^{-\rho}(t)C^{-1}(a_0(t) - b_0(t))\,dt \approx \frac{T}{2}\left(\frac{a_0[n] - b_0[n]}{2R_0^{\rho}[n]\,C} + \frac{a_0[n-1] - b_0[n-1]}{2R_0^{\rho}[n-1]\,C}\right) \tag{3.7}$$

and the fundamental theorem of calculus to calculate the expression on the right.

$$\int_{\mathrm{T}(n-1)}^{\mathrm{T}n} \frac{d}{dt}\left(\frac{1}{2}R_0^{1-\rho}(t)(a_0(t) + b_0(t))\right)\,dt = \frac{a_0[n] + b_0[n]}{2R_0^{\rho-1}[n]} - \frac{a_0[n-1] + b_0[n-1]}{2R_0^{\rho-1}[n-1]} \tag{3.8}$$

Combining the two expressions gives us the following difference equation

$$\begin{aligned} b_0[n] = &- b_0[n-1]\frac{1 - \mu_0 C R_0[n-1]}{1 + \mu_0 C R_0[n-1]}\left(\frac{R_0[n]}{R_0[n-1]}\right)^{\rho} \\ &+ a_0[n]\frac{1 - \mu_0 C R_0[n]}{1 + \mu_0 C R_0[n]} \\ &+ a_0[n-1]\frac{1 + \mu_0 C R_0[n-1]}{1 + \mu_0 C R_0[n-1]}\left(\frac{R_0[n]}{R_0[n-1]}\right)^{\rho} \end{aligned} \tag{3.9}$$

We assume that $\mu_0 = \frac{2}{\mathrm{T}}$ as is the case for the standard bilinear transform (Table A.2). If we now replace the standard difference equation for an unadapted capacitor with (3.9) and repeat the simulations above, what results is a simulation with no inaccurate response at $t = 10\tau$ like before.

If we take (3.9) and adapt it by placing $R_0[n] = \frac{1}{\mu_0 C}$, we obtain

$$b_0[n] = a_0[n-1] \tag{3.10}$$

which is the same equation as the commonly used adapted capacitor equation (B.11). In

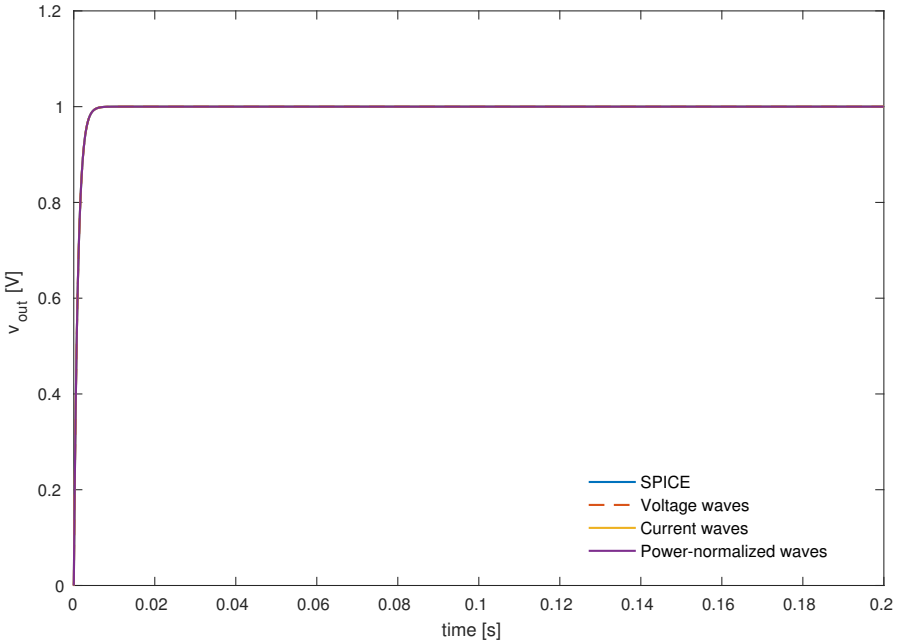

Figure 3.6 *Unit-Step Response v_{out}. Capacitor Discretized using Trapezoidal Rule*

other words the equations for the adapted capacitor is the same when its dynamics are discretized using the standard bilinear transform and trapezoidal rule. They are not equal for the unadapted capacitor. This explains the fact that inaccurate simulations have not been reported in the literature for time-varying systems [131]

3.3 Time-Variant Conditions and Highly-Damped Poles

It is well known fact that the standard bilinear transform warps the frequency axis [139]. Frequency warping methods exist that may be used to compensate for the frequency distortion, but this generally overlooks pole distortion in the general case [137]. There have been reports in the numerical analysis literature where using the trapezoidal rule to discretize systems with highly-damped poles causes high-frequency oscillations in the numerical simulation [140, 141]. This tends to happen when the system is in transient-mode (e.g., time-varying).

In [56] Germain and Werner studied the effects of s-to-z-plane mappings in more detail to include distortion effects on the general location of poles, not only frequency warping. They did so by realizing that the the well known spectral-mappings, forward- and backward Euler and bilinear transform (Table A.2) belong to a set of Möbius transforms that map from the s to z-plane.

A pole location in the s-plane is commonly decomposed as $s = \sigma + j\Omega$ where σ is defined as the *damping* and Ω is the *frequency*. A pole location in the z-plane is similarly decomposed as $z = re^{j\omega}$, $r \geq 0$, $\omega \in]-\pi, \pi]$, where $\log(r)/T$ is defined as the *normalized damping* and ω/T is the *normalized frequency*. A spectral mapping from s-to-z-plane can thus be seen as a mapping between points $s \to z$ or their decompositions $(\sigma, \Omega) \to (\log(r)/T, \omega/T)$.

The α-transform is a spectral mapping that contains both Euler transforms and the bilinear transform as special cases. It is defined as

$$z = f_\alpha^{-1}(s) \triangleq -\frac{\alpha s + \frac{1+\alpha}{T}}{s - \frac{1+\alpha}{T}} \tag{3.11}$$

By tuning α, each of the aforementioned spectral transform may be obtained (e.g., $\alpha = 1$ for the standard bilinear transform). The relation between the quantities (σ, Ω) and r, assuming that the upper s-plane maps to the upper z-plane, becomes [56]

$$r^2(\sigma, \Omega) = \frac{(1 + \alpha + \alpha T\sigma)^2 + (\alpha T\Omega)^2}{(1 + \alpha - T\sigma)^2 + (T\Omega)^2} \tag{3.12}$$

The normalized damping $\log(r)/T$ depends on both the continuous damping σ and frequency Ω. This is a direct result of the fact that the α-transform is a special-case of Möbius transforms, a family of transforms that are all angle-preserving. That is they map every straight line to a line or a circle, and map every circle to a line or a circle.

Spurious high-frequency oscillations of systems with highly-damped poles discretized using the trapezoidal method has been reported in the numerical analysis literature [140,141]. These observations can be explained by the fact that the mapping of pole contours with identical damping in the s-plane, while still circles, are not centered around the origin [56]. In other words, the normalized damping is dependent on continuous-time frequency.

From (3.12) it is simple to see that there is no guarantee that there exists a monotonic relationship between the continuous damping σ and normalized damping $\log(r)/T$. Given that we have knowledge about the operating range of a particular circuit we may know the region in the s-plane where all the poles of the system are located. This information can be put to good use as we can select a value of $\alpha > 0$ such that for all pole locations we can ensure a monotonic relationship between the continuous and normalized damping given that Ω is constant.

The *damping monotonicity criterion* guarantees a monotonic relationship between normalized and continuous damping. It is guaranteed if and only if [56]

$$\left(\sigma - \frac{\alpha^2 - 1}{2\alpha T}\right)^2 - \Omega^2 \leq \left(\frac{(\alpha + 1)^2}{2\alpha T}\right)^2 \tag{3.13}$$

holds for all values of (σ, Ω). We can tune the value of α in such a way that the above condition is always met.

When continuous poles are purely real ($\Omega \equiv 0$) the damping monotonicity criterion simplifies to finding a value of $\alpha > 0$ such that

$$\alpha \geq \frac{-1}{T\sigma + 1} \tag{3.14}$$

is guaranteed for all values of σ. In §5.2.3 we study a nonlinear circuit that contains highly-damped poles. In that case the damping monotonicity criterion is a very useful theoretical tool to have when simulating common audio circuits.

Under time-varying conditions the equivalence between spectral mappings and numerical schemes is lost. Spectral mappings can provide us with valuable information about the system, but become inaccurate under time-varying conditions. The dynamics of the system must be studied first, if possible using spectral mappings, in order to ensure that some design requirements are met (e.g., stability, damping monotonicity). Then a proper numerical scheme should finally be applied to discretize the system [56].

3.4 Time-Varying Reactances

In the preceding discussion we have assumed that although the system as a whole contains reactive components, the time-varying component itself has been purely algebraic and as such memoryless. The WDF literature is rather sparse on the topic of accurately simulating systems where reactances vary with time. One possible explanation for that is that when reactances are allowed to vary with time, the link to the underlying physics is lost under the *lumped matter discipline* §A.1.

Ambiguity in the lumped matter discipline becomes apparent when capacitances are varied. Let us assume that we are changing a given capacitance from C_1 to C_2, where $C_1 < C_2$. Under the lumped matter discipline there are virtually infinite ways to get from C_1 to C_2. Namely, we could have (a) capacitor of C_1 in the circuit and then add a capacitor of $(C_2 - C_1)$ in parallel to it (b) two series capacitors C_a, C_b that in total make up $C_1 = C_a \parallel C_b$. We then remove either one of them (say C_a) such that $C_2 = C_b$ (c) add/remove dielectric between the plates of a capacitor (d) some combination of previous steps. From this trivial though-experiment it is apparent that guaranteeing general passivity/stability when performing the $C_1 \to C_2$ transformation under the lumped matter discipline is infeasible.

In [142] Fettweis proposed *lossless* (no energy dissipated) time-varying models

$$i = \sqrt{C(t)}\ \frac{d}{dt}\left(\sqrt{C(t)}\ v(t)\right), \tag{3.15}$$

$$v = \sqrt{L(t)}\ \frac{d}{dt}\left(\sqrt{L(t)}\ i(t)\right) \tag{3.16}$$

of the capacitor and inductor respectively. For some passive functions $C(t)$ and $L(t)$, the lossless guarantee becomes apparent when the above equation is multiplied by v and i respectively to obtain the instantaneous power [22]

$$p = v \cdot i = \sqrt{C(t)} \cdot v(t) \frac{d}{dt}\left(\sqrt{C(t)}\ v(t)\right) = \frac{d}{dt}\left(\frac{1}{2} C(t)\ v(t)^2\right), \tag{3.17}$$

$$p = v \cdot i = \sqrt{L(t)} \cdot i(t) \frac{d}{dt}\left(\sqrt{L(t)}\ i(t)\right) = \frac{d}{dt}\left(\frac{1}{2} L(t)\ i(t)^2\right). \tag{3.18}$$

The instantaneous power is the time derivative of the energy, which for the two cases above is $\frac{1}{2}L(t)\ i(t)^2 \geq 0$ and $\frac{1}{2}C(t)\ v(t)^2 \geq 0$. The energy is non-negative and the components thus lossless.

Discretization must be performed by applying of trapezoidal rule. Furthermore power-normalized wave variables need be employed in order to guarantee lossless behavior after discretization. Following the same steps as in 3.2 we obtain the following unadapted difference equations for the lossless reactive elements

$$\begin{aligned} b_0[n] = &- b_0[n-1]\ \frac{T/2 - C[n-1]R_0[n-1]}{T/2 + C[n]R_0[n]} \left(\frac{R_0[n]}{R_0[n-1]}\right)^{\rho} \sqrt{\frac{C[n]}{C[n-1]}} \\ &+ a_0[n]\ \frac{T/2 - C[n]R_0[n]}{T/2 + C[n]R_0[n]} \\ &+ a_0[n-1]\ \frac{T/2 + C[n-1]R_0[n-1]}{T/2 + C[n]R_0[n]} \left(\frac{R_0[n]}{R_0[n-1]}\right)^{\rho} \sqrt{\frac{C[n]}{C[n-1]}} \end{aligned} \tag{3.19}$$

which reduces to the familiar adapted capacitor equation if $\rho = 1/2$ (power-normalized waves) and $R_0[n] = \frac{T}{2\ C[n]}$

$$b_0[n] = a_0[n-1]. \tag{3.20}$$

Similar results are obtainable for the inductor and will be left as an exercise for the reader.

Modeling time-varying reactive elements as lossless means that they are stable by definition. The models however only accurately describe reactive elements if the change of reactance varies slowly.

3.5 Summary

In this chapter we explored the topic of time-variance when simulating lumped physical models using the WDF formalism. We saw that the choice of connection tree and port resistances inherently influence the resulting numerical scheme. We provided an example where utilizing power-normalized waves resulted in an inaccurate simulation depending on the connection tree chosen.

The topic of spectral mappings and numerical schemes was briefly discussed. It was shown that in the case of a standard capacitor both bilinear transform and the trapezoidal rule result in the same abstract DSP block when its port is adapted. Similar results can be obtained for the inductor. We reviewed the topic of Möbius transforms as applied to discretizations of lumped element models. For a family of mappings, including both Euler methods and the bilinear methods, the normalized damping is dependent not only on the continuous damping but also frequency. The damping monotonicity criterion was presented as a way to maintain a monotonic relationship between the continuous and normalized damping for a constant continuous frequency.

Finally the topic of time-varying reactances within the lumped model assumption was discussed. Recommendations for implementing time-varying reactances was given with an emphasis on the difference between lossless reactive element as presented by Fettweis, and reactive elements that maintain some link to the physical device they attempt to replicate.

Chapter 4

Common Nonlinear Components

Most audio circuits contain at least one nonlinear component. These components are known to directly influence the characteristic sounds of many audio circuits [50]. Examples of nonlinear components include the diodes responsible for the clipping behavior within the Korg MS-20 filter [57] and transistors used in literally all guitar distortion pedals. Consequently, mathematical models of nonlinear components are essential to the accurate simulation of audio circuits.

Wave Digital Filters were not originally intended for modeling nonlinear circuits. Consequently most nonlinear components have not been introduced into the formalism yet. Nonlinear components that have been handled so far include single diodes [124], any number of diodes in parallel/antiparallel configurations [129,143], BJTs [43,116] and tube models [14,126,144].

In the following chapter we introduce models of three nonlinear components, commonly found in audio circuits, into the WDF framework.

4.1 Zener Diode

Diodes are the simplest yet most commonly found nonlinear devices in audio circuits. They are widely used as switches and waveform clippers in audio filters [57,145,146] and guitar effects [77]. Diodes have three major regions of operation.

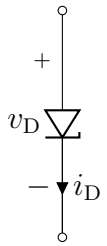

Figure 4.1 *Zener Diode Symbol*

- **Forward bias** When the voltage over a diode is high enough (around $\approx 0.5\,\mathrm{V}$ for silicon diodes) the diode starts conducting. In this region its behavior is often modeled by the Shockley diode model (4.1).
- **Reverse bias** If the voltage over the diode is not high enough the diode will let almost no current through it.
- **Breakdown** If the voltage over a diode becomes sufficiently negative the voltage may reach a point where the diode will start conducting again, only this time in the opposite direction. This occurs when the voltage over the diode exceeds the so called *breakdown voltage* $-V_\mathrm{BD}$ and $v_D < -V_\mathrm{BD}$ is known as the breakdown region.

The physics of how diodes conduct in the breakdown region are explained by two separate phenomena. **Avalanche breakdown** occurs in mildly doped pn-junctions [147]. When current carriers in the junction are accelerated to high energy levels they collide and free up otherwise immobile/bound current carriers. The freed current carriers result in a net increase in current flowing through the diode due to *drifting* of electrons. The higher energy levels of the accelerated current carriers and increased net current can damage the diode if external circuitry is not put into place. **Zener breakdown** occurs in heavily doped junctions under a strong electric field produced by a reverse voltage [147]. The electric field may push electrons to tunnel across the junction, resulting in the repulsion of bound electrons which causes a net current to flow across the terminals of the diode.

Diode Models in the WDF literature

In 2012 Paiva *et al.* proposed an expression of a single diode by providing an explicit wave-domain formulation of the ideal Shockley equation. The explicit solution was put forward by introducing the Lambert W function [148]. Recent work improved upon and extended their model to any number of diodes in parallel/antiparallel configuration [143]. Both proposed methods make the assumption that no other nonlinearity is present in the circuit. The generality of the proposed models is thus limited.

In order to circumvent the aforementioned limitations we propose models of diodes, and other nonlinear components, in the Kirchoff domain. That way we can use the method described in §2.2.5 to handle arbitrary number of nonlinearities in any configuration within the WDF formalism.

The proposed methods model individual diodes using the Shockley diode model [149]

$$i = I_s(e^{\frac{v}{\mu V_\mathrm{T}}} - 1) \tag{4.1}$$

where I_s is the saturation current of the diode, μ is the emission coefficient/ideality factor and V_T is the thermal voltage. The model proposed by Pavia *et al.* does not model the breakdown region of the diode. Neglecting the reverse bias region in this way may be accurate for diodes that are not designed to operate there. However for a large family of diodes this is not the case and more elaborate models are needed.

Diodes in the Breakdown Region

Contrary to most diodes that may get destroyed due to overheating if operated for too long in the breakdown region, Zener diodes are designed to operate there. After the breakdown voltage is reached, the voltage does not vary substantially with increasing current and so Zener diodes are most commonly used as voltage regulators and/or limiters.

Even though Zener diodes are made up of a single pn-junction, forming an accurate model of real-world devices is an overwhelming task. Indeed multiple models exist with

the aim of capturing some of the complex behavior of Zener diodes. Models run the gamut from simpler ones that idealize the diode as a current source, to others that involve multiple tunable parameters. The parameters are used to match static, dynamic and/or temperature-dependent characteristics of individual diodes [150, 151].

We propose a simple model that aims to replicate the static behavior of diodes in all regions of operation. This model is loosely based on the three-step nonlinear diode found in SPICE [34]. The model we propose imitates the static behavior of a real-world diode by forming a two-step nonlinear model.

Table 4.1 *Zener Model—Parameters*

Parameter	Description	Typical value
I_s	Saturation current	1 fA
V_T	Thermal voltage	25.85 mV (at $T = 300\,\mathrm{K}$)
G_min	Minimum conductance	1 nS
V_BD	Breakdown voltage	3.3 V
I_BD	Current at breakdown region	1 mA
μ	Emission coefficient	1.5

The proposed model describes current through a diode as a function of voltage v_D.

$$i_D = \begin{cases} I_s(e^{\frac{v_D}{\mu V_\mathrm{T}}} - 1) + v_D\, G_\mathrm{min} & \text{for } v_D \geq -V_\mathrm{BD} \\ -I_s(e^{-\frac{V_\mathrm{BD}+v_D}{\mu V_\mathrm{T}}} - 1) - I_\mathrm{BD} & \text{for } v_D < -V_\mathrm{BD} \end{cases}, \tag{4.2}$$

its derivative is

$$\frac{di_D}{dv_D} = \begin{cases} I_s \frac{1}{\mu V_\mathrm{T}} e^{\frac{v_D}{\mu V_\mathrm{T}}} + G_\mathrm{min} & \text{for } v_D \geq -V_\mathrm{BD} \\ I_s \frac{1}{\mu V_\mathrm{T}} e^{-\frac{V_\mathrm{BD}+v_D}{\mu V_\mathrm{T}}} & \text{for } v_D < -V_\mathrm{BD} \end{cases}. \tag{4.3}$$

The parameters of the model (see Table 4.1) can be tuned to match the static behavior of the diodes being modeled. The voltage-current relationship assuming the default values in Table 4.1 is shown in Figure 4.2 with the dashed line indicating the breakdown voltage ($v_D = -V_\mathrm{BD}$).

In order to make the above functions continuous at each point we propose that I_BD and

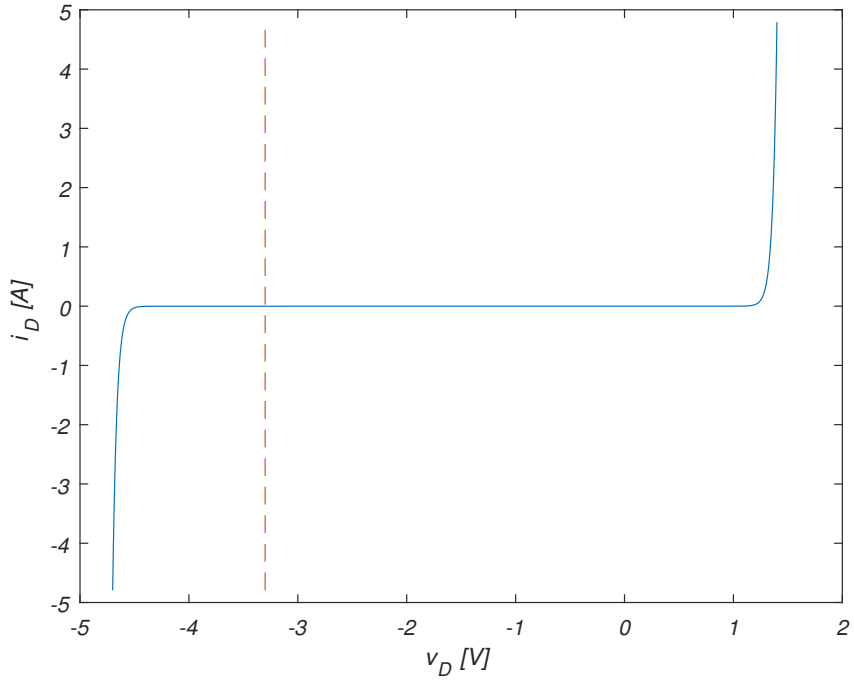

Figure 4.2 *Zener Diode—Voltage/Current Relationship*

$G_{\min}$ are fixed depending on other model parameters, namely.

$$I_{\mathrm{BD}} = -I_s(e^{-\frac{V_{\mathrm{BD}}}{\mu V_{\mathrm{T}}}} - 1) + V_{\mathrm{BD}}\ G_{\min}, \tag{4.4}$$

$$G_{\min} = \frac{I_s}{\mu V_{\mathrm{T}}}(1 - e^{-\frac{V_{\mathrm{BD}}}{\mu V_{\mathrm{T}}}}). \tag{4.5}$$

By fixing I_{BD} and $G_{\min}$ we certainly loose degrees of freedom that could be used to better match a real-world device. On the other hand this simplification ensures the continuity of current and its first derivative with respect to voltage. That in turn results in less spectral distortion (aliasing) in our discrete-time simulation. A further detail refers to our choice of using a Newton-Raphson iterative solver. The solver may become unstable if the nonlinear functions or their derivatives are discontinuous. Having the nonlinear function continuous is thus a desirable trait within the framework we propose.

Obtaining model parameters that accurately match real-world devices can either be done by reading values off datasheets or by performing measurements and tuning parame-

ters accordingly. The proposed model can also be used to model other types of diodes that operate in the breakdown region, such as avalanche diodes [147].

As all diode models based off the Schokley diode model (4.1), the proposed model makes the assumption that the diode is operating in low-level injection. This assumption is known to be inaccurate in power semiconductors [34]. Since most audio circuits are low-power the Shockley model is generally *good enough* for the purposes of audio circuit simulation.

Incorporating proposed model inside a WDF

Incorporating the proposed model into a WDF simulation becomes simple. Each diode is represented by the $i_D = f(v_D)$ relationship in (4.2) and included into the vector of nonlinearities to be placed at the root of a WDF connection tree. Equation (4.3) is placed inside the Jacobian matrix of the Newton-Raphson iterative solver.

In circuit theory elements are often defined in terms of behavior at their terminals (i.e., current, voltage). The WDF formalism however emphasizes the behavior of elements in terms of ports (i.e., waves). The Zener diode has only two terminals and thus only *needs* one port to be properly defined in the WDF domain.

4.2 Field Effect Transistor

A field-effect transistor is a four-terminal semiconductor device, the terminals being gate (G), source (S), drain (D) and body. The body terminal is however not often made available to the circuit designer but rather set internally to bias the device into operation. FETs can be utilized both in amplification and switching and have been applied to a wide range of audio circuits, such as phaser/flanger audio effects [87, 152], amplifiers [153] and audio filters [154].

While BJTs are bipolar semiconductor devices, meaning that they operate by the movement of both electrons and holes (lack of electrons), FETs are unipolar and operate by a single current carrier. FETs that operate using the movement of free electrons are called

n-channel while those that operate by hole movement are *p-channel* FETs.

The voltage difference between gate and source terminals induces an electric field. The strength of this electric field directly modulates the conductive channel that forms between the source and drain terminals and in turn the amount of current that flows through it. FETs control the flow of current by voltage rather than current as is the case with BJTs and thus have high input impedances.

Depending on the FET, it may be in one of two modes.

- **Depletion mode** or *normally-on* devices will conduct if the gate-source voltage is small. By increasing the voltage difference the conductive channel begins to get *depleted* of carriers, effectively making it less conductive.
- **Enhancement mode** or *normally-off* devices work inversely to the depletion mode devices. That is to say the conductive channel is closed (no current flowing) when the gate and source are at the same potential but starts to open as voltage is applied.

The majority carriers in the conductive channel determine the polarity of the gate-source voltage in order to enhance or deplete the conductive channel of carriers.

While a great number of FET devices exist, in this thesis we concentrate on the two most commonly used FETs in audio circuits. Namely the junction field effect transistor (JFET) and the metal-oxide-semiconductor field-effect transistor (MOSFET).

The Shichman-Hodges family of FET models is the most widespread and first-order version of it can be used to capture behaviors of both JFETs and MOSFETs [155]. For the purposes of simulating audio circuits we propose a slightly modified first-order Shichman-Hodges model. The current from drain to source (i_{DS}) is given as a function of the voltage drop between gate and source (v_{GS}). For a n-channel FET this current is given as

$$i_{DS} = \begin{cases} G_{\min}\, v_{GS} & \text{for } v_{GS} < V_{Th} \\ \beta(v_{GS} - V_{Th})^2(1 + \lambda v_{DS}) & \text{for } V_{Th} < v_{GS} \leq v_{DS} + V_{Th} \\ \beta v_{DS}(2(v_{GS} - V_{Th}) - v_{DS})(1 + \lambda v_{DS}) & \text{for } V_{Th} < v_{DS} < v_{GS} \end{cases} \tag{4.6}$$

Table 4.2 *FET Model—Parameters*

Parameter	Description	Typical value
β	Transconductance factor	$1\text{AV}^{\ 2}$
λ	Output conductance (saturation)	$1\text{V}^{\ 1}$
V_{Th}	Threshold voltage	$-2.5\,\text{V}$
G_{min}	Minimum conductance	$1\,\text{nS}$
KP	Transconductance parameter	$20\ \text{mAV}^{\ 2}$
L_{eff}	Effective channel length	$1\,\text{m}$
W	Channel width	$1\,\text{m}$

The three cases correspond to the different modes/regions of operation: Cutoff region, ohmic region and saturation region respectively.

In order to accommodate the three-terminal device in a WDF simulation we assume that there is some tiny current flowing from gate to source

$$i_{GS} = G_{\text{min}}\, v_{GS}. \tag{4.7}$$

Note that the first-order Shichman-Hodges model is accurate only when $v_{DS} > 0$. In the case of audio circuits this is a safe assumption as FETs are commonly biased into operation. For p-channel devices, the voltage polarities and direction of current flow is inverted.

4.2.1 JFET

As the name suggests, the junction field effect transistor contains a pn-junction. The junction lies between the gate and drain/source terminals. The junction is most commonly reverse-biased and the voltage over it is used to control the size of a depletion layer that modulates the conductive channel and in turn the source-drain current. All JFETs are depletion mode devices. The circuit symbols for the n-channel (pn-junction from gate to source/drain) and p-channel (pn-junction from source/drain to gate) are shown in Figure 4.3.

The three model parameters in Table 4.2 $\{\lambda, \beta, V_{Th}\}$ can be read from datasheets supplied by vendors or estimated by measuring individual devices.

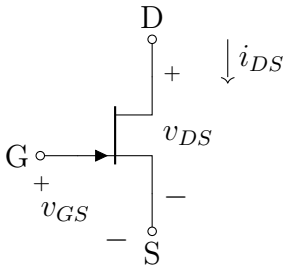

(a) *n-channel Circuit Symbol.*

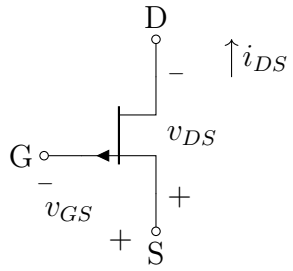

(b) *p-channel Circuit Symbol.*

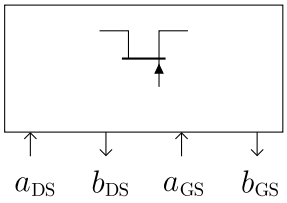

(c) *n-channel Wave-Domain Symbol.*

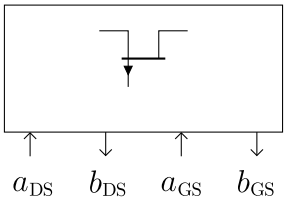

(d) *p-channel Wave-Domain Symbol.*

Figure 4.3 *JFET Symbols*

4.2.2 MOSFET

The metal-oxide-semiconductor field-effect transistor, also known as the insulated-gate field-effect transistor (IGFET) can be seen as a JFET with an additional layer of insulating oxide (or similar material) placed over its gate. The large majority of MOSFETs found in audio circuits are enhancement-mode devices. In the first-order Shichman-Hodges model for the MOSFET, β is expressed in terms of other MOSFET specific device-level parameters (see Table 4.2)

$$\beta = \frac{KP}{2}\frac{W}{L_{\text{eff}}}. \tag{4.8}$$

Incorporating Proposed FET Models Inside a WDF

FETs are three-terminal devices and incorporating them as one-port device is unfeasible. Instead we must model them using two ports, with one terminal of each port wired together.

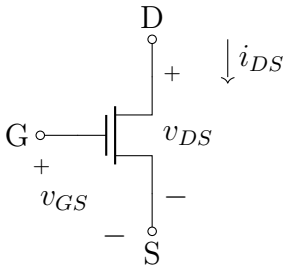

(a) *n-channel Circuit Symbols.*

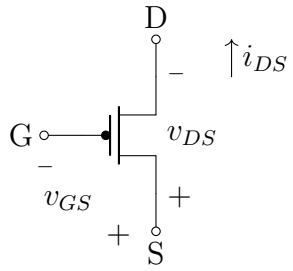

(b) *p-channel Circuit Symbols.*

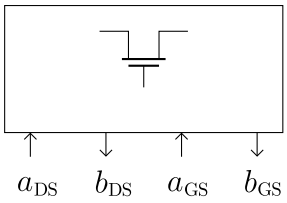

(c) *n-channel Wave-Domain Symbol.*

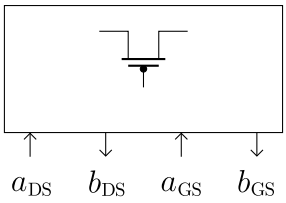

(d) *p-channel Wave-Domain Symbol.*

Figure 4.4 *MOSFET Symbols*

Any choice of terminal currents (gate, drain or source) may be treated as port currents (gate-drain, gate–source, drain–gate, drain-source etc). We arbitrarily choose $[\,i_{DS} \quad i_{GS}\,]^\intercal$ to be our port currents. They are defined in terms of the port voltages $[\,v_{DS} \quad v_{GS}\,]^\intercal$. The two-port FET element (see e.g. Figure 4.4c has port 0 current defined as i_{DS} and port 1 current defined as i_{GS}. The two-port FET is then included at the root of a WDF connection tree as outlined in §2.2.5.

4.3 Operational Transconductance Amplifier

Operational Transconductance Amplifiers, or OTAs for short, are active, tunable, high-gain devices, that take differential voltage as input and output current[1]. The simple external tuning of the gain, called *transconductance*, have made OTAs an essential building block for audio circuit designers. By modifying the transconductance, OTAs are most commonly used to decouple control from audio circuitry, as is done in the filter of the Korg MS-20 synthesizer [57] discussed in §5.3, or in the envelope filter discussed in §5.2.

[1]Contents of this section have been adapted from a paper presented at DAFx17 in Edinburgh [131]

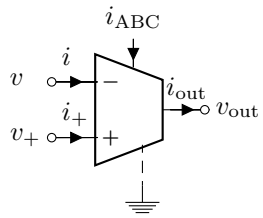

(a) *VCCS OTA Symbol.*

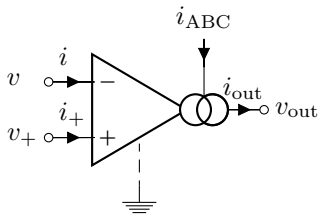

(b) *Alternate OTA Symbol.*

Figure 4.5 *OTA Symbols*

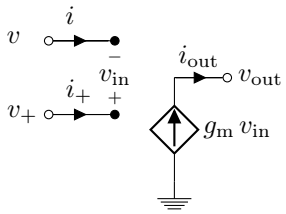

Figure 4.6 *Ideal OTA*

OTAs may be built using bipolar or CMOS transistor technology [156]. CMOS OTAs are widespread in high-frequency applications [147] but are less common in audio circuits where bipolar OTAs are ubiquitous.

On the device level modern OTAs can be quite complex, containing multiple transistors and other nonlinear components in complicated topologies. To simplify circuit design, analysis, and simulation, the behavior of OTAs is often idealized completely or approximated, as is often done with traditional op amps [45]. Such approximations include linear [157] or nonlinear macromodels [158].

The most commonly used OTA symbol in the research community is the VCCS symbol augmented with an additional bias current port as shown in Figure 4.5a. The OTA symbol widely found in circuit schematics is shown in Figure 4.5b.

4.3.1 Ideal VCCS Model

An ideal OTA is a voltage dependent current source, with an adjustable gain, called transconductance g_{m} [156]. The output current i_{out} equals the product of the differen-

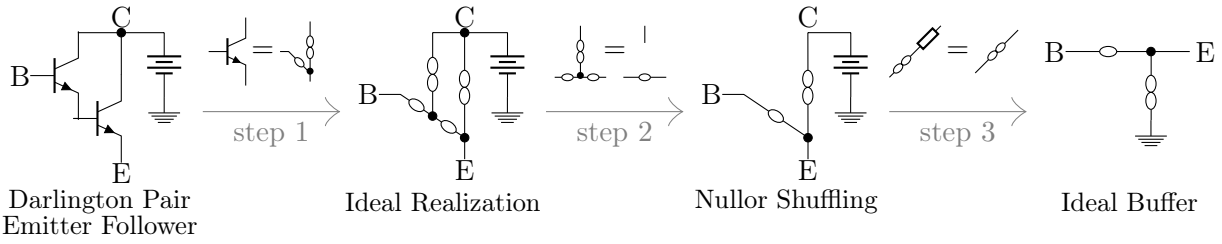

Figure 4.7 *Darlington Pair Emitter Follower to Idealized Nullor Realization*

tial voltage input $v_{\text{in}} = v_+ - v_-$ and g_{m}

$$i_{\text{out}} = g_m \, v_{\text{in}}. \tag{4.9}$$

The conductance between the input terminals is assumed zero as is the case with traditional op amps [45]. The output on the other hand is assumed to be a current source and so the output impedance is large. This is not the case for the standard op amp which exhibits low impedance at its output terminal. Low output impedance is often desirable when designing audio circuits and so modern bipolar-based OTAs, such as the LM13700 [159], include controlled impedance buffers, such as a Darlington-pair [147], on device. In this thesis we will idealize each Darlington-pair as an ideal buffer through the circuit theoretic steps shown in Figure 4.7.

The transconductance of a real world device is a multivariate dynamic nonlinear function, dependent on temperature, device geometry, manufacturing process, etc. [158, 160]. In the ideal case it is a simple function on temperature and a bias current, which the device sinks through a dedicated input terminal. This bias current is often referred to as the Amplifier Bias Current (ABC) i_{ABC}. For an OTA based on a bipolar transistor differential pair, the output current and transconductance are given by [156, 161]

$$i_{\text{out}} = i_{\text{ABC}} \tanh \frac{v_{\text{in}}}{2\,V_{\text{T}}}, \tag{4.10}$$

$$g_{\text{m}} = \frac{di_{\text{out}}}{dv_{\text{in}}} = \frac{i_{\text{ABC}}}{2\,V_{\text{T}}} \operatorname{sech}^2 \frac{v_{\text{in}}}{2\,V_{\text{T}}}. \tag{4.11}$$

In this equation the transconductance depends instantaneously on the differential input voltage. It is however desirable for circuit designers that the transconductance is indepen-

dent of the differential voltage input as discussed in §4.3. Assuming that $|v_{\text{in}}| \ll 2V_{\text{T}}$ the transconductance becomes

$$g_{\text{m}} \approx \frac{i_{\text{ABC}}}{2\,V_{\text{T}}}. \tag{4.12}$$

V_{T}, the thermal voltage, is usually on the scale of tens of millivolts and so making this assumption limits the dynamic range of the input. However, modern OTAs, such as the LM13700 [159], include linearizing diodes that increase the input range of the differential voltage input while keeping the transconductance gain linear with respect to i_{ABC} [161].

The ABC terminal of a bipolar-based OTA can be idealized as an ideal voltage source with constant voltage of $V_{\text{ABC}} = 0.7\,\text{V}$. This idealization is based on the fact that a cathode terminal of a silicone diode is often connected internally to the ABC terminal of a bipolar-based OTA [162]. Note that placing the ideal voltage source outside the circuit containing the OTA in order may reduce complexity.

In §2.2.4 we have described how to transfer a populated MNA matrix from the Kirchoff domain to the wave domain [44]. An ideal OTA is shown in Figure 4.6 while a MNA element stamp is given by (4.13).

$$\begin{array}{c} \\ \gamma \\ \delta \\ \text{next} \end{array} \begin{array}{c} \begin{array}{ccc} \alpha & \beta & \text{n} \end{array} \\ \left[\begin{array}{cc|c} & & 1 \\ & & -1 \\ \hline -g_{\text{m}} & g_{\text{m}} & -1 \end{array}\right] \end{array} \tag{4.13}$$

Nodes shown in Figure 4.6 are $\alpha = v_{+}$, $\beta = v_{-}$, $\gamma = v_{\text{out}}$, $\delta =$ ground.

4.3.2 Linear Macromodel

Real-world OTAs exhibit multiple nonidealities. Some of which may lead to audible effects and need to be taken into account when designing or analyzing audio circuits. Similar to the nonidealities exhibited by standard opamps [45], real-world OTAs have finite input and output conductances and capacitances, input offset voltage, input bias currents, input offset current, differential and common mode gain and also other OTA-specific nonidealities such as frequency dependent transconductance gain [157].

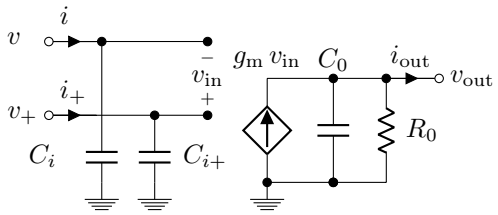

Figure 4.8 *Linear Macromodel OTA*

Choosing which effects to include in a macromodel is a trade-off between complexity and accuracy. Complex nonlinear macromodels for CMOS OTAs exist in the literature [158] and can be adapted to bipolar OTAs by tuning the model parameters. Here we balance complexity and accuracy by proposing a linear macromodel which models input and output capacitances C_{i+}, C_{i-} and C_o as well as a finite output conductance R_o.

Incorporating this macromodel into a WDF structure is simple. The procedure outlined in §2.2.4 is followed as before and the MNA stamp shown in (4.13) is applied for each OTA in the circuit schematic. Depending on the circuit being modeled, the current source may or may not be incorporated inside a $\mathcal{R}$-type adaptor.

4.3.3 Nonlinear Clipping

In the past two subsections we have assumed that $|v_{\text{in}}| \ll 2V_{\text{T}}$ so that the transconductance becomes independent of the input voltage $g_{\text{m}} \approx \frac{i_{\text{ABC}}}{2\,V_{\text{T}}}$. Including the saturating effects from (4.11) into a simulation will result in a more accurate, refined model of the real behavior. Furthermore it may also be sonically interesting. The nonlinear transconductance is defined as (4.11)

$$g_{\text{m}} = \frac{i_{\text{ABC}}}{2\,V_{\text{T}}} \operatorname{sech}^2 \frac{v_{\text{in}}}{2\,V_{\text{T}}}. \tag{4.14}$$

Incorporating Proposed OTA Models into WDF

In order to include the nonlinear transconductance into the proposed models we place an additional resistor R_i (Figure 4.9a) across the input terminals so that the Newton-Raphson solver may have an easier time converging. The ports of the input terminals and nonlinear

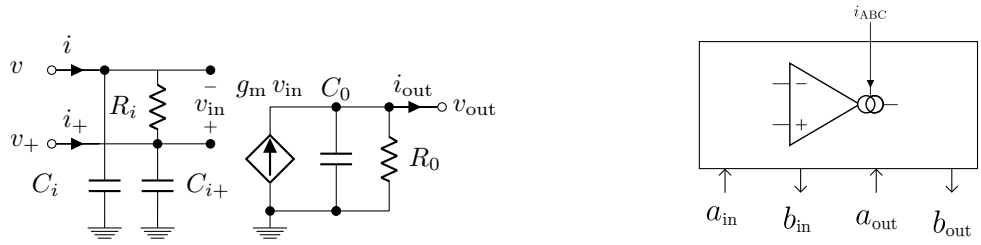

(a) *Circuit Schematics.* (b) *OTA symbol.*

Figure 4.9 *Nonlinear Macromodel OTA*

current source are treated as a single two-port nonlinear device. The input vector is thus defined by $[\, v_{\text{in}} \quad v_{\text{out}} \,]^{\intercal}$ and output vector $[\, i_{\text{in}} \quad i_{\text{out}} \,]^{\intercal}$.

The capacitors are to be placed in the tree that grows below the nonlinearities placed at the root. i_{ABC} is sourced externally and the scattering behavior of the adaptor or root element that contains the VCCS must be updated when i_{ABC} varies. Finally the steps indicated in §2.2.5 may be followed to derive the nonlinear WDF.

An example of incorporating the proposed linear and nonlinear OTA models to a WDF simulation is given as a case study in §5.2.

4.4 Summary

In this chapter we elaborated on the importance of being able to model the behavior of nonlinear components in audio circuits simulation. We then proceeded to introduce models of nonlinear components commonly found in audio circuits into the WDF formalism. For each proposed model we outlined the steps necessary to incorporate the models in a WDF simulation.

Now that we have reviewed the relevant theory we can continue to model audio circuits that contain Zener diodes, FET transistors and operational transconductance amplifiers using the WDF approach to circuit modeling.

Chapter 5

Nonlinear components in WDFs—Case Studies

In this chapter we put the theory introduced in previous chapters to good use. We simulate three audio devices that contain nonlinear devices introduced into the WDF formalism in Chapter 4.

To assess the accuracy of the derived WDF models we compare various simulations to that of SPICE. We utilize test signals of varying complexity in both frequency- and time domain to make sure our algorithms are at least as accurate as a corresponding simulation obtained from SPICE.

5.1 FET Booster Circuit

The circuit we study first is a FET booster guitar pedal[1]. A booster effect is commonly used to amplify an input signal without distorting it heavily. The amount of amplification is configurable via the potentiometer R_g made available to the user on the front of the device.

The circuit that implements the FET Booster is built around a single N-channel JFET transistor (Figure 5.1a). The JFET is biased to operate in its linear region and does not

[1]Circuit adapted from http://www.muzique.com/lab/boost.htm

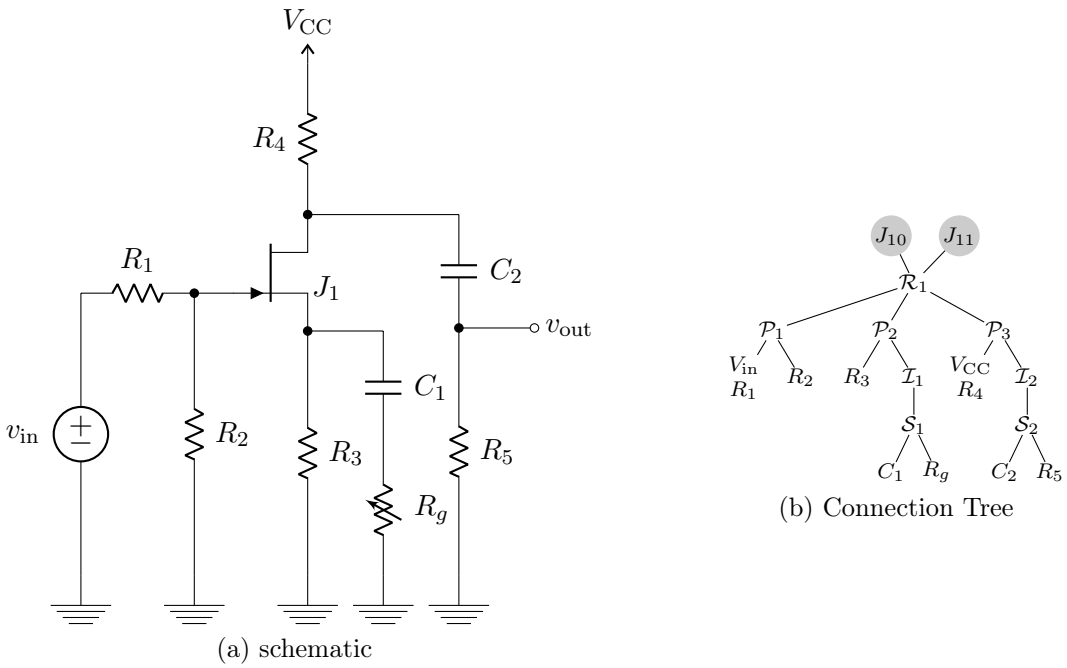

(a) schematic

(b) Connection Tree

Figure 5.1 *FET Booster*

introduce substantial overtones to the input signal.

Deriving a WDF model of the FET booster circuit begins, as always, by looking at the schematic (Figure 5.1a). In order to minimize computational complexity each rigid adaptor should have as few ports connected to it as possible. We look for opportunities to separate its topology up into individual components connected in parallel and/or series connections, resigning to rigid connections only if necessary. At the same time we must be careful that the two ports belonging to the FET are not separated as they need to be available as a pair at the root of the connection tree [43].

The topology of the FET Booster circuit is rather simple and it is trivial to perform decomposition of its topology by looking at the schematic. For more complex circuits, a graph-theoretic approach has been proposed in the literature that handles arbitrarily complex linear topologies [120, 121]. It has recently been extended to arbitrarily complex nonlinear ones [43]. The fully decomposed circuit is visualized as a connection tree in Figure 5.1b. J_{10} corresponds to the v_{DS} port of the JFET while J_{11} corresponds to the v_{GS}

Table 5.1 *FET Booster—Component Values*

Component	Value
R_1	$1\,\mathrm{k}\Omega$
R_2	$1\,\mathrm{M}\Omega$
R_3	$4.4\,\mathrm{k}\Omega$
R_4, R_5	$10\,\mathrm{k}\Omega$
R_g	$[1\,\mathrm{k}\Omega,\ 5\,\mathrm{k}\Omega]$
C_1, C_2	$10\,\mu\mathrm{F}$
V_{CC}	$9\,\mathrm{V}$

port. Note that this particular connection tree is only one of multiple possibilities.

3-port series and parallel adaptors have well known scattering matrices. The scattering matrix for each rigid adaptor must however be computed on an ad hoc basis. The connection tree contains a single rigid adaptor $\mathcal{R}_1$ and so its scattering matrix must be computed. Scattering matrices for arbitrary rigid adaptors are determined by transforming a populated MNA matrix derived from the circuit after its topology has been decomposed into parallel, series and rigid connections.

The process by which a MNA matrix is populated is described in detail in [44]. For each of the five ports connected to $\mathcal{R}_1$ we place a resistive voltage source, defining one terminal to be positive. Each node in this circuit is identified by a unique integer. Each port of the circuit is given a unique letter and port resistance in such a way that the ports facing up towards $\mathcal{R}_1$ are adapted. Ports connected to nonlinear elements, such as the JFET, are given some arbitrary port resistance that won't affect the simulation. With all nodes and ports uniquely identified the MNA matrix is populated using MNA element stamps as shown in [51].

Once the MNA matrix is populated, the scattering matrix is computed using (2.18), see §D for a script that calculates the scattering matrix. Special attention must be paid to the polarity of the sub-trees that hang off $\mathcal{R}_1$, such that they are correct with respect to the component and adaptors as defined in Appendix B.1. Incorrect polarity may have disastrous effects on the simulation of circuits that contain nonlinear devices [42]. Once

the scattering matrix is computed the matrices $\mathbf{E}, \mathbf{F}, \mathbf{M}, \mathbf{N}$ are computed using (2.23) to (2.27) such that the nonlinear equations of the JFET transistor may be solved locally.

The FET model derived in Chapter 4 is placed at the root of the connection tree and the capacitor is discretized using the standard bilinear transform. We extended the RT-WDF C++ library [144] with the FET nonlinear model and implemented a Newton-Raphson iterative solver with backtracking to improve the chances of convergence [6].

5.1.1 Comparison to SPICE

To assess the accuracy of the derived WDF model we compare it to the same exact model in SPICE. The first input is a 440 Hz sine wave with constant amplitude of 0.5 V. Next we

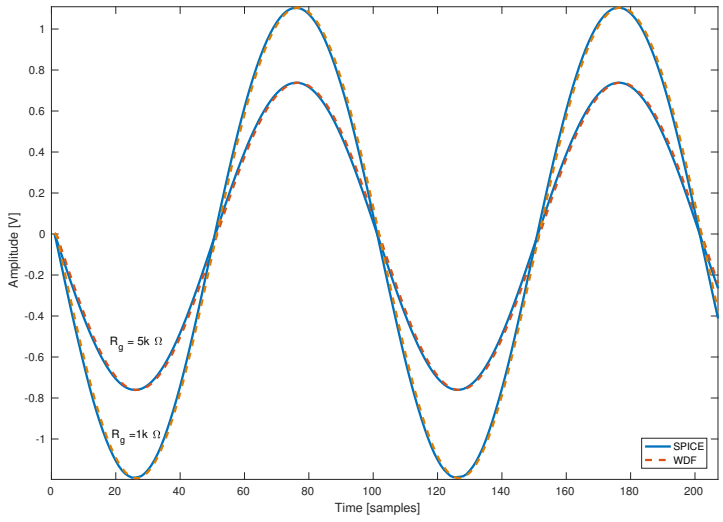

Figure 5.2 *FET Booster—Amplitude Boosting.* 440 Hz *Sine Input,* $R_g = 1\,\mathrm{k}\Omega, 5\,\mathrm{k}\Omega$. *16x Oversampling.*

fix $R_g = 2\,\mathrm{k}\Omega$. The amplitude of the partials from the SPICE simulation are marked with a circle. In Figure 5.3 we see the processed signal with 16x oversampling. The simulation matches that of SPICE nicely.

We next compare the derived WDF algorithm to SPICE when the input is a multi-partial signal. We use the same antialiased 440 Hz sawtooth wave (Figure 5.4) and place

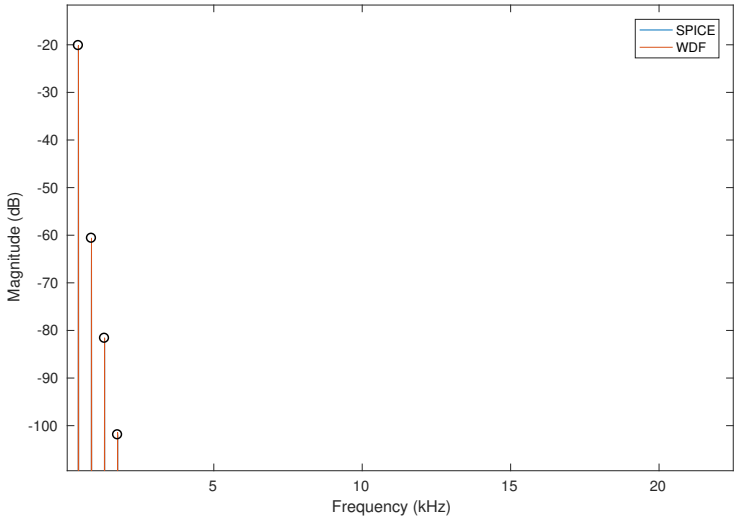

Figure 5.3 *FET Booster*—440 Hz *Sine Input,* $R_g = 1\,\mathrm{k}\Omega$. *16x Oversampling.*

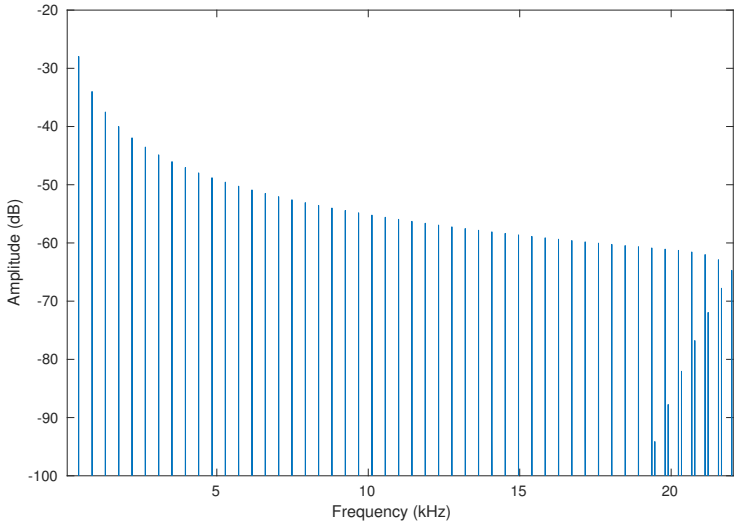

Figure 5.4 *Antialiased* 440 Hz *Sawtooth.*

$R_g = 1\,\text{k}\Omega, 5\,\text{k}\Omega$. We see that the WDF simulation compares nicely to that of SPICE, as seen in Figure 5.5 and Figure 5.6 respectively. Since the FET is operating in its linear

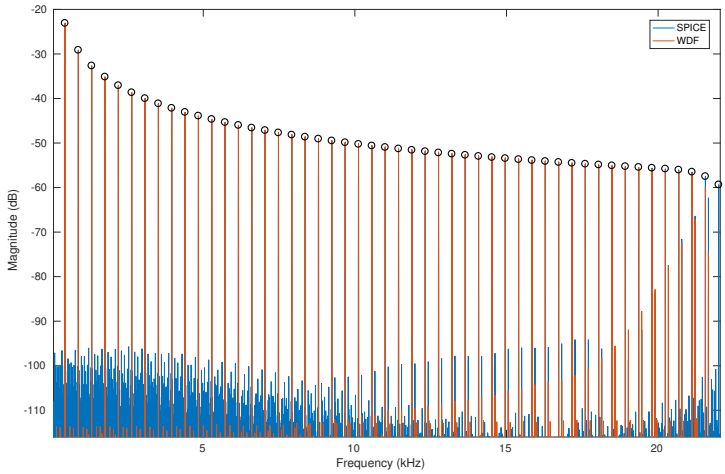

Figure 5.5 *FET Booster—*440 Hz *Antialiased Sawtooth Input,* $R_g = 1\,\text{k}\Omega$*. 16x Oversampling.*

region we do not expect a substantial effect on the spectrum when tuning R_g, other than (almost) linear amplification. This is precisely what we see in Figures 5.5–5.6.

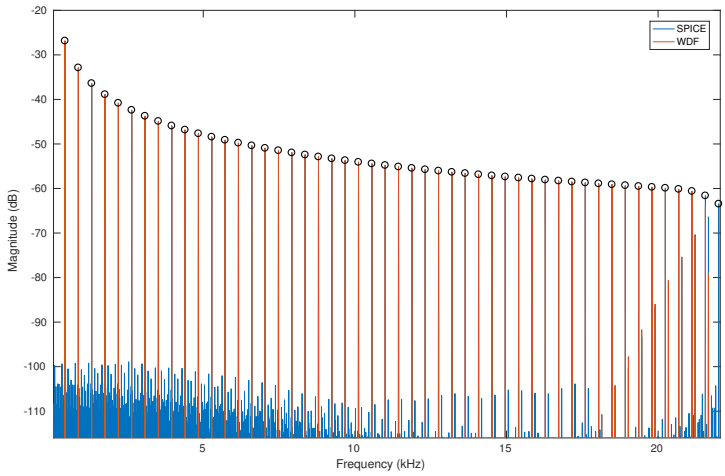

Figure 5.6 *FET Booster—440 Hz Antialiased Sawtooth Input, $R_g = 5\,\mathrm{k}\Omega$. 16x Oversampling.*

5.2 Envelope Filter

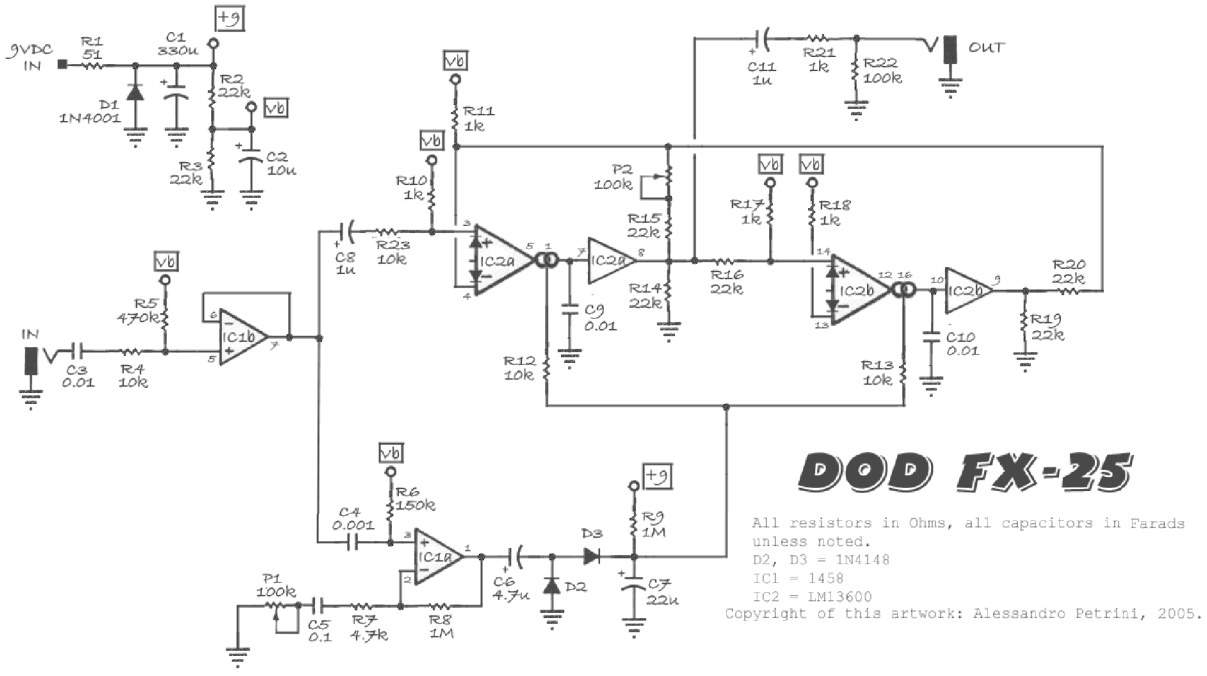

Figure 5.7 *Envelope Filter—DOD FX25 Clone Schematic*

In this section the OTA models proposed in Chapter 4 are utilized to model an envelope filter guitar/bass effect. The schematic we study [163] is based on the DOD FX-25 guitar pedal[2].

In general an envelope filter tracks the temporal envelope of an input signal. The envelope directly modulates the critical (e.g., resonant or cutoff) frequency of a filter, that in turn filters the input. This self-modulation can create some very interesting sonic effects, envelope filters are also referred to as auto-wah effects. The critical frequency of the filter is swept automatically up and down depending on the strength of a player's picking and not by the movement of his foot on a rocking pedal as is the case with traditional wah-wah pedals. Some are even controlled by an arm that is directly attached to a guitar.

The envelope filter we study has two parameters to be configured by the user. The *sensitivity* parameter influences how intensely the envelope follower reacts to a given input, thus influencing the maximum critical frequency the filter can be swept to. The *range* parameter is used to determine characteristics of the filter, such as the gain (5.11), critical frequency (5.12) and Q-factor (5.13).

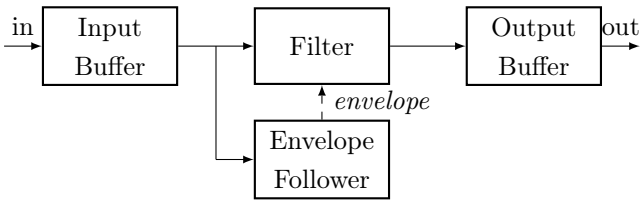

Figure 5.8 *Envelope Filter—Block Diagram*

The complete circuit diagram in Figure 5.7 is quite complex and would pose a formidable challenge if no simplifications were made. In the rest of this thesis we model operational amplifiers as nullors [45,164]. From a circuit-theoretic standpoint the output of the norator connected in series to a load is equivalent to a norator and an ideal voltage source [164] connected in series to the same load. That is the load does not influence the output of the norator at all. By modeling each op-amp using a norator we are able to split the complete

[2]Figure 5.7 is displayed with approval from the author.

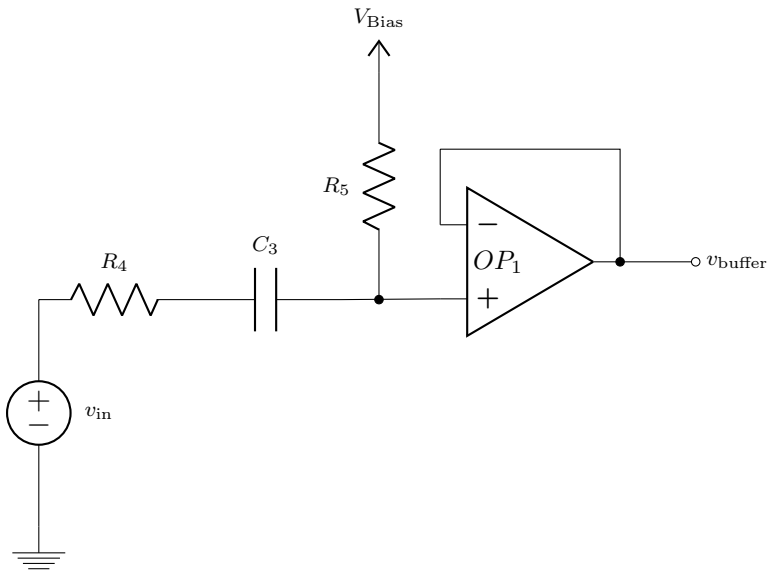

(a) Schematic

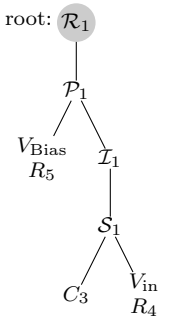

(b) Connection Tree

Figure 5.9 *Envelope Filter—Input Buffer*

Table 5.2 *Envelope Filter—Input Buffer Component Values*

Component	Value
R_4	10 kΩ
R_5	470 kΩ
C_3	10 nF
V_{Bias}	4.5 V

circuit up into smaller subsections. The general abstract block diagram of the effect is shown in Figure 5.8.

5.2.1 Input Buffer

The input buffer is a simple 1st-order high pass filter with C_3 acting as a coupling capacitor. R_1 and R_2 bias the input signal to the operating voltage. The op-amp in a non-inverting buffer configuration that furthermore provides high input-impedance, a desirable trait of real-world audio effects. In the digital realm there is no effective coupling at this stage, due to the way we model the op amp, and so we can skip the op amp modeling and take the

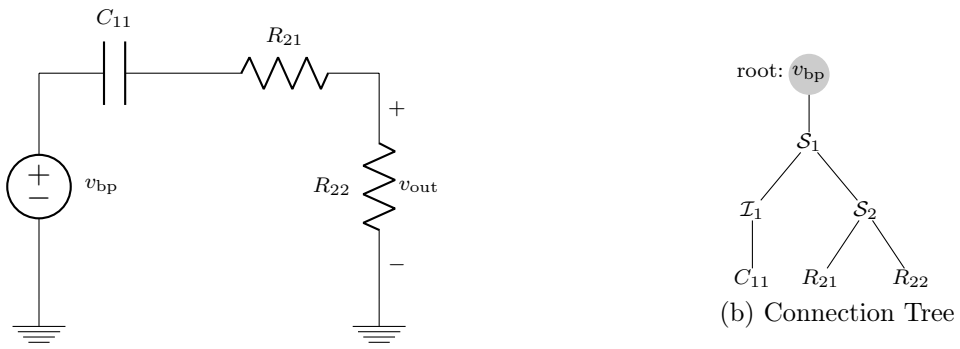

(a) Schematic

(b) Connection Tree

Figure 5.10 *Envelope Filter—Output Buffer*

Table 5.3 *Envelope Filter—Output Buffer Component Values*

Component	Value
R_{21}	$1\,\text{k}\Omega$
R_{22}	$100\,\text{k}\Omega$
C_{11}	$1\,\mu\text{F}$

voltage over $R_5 + V_{\text{Bias}}$ as the output voltage. The transfer function from v_{in} to v_{buffer} is

$$H(s) = \frac{V_{\text{buffer}}(s)}{V_{\text{in}}(s)} = \frac{s\frac{R_5}{R_4+R_5}}{s + \frac{R_5}{C_3(R_4+R_5)}} \tag{5.1}$$

One possible connection tree for the input buffer is shown in Figure 5.9b. Deriving the rigid adaptor is done as described in §5.1 and will be omitted here for sake of brevity.

5.2.2 Output Buffer

The output buffer (Figure 5.10a) decouples the processed signal from the internal operating voltage and supplies it to the outside world. Similar to the input buffer, the output buffer is also a 1st-order high-pass filter, with a similar linear transfer function, but different component values. One connection tree for the output buffer is shown in Figure 5.10b.

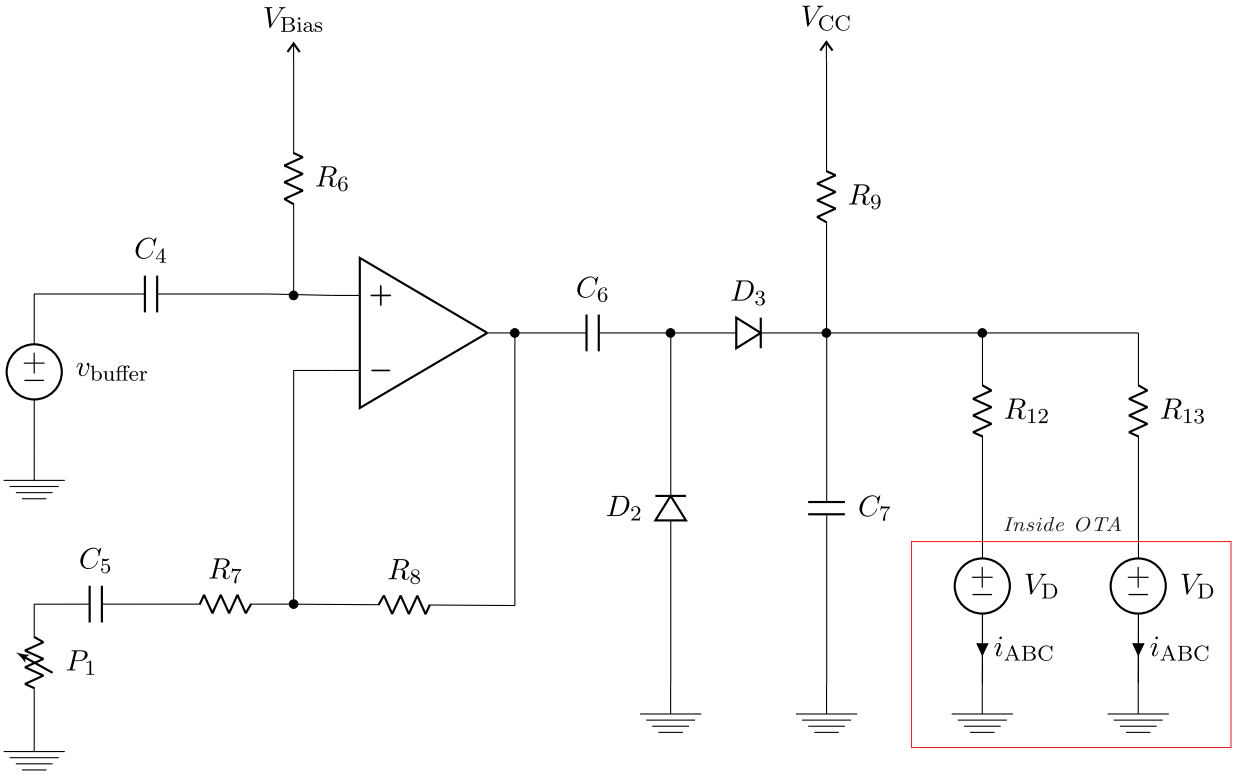

Figure 5.11 *Envelope Filter—Envelope Follower Schematic*

5.2.3 Envelope Follower

The circuit that implements the envelope tracking/following is centered around two diodes, D_2 and D_3. Since the voltage over the diodes won't enter their respective breakdown region for the range of operating voltages of the circuit, we model them using the ideal Shockley diode equation (4.1). Ideal voltage sources $V_{\text{ABC}} = 0.6\,\text{V}$ are placed in series with R_{12} and R_{13} to model the circuit inside the ABC terminal (§4.3).

As before we model the op-amp as a nullor. A norator (output port of the nullor) in series with some load is simply a norator [164]. From a circuit-theoretic point of view the left terminal of C_6 in Figure 5.11 is connected to an ideal voltage source that sources/sinks the voltage supplied by the op-amp. Having the circuit split up into two separate sections, linear (see Figure 5.12a) and nonlinear (see Figure 5.13a), means that we have two WDF trees running side-by-side. This results in smaller $\mathcal{R}$-type adaptors that reduce complexity.

Table 5.4 *Envelope Filter—Envelope Follower Component Values*

Component	Value
R_6	150 kΩ
R_7	4.7 kΩ
R_8, R_9	1 MΩ
P_1	100 kΩ
C_4	1 µF
C_5	100 nF
C_6	4.7 µF
C_7	22 µF
D_2, D_3	1N4148
V_{Bias}	4.5 V
V_{CC}	9 V

Envelope Follower—Linear Section

The linear section implements a cascade of a 1-st order high-pass filter composed of C_4 and R_6 that is cascaded to a 1-st order high-frequency shelving filter that is made up of the remaining components.

$$H(s) = \frac{V_{\text{linear}}(s)}{V_{\text{buffer}}(s)} = H_{\text{HP}}(s) \cdot H_{\text{SHELF}}(s) = \frac{s}{s + \frac{1}{R_6 C_4}} \frac{s\frac{P_1+R_7+R_8}{P_1+R_7} + \frac{1}{C_5(P_1+R_7)}}{s + \frac{1}{C_5(P_1+R_7)}} \tag{5.2}$$

In order to simplify the resulting connection tree we add an ideal resistor R_{buffer} in series with v_{buffer}. As every voltage source has some intrinsic resistance, inserting R_{buffer} will not affect the accuracy of our simulation. We assume that its value is small enough so that effects from it can be neglected from calculations.

Envelope Follower—Nonlinear Section

The nonlinear section of the circuit implements the envelope tracking (Figure 5.13). A resistor of some small resistance R_{linear} is included so that it can form a resistive voltage source with v_{linear}. In order to get an intuitive understanding of what is going on within the nonlinear section we imagine that a step function is supplied as input via v_{linear}. If the voltage over D_3 is higher than its forward voltage, it is switched on and will start to conduct. At that point in time C_7 will begin charging up. Simultaneously C_6 also begins

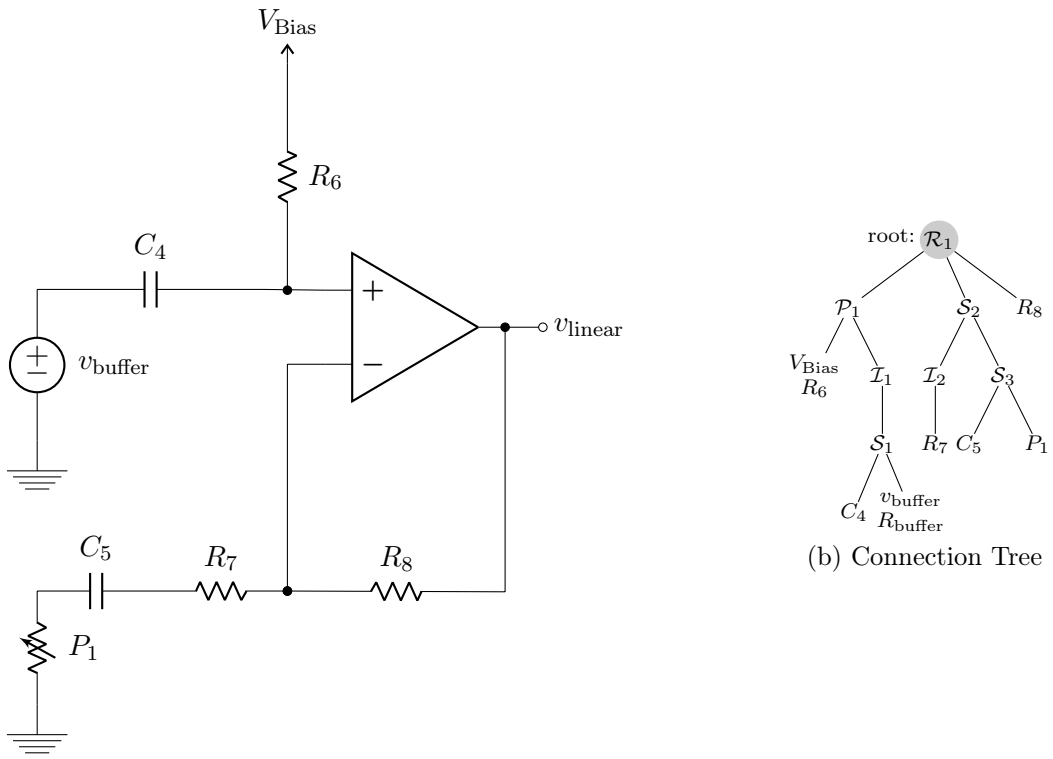

(a) Schematic

(b) Connection Tree

Figure 5.12 *Envelope Filter—Envelope Follower (Linear Section)*

charging up, eventually reaching a point where the voltage over D_3 is less than its forward voltage and it stops conducting, effectively entering a switched off state.

Some of the current that is fed through D_3 will flow directly through resistors R_{12} and R_{13}, as amplifier bias current, into the filter section. Once the input goes down again the polarity over D_2 may become greater than its forward voltage and current will flow through D_2 and C_6 to the ideal voltage source.

The fact that the diodes are operated as switches means that the damping of the instantaneous poles of the circuit will vary greatly in a short amount of time. To accurately discretize this subsection we must resort to the use of an α-transform and the damping monotonicity criterion as discussed in §3.2. First we need to figure out the locations of poles in the system.

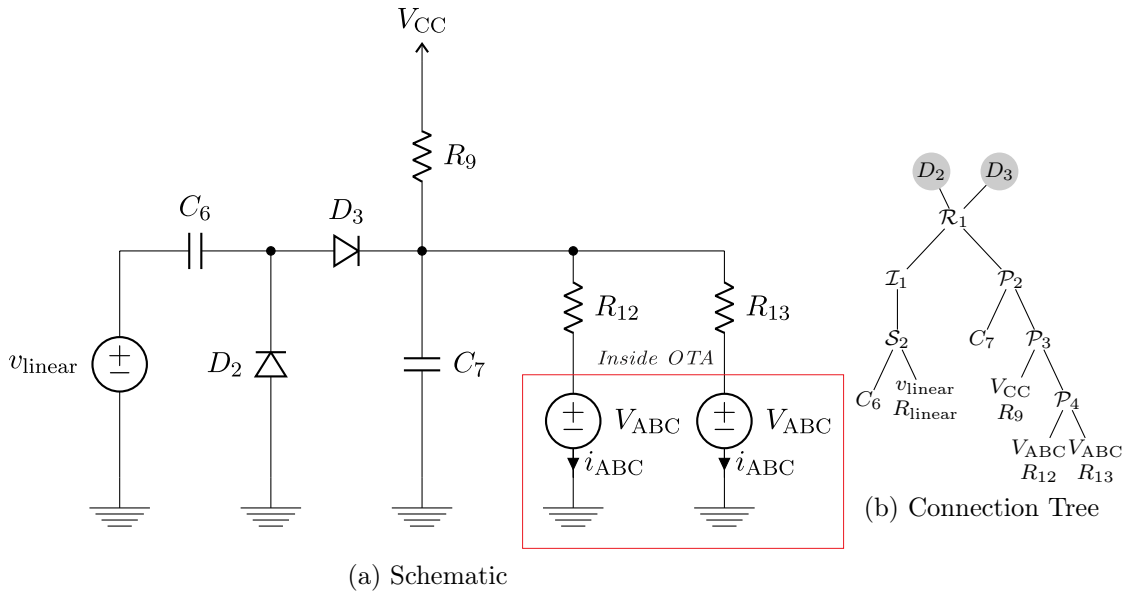

Figure 5.13 *Envelope Filter—Envelope Follower (Nonlinear Section)*

In order to do so we must first linearize the circuit around a given operating point and derive transfer functions from the input, over the two diodes. We use a small-signal model for each of the diodes [147]. This model assumes that the voltage over a diode D may be split up into a DC and AC parts $v_D(t) = V_D + v_d(t)$. Plugging this into the Shockley diode equation gives us

$$i_D(t) = I_s(e^{\frac{v_D(t)}{\mu V_T}} - 1) \approx I_s e^{\frac{v_D(t)}{\mu V_T}} \tag{5.3}$$

$$= I_s e^{\frac{V_D}{\mu V_T}} e^{\frac{v_d(t)}{\mu V_T}} = I_D e^{\frac{v_d(t)}{\mu V_T}} \tag{5.4}$$

We now perform the first Taylor expansion of $e^{\frac{v_d(t)}{\mu V_T}}$ around $v_d(t) = 0\,\mathrm{V}$

$$e^{\frac{v_d(t)}{\mu V_T}} \approx 1 + \frac{v_d(t)}{\mu V_T} \tag{5.5}$$

thus recovering the diode current split into DC and AC parts

$$i_D(t) \approx I_D + \frac{I_D}{\mu V_T} v_d(t) = I_D + \frac{1}{r_D} v_d(t). \tag{5.6}$$

r_D is known as the small-signal resistance and must be calculated based on the operational

conditions of the circuit. Using the small-signal approximation, diodes D_2 and D_3 can be

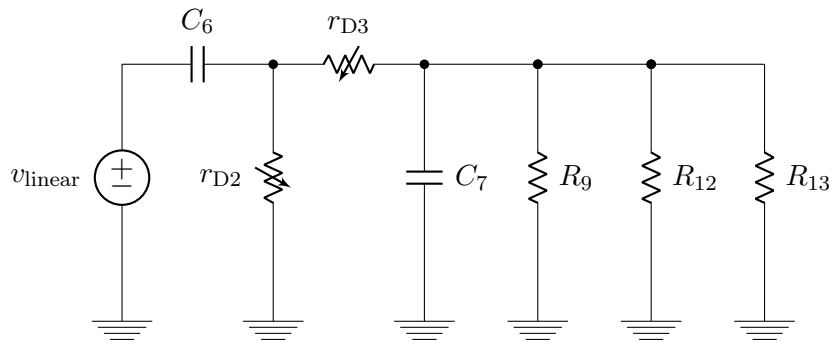

Figure 5.14 *Envelope Filter—Envelope Follower (Nonlinear Section) Small Signal Approximation*

replaced by their small-signal equivalences r_{D2} and r_{D3}. Assuming that other DC sources are placed at zero we obtain the small-signal equivalent circuit in Figure 5.14. Now we can derive a transfer functions by using MNA-based techniques described in [165]. Placing $R_{\mathrm{par}} = R_7 \parallel R_8 \parallel R_9$, the transfer function from v_{linear} over r_{D2} becomes.

$$H_{\mathrm{D2}}(s) = \frac{C_4 r_{\mathrm{D3}} s (C_5 r_{\mathrm{D2}} R_{\mathrm{par}} s + r_{\mathrm{D2}} + R_{\mathrm{par}})}{C_4 C_5 r_{\mathrm{D3}} r_{\mathrm{D2}} R_{\mathrm{par}} s^2 + (C_4 r_{\mathrm{D3}} (r_{\mathrm{D2}} + R_{\mathrm{par}}) + C_5 R_{\mathrm{par}} (r_{\mathrm{D2}} + r_{\mathrm{D3}})) s + r_{\mathrm{D3}} + r_{\mathrm{D2}} + R_{\mathrm{par}}} \tag{5.7}$$

Now we can use it to find the instantaneous poles for the component values and possible operating voltages we have. The poles of the transfer function from v_{linear} over r_{D3} has the same poles. Finding the exact minimum pole location requires some nonlinear optimization methods which are beyond the scope of this thesis. Instead we use the intuition gained from describing the circuit and make the assumption that at least one pole is highly-damped when either diode is switched-on while the other one is switched-off.

In order to get a rough estimate of the pole location we simulate the full nonlinear circuit shown in Figure 5.11 using SPICE. SPICE itself uses a modified version of the trapezoidal integration rule with varying sample-rate [34]. We use the values obtained there as rough estimates.

We feed the SPICE simulation an input of amplitude of 0.2 V which should give us a rough picture of the range of voltages that we may expect. The sensitivity parameter is varied over its full range. We obtain two data points where one diode is conducting while the other is not. The points are $v_{\mathrm{D1}}, v_{\mathrm{D2}} = 0.8512, -1.6248\,\mathrm{V}$ and $v_{\mathrm{D1}}, v_{\mathrm{D2}} = -1.6485, 0.8622\,\mathrm{V}$.

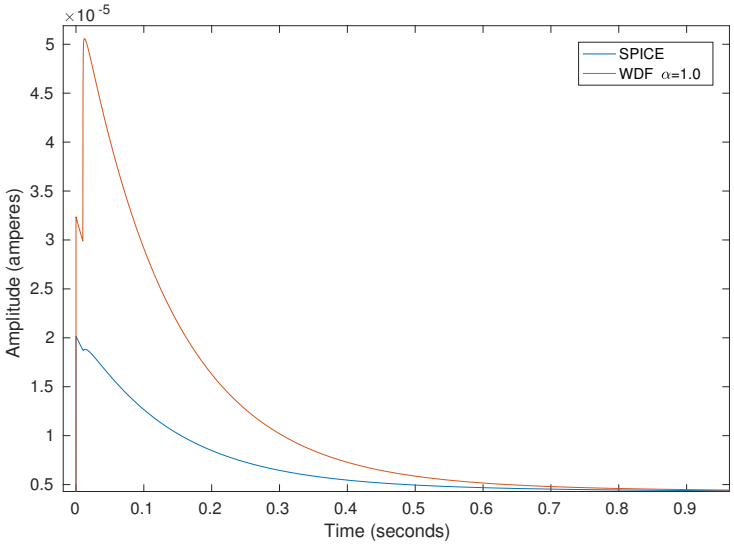

Figure 5.15 *Envelope Follower (Nonlinear Section)—Larger α*

The pole with the maximum damping is located at $\sigma_{\min} = -2.24 \cdot 10^6$ and for a sample rate of 44.1 kHz ($T \approx 22.676\,\mu s$) we get (3.14)

$$\alpha \leq 0.0201 \tag{5.8}$$

It should be noted that damping monotonicity is intrinsically guaranteed if backwards Euler ($\alpha = 0$) is used as the discretization method of choice. We can now feed the derived WDF model with a 0.2 V step function and observe the effect of varying α.

It is apparent from Figures 5.15–5.16 that choosing a proper value for α is crucial if accurate simulations are to be obtained. Applying the standard bilinear transform, without considering the damped poles, will result in a simulation that overshoots the SPICE comparison substantially. α values that are closer to the damping monotonicity criterion result in much more accurate responses when compared to SPICE. One way to get even more accurate responses is to oversample the algorithm. Oversampling effectively increases the allowable bandwidth a processed signal can have without being subjected to aliasing [78].

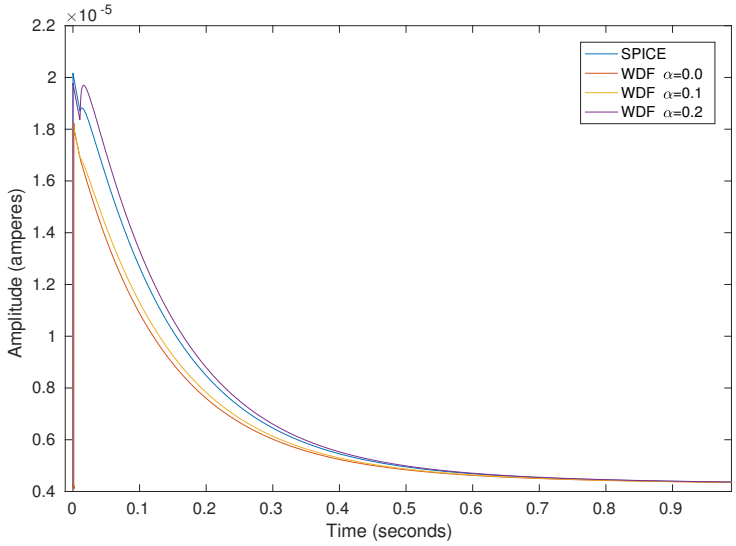

Figure 5.16 *Envelope Follower (Nonlinear Section)—Smaller α*

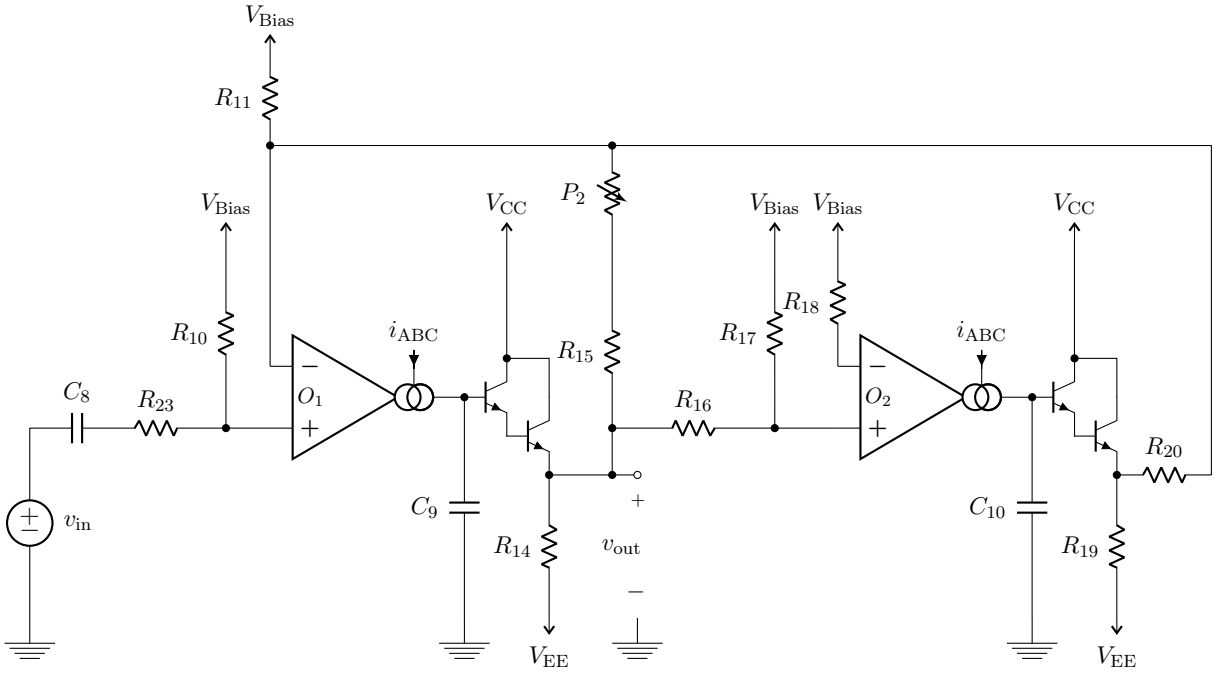

Figure 5.17 *Envelope Filter—Filter Schematic*

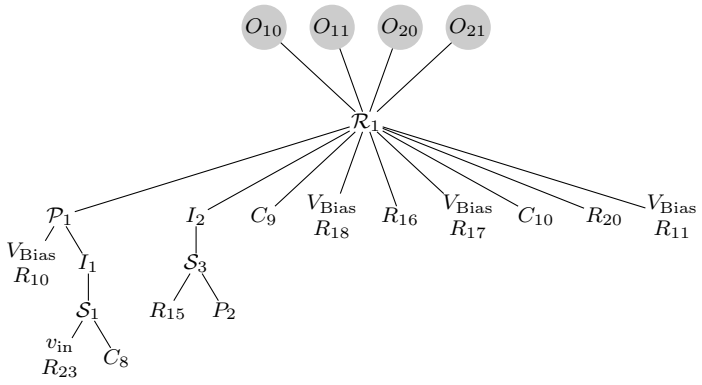

Figure 5.18 *Envelope Filter—Filter Connection Tree*

Table 5.5 *Envelope Filter—Filter Component Values*

Component	Value
R_{23}	10 kΩ
R_{10}, R_{11}, R_{17}, R_{18}	1 kΩ
R_{14}, R_{15}, R_{16}, R_{19}, R_{20}	22 kΩ
P_2	100 kΩ
C_8	1 µF
C_9, C_{10}	10 nF
V_{Bias}	4.5 V
V_{CC}	9 V

5.2.4 Filter Section

The filter section of the envelope filter is shown in Figure 5.17 and corresponding component values shown in Table 5.5. Idealizing the Darlington pair using the steps shown in §4.3 and replacing C_8 with R_{23} (simplifies our algorithm) we end up with the connection tree shown in Figure 5.18. This linear transformation will not change the positive input terminal at O_1 as the values of all components are assumed constant [131]. The calculation of the scattering matrix is shown in a script in §D.

To gain insight into which kind of filter the circuit is realizing we derive its transfer function. We replace the OTA with our ideal VCCS model and assume that i_{ABC} and

the range parameter are constants, i.e., we study the system under LTI conditions. We continue to derive the transfer function using MNA (and the newly derived OTA MNA element stamps).

$$H(s) = \underbrace{H_0}_{\text{Gain}} \quad \underbrace{\frac{s}{s+\omega_\mathrm{c}}}_{\text{Highpass section}} \quad \underbrace{\frac{\frac{\omega_0}{Q_\infty}s}{s^2+\frac{\omega_0}{Q_\infty}s+\omega_0^2}}_{\text{Bandpass filter}} \tag{5.9}$$

The transfer function this circuit realizes is essentially a 1st order highpass filter, composed of components C_8, R_{10}, R_{23}, cascaded with a 2nd order bandpass filter. To simplify the expression of the transfer function, components with identical values are grouped together, $R_\mathrm{a} = R_{23}$, $R_\mathrm{b} = R_{10}, R_{11}, R_{14}, R_{17}, R_{18}, R_{19}$, $R_\mathrm{c} = R_{15}, R_{16}, R_{20}$, $R_\mathrm{d} = P_2$, $C_\mathrm{a} = C_8$ and $C_\mathrm{b} = C_9, C_{10}$. We define $R_\mathrm{q} = R_c + rR_d$, where $r \in]0, 1]$ determines the range.

$$\omega_\mathrm{c} = \frac{1}{C_\mathrm{a}\left(R_\mathrm{a}+R_\mathrm{b}\right)} \tag{5.10}$$

$$H_0 = \frac{\frac{R_\mathrm{b}R_\mathrm{c}}{R_\mathrm{q}} + R_\mathrm{b} + R_\mathrm{c}}{3\left(R_\mathrm{a}+R_\mathrm{b}\right)} \tag{5.11}$$

$$\omega_0^2 = \frac{R_\mathrm{b}^2\, g_\mathrm{m}^2}{C_b^2\left(R_\mathrm{b}+R_\mathrm{c}\right)\left(\frac{R_\mathrm{b}R_\mathrm{c}}{R_\mathrm{q}} + R_\mathrm{b} + R_\mathrm{c}\right)} \tag{5.12}$$

$$Q_\infty = \frac{R_\mathrm{q}}{R_\mathrm{c}}\sqrt{\frac{\frac{R_\mathrm{b}\,R_\mathrm{c}}{R_\mathrm{q}} + R_\mathrm{b} + R_\mathrm{c}}{R_\mathrm{b}+R_\mathrm{c}}}\,. \tag{5.13}$$

Interestingly R_q, controlled by the range, influences all parameters of the transfer function except ω_c. The transconductance, g_m, whose highest value can be set by the sensitivity knob in the envelope follower section, only influences the center frequency. That means that the filter is a constant-Q filter with respect to the transconductance, surely a desirable trait when sweeping the frequency spectrum.

Comparison of Bode plots with three amplifier bias currents $i_\mathrm{ABC} = \{6, 60, 600\}\,\mu\mathrm{A}$ and four range settings $r = \{0.01, 0.22, 0.6, 1.0\}$ are shown in Figure 5.19. The input is supplied

via the ideal voltage source, v_{bp}, and output is taken at v_{out} in Figure 5.17.

The ideal OTA based circuit shows excellent results when compared to the transfer function. The only visible difference between the two happens as the frequency approaches the Nyquist frequency where the warping effects from the bilinear transform become noticeable. The plot of the macromodel is in good accordance with a component-level SPICE model where the magnitude spectrum matches almost exactly throughout the range of amplifier bias currents and range controls. There are minor differences in the location of critical frequencies and bandwidth between the two plots in Figure 5.19.

We briefly study the circuit's behavior under time-varying conditions. The input is a 440 Hz sawtooth, r, the parameter controlling the range, is set to 0.01 and i_{ABC} is increased linearly over time as indicated in the first row of Figure 5.20. In the second row of the same figure a comparison of a SPICE simulation of the filter circuit composed of an ideal OTA simulated using SPICE is compared to the ideal OTA WDF. The third row compares the ideal and macromodel WDFs to a component-level model of the LM13700 OTA as simulated in SPICE. Despite the assumptions of (4.12) and idealizing Darlington pairs as ideal buffers, good results are obtained. The clipping behavior of the OTA (4.11) will have a more pronounced effect as the amplitude of the input is increased. This will cause the differences between the simulations from the component-level SPICE model and the WDFs to deviate more at higher amplitudes than at lower ones.

The input signal to the envelope filter circuit is meant to be a guitar pickup and so the clipping behavior of the OTAs is almost never reached. For the next circuit we study, this is not the case and we will show how the saturated OTA model compares to the ideal OTA model and how it influences the resulting timbre.

5.3 Korg MS-20 Filter

The filter of the Korg MS-20 synthesizer [57] is renowned for its gritty characteristics. Here we study the circuitry that realizes the filter and derive a WDF model of it.

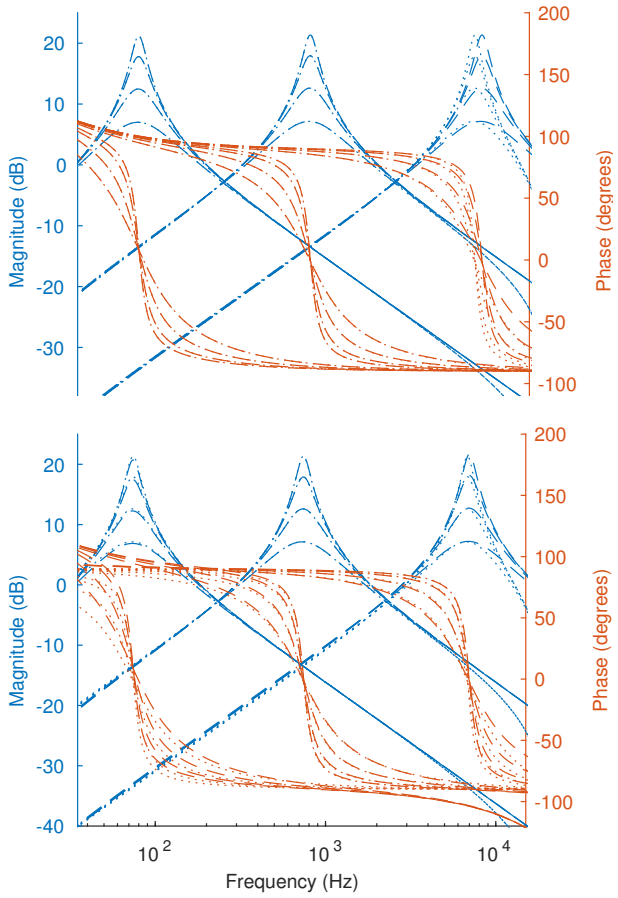

Figure 5.19 *Bode plot comparison of magnitude (blue) and phase (orange) spectra. Upper plot compares the ideal OTA transfer function (dashed lines) and WDF model (dotted lines). Lower plot compares the component-level SPICE model of the LM13700 (dashed lines) with a macromodel-based model (dotted lines).*

The filter section of the Korg MS-20 can be seen in Figure 5.21. It's inner workings has already been studied by Stinchcombe [154]. Stinchcombe derives an approximate transfer function of the filter by idealizing the behavior of the OTA, op-amps and Darlington pairs Q_{D1} and Q_{D2} and removing the antiparallel diodes APD. He also makes several approximations, such as neglecting influence from C_7 and assuming that $C_4 = C_5$, $R_{19} = R_{22} = R_{24} = R_{27}$, $R_{19} \gg R_{21}$ and $R_{24} \gg R_{26}$. Under these assumptions the transfer

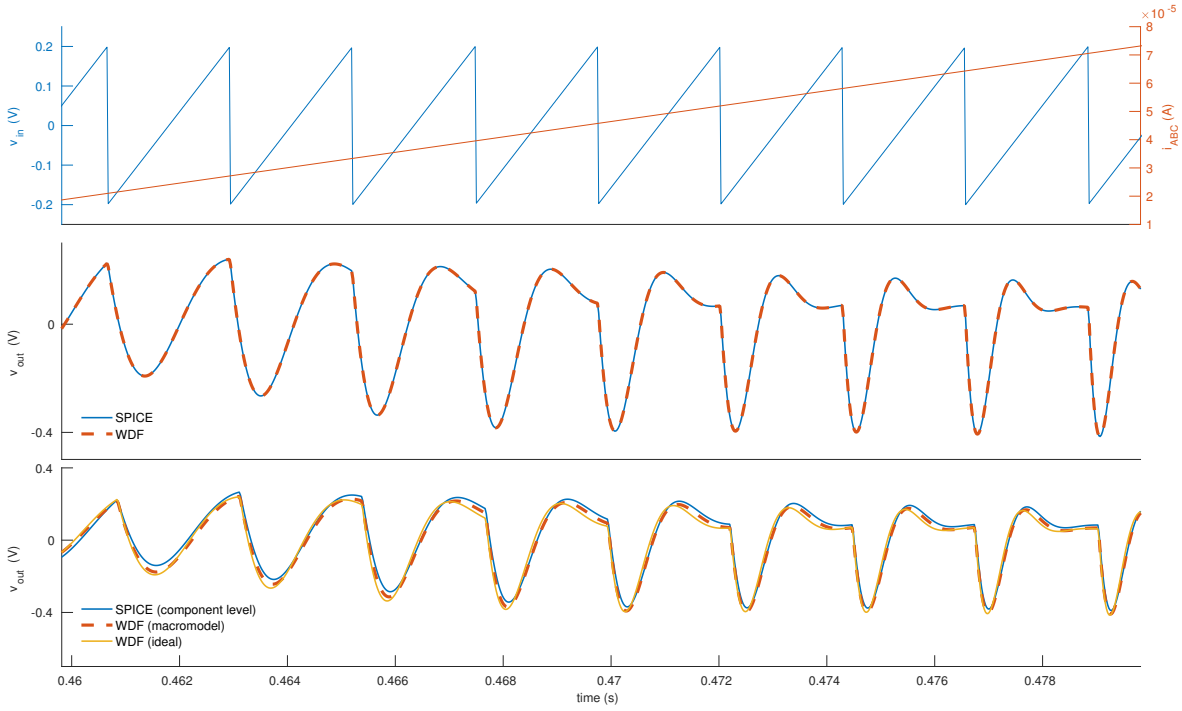

Figure 5.20 *Envelope Filter—Simulation Under Time-Varying i_{ABC}*

function becomes a simple 2nd-order lowpass filter

$$H(s) = \frac{V_{\text{out}}(s)}{V_{\text{in}}(s)} = \frac{\omega_c^2}{s^2 + \frac{\omega_c}{Q_\infty} s + \omega_c^2} \tag{5.14}$$

where

$$\omega_c^2 = \frac{g_m}{(2 + \frac{R_{19}}{R_{21}})C_1} \tag{5.15}$$

$$Q_\infty = \frac{1}{2 - (1 + \frac{R_{30}}{R_{31}})\frac{R_{29} + qR_q}{qR_q}} \tag{5.16}$$

where $q \in]0, 1]$ is used to determine the quality factor of the filter. The filter may thus be approximated as having individual control over both the cutoff frequency and quality factor.

In order to further verify Stinchcombe's findings we derive the transfer function using

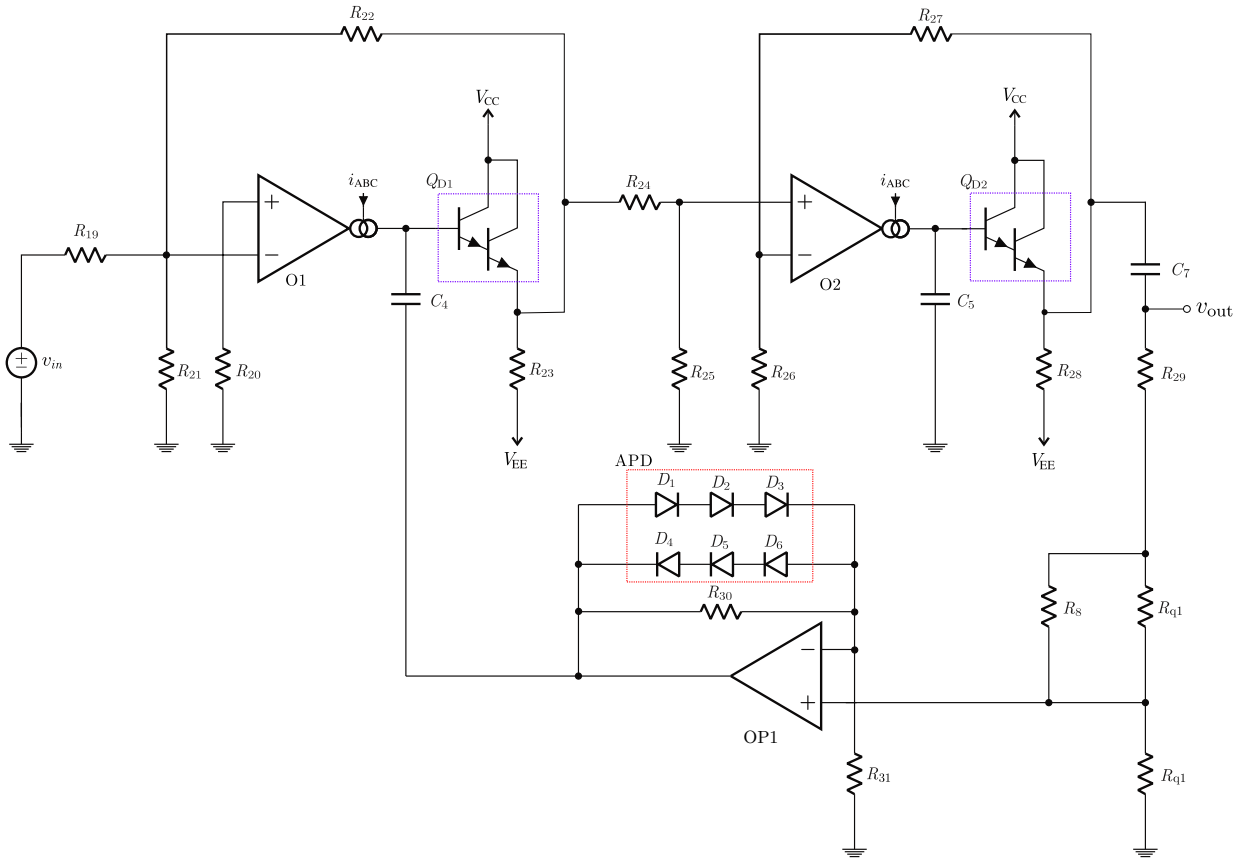

Figure 5.21 *Korg MS-20 Filter—Schematic*

MNA that does not make the same simplifying assumptions. We then compare the two respective derivations for four values of $i_{\text{ABC}} = \{0.4, 4, 40, 400\}$ µA and $q = 1$. For frequencies higher than around 10 Hz, Stinchcombe's derived transfer function is in pretty good agreement with the MNA based derivation for the given ABC currents (Figures 5.22-Figure 5.23). One possible reason is that Stinchcombe disregards the effects from the output coupling capacitor C_7.

Recently another synthesizer filter in the MS synthesizer series by Korg, the Korg MS-50, was studied in the WDF domain by Rest *et al.* [166]. The MS-50 features a Sallen-Key filter topology built around a voltage controllable diode bridge while the MS-20 does not have a pure Sallen-Key filter topology due to the buffers (Darlington-pairs) in its feed-forward path.

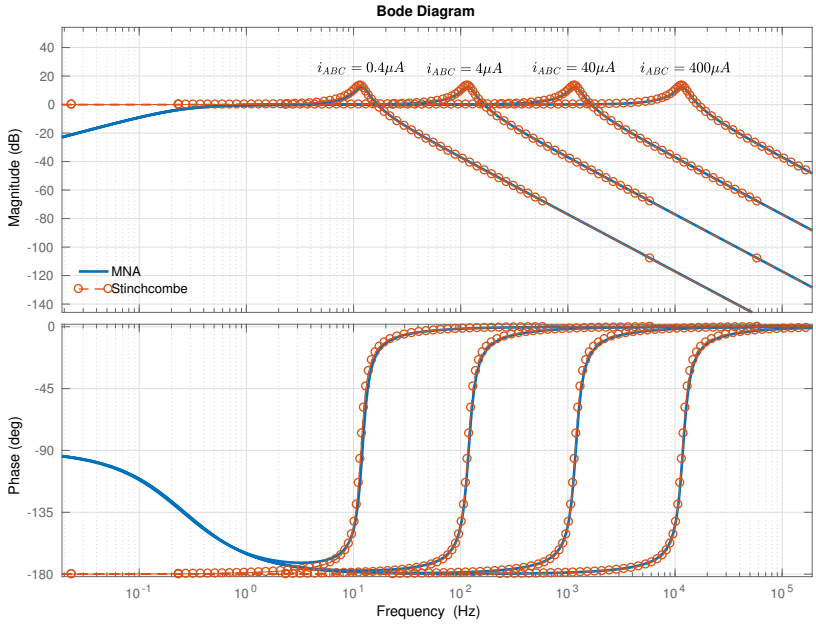

Figure 5.22 *Korg MS-20 Filter—Bode Plot Comparison*

Deriving a WDF model of this circuit follows. We begin by making simplifications to the circuit schematics. Darlington buffers Q_{D1}, Q_{D2} are made into ideal buffers (Figure 4.7) and the operational amplifier OP_1 is idealized as a nullor. First we idealize the behavior of the OTA, only later including the clipping/saturation effects.

We glance at the schematic for ways to divide the topology of the circuit down to known connections and components. One connection tree is shown in Figure 5.24. Deriving the scattering matrices is done as before (§§2.2.4–2.2.5), see §D for a script that calculates the scattering matrix.

5.3.1 Comparison to SPICE

To access the accuracy of the derived model we first simulate it with a single-partial audio signal (Figure 5.25) where it is easy to see the effects of the anti-parallel didoes in the

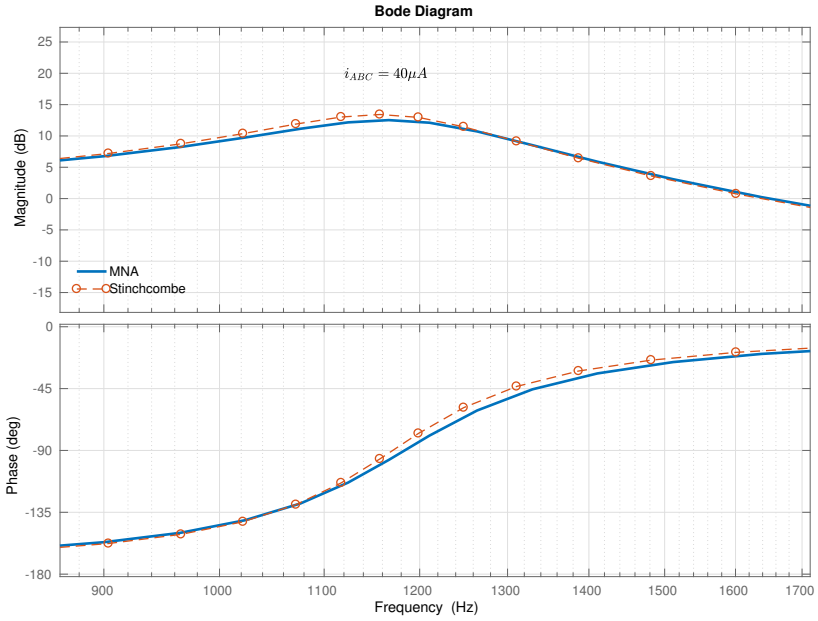

Figure 5.23 *Korg MS-20 Filter—Bode Plot Comparison (Zoom)*

feedback path; the odd harmonics are much more dominant than the even ones. Next we simulate a multi-partial audio signal (Figures 5.26–5.27). In all cases the WDF simulation compares well to that of SPICE.

Ideal OTA vs Saturation Model OTA

Next we compare a simulation using the ideal OTA model with that of the saturation model. In Figure 5.28 the input signal is a 1 V peak antialiased sawtooth wave and we see that there is not a substantial effect by including the saturation OTA model (circle markers show peaks of the ideal OTA model). However when the input signal is a 4.5 V peak antialiased sawtooth wave the spectrum changes substantially when the saturation OTA model is included (Figure 5.29)

Table 5.6 *Korg MS-20 Audio Circuit—Component Values*

Component	Value
R_8	$2.2\,\mathrm{k}\Omega$
R_{19}, R_{22}, R_{24}, R_{27}, R_{30}, R_q	$10\,\mathrm{k}\Omega$
R_{20}, R_{21}, R_{25}, R_{26}	$220\,\Omega$
R_{29}	$8.2\,\mathrm{k}\Omega$
R_{31}	$3.3\,\mathrm{k}\Omega$
C_4, C_5	$2.2\,\mathrm{nF}$
C_7	$33\,\mu\mathrm{F}$
V_{CC}	$15\,\mathrm{V}$
V_{EE}	$-15\,\mathrm{V}$

5.4 Summary

In this chapter we applied the theory reviewed and developed in the previous chapters to derive WDF algorithms of three nonlinear audio circuits. Simulations were in good agreement tried-and-true circuit simulation software SPICE, both in the frequency- and time-domains.

The issue of discretization under time-varying conditions was discussed, most notably in the context of an envelope filter circuit as well as a nonlinear envelope follower circuit.

In this chapter we have used SPICE as a ground-truth for comparison. As we saw we obtained results that most certainly compare to SPICE. However, the algorithm behind SPICE §C is not possible to extend to real-time since the operations needed can not be bounded beforehand [34]. This we can do with our current WDF framework. Additionally, in our simulations we noticed that for similar parameters we found that simulations from the WDF algorithm resulted in a lower noise-floor for all simulations we ran.

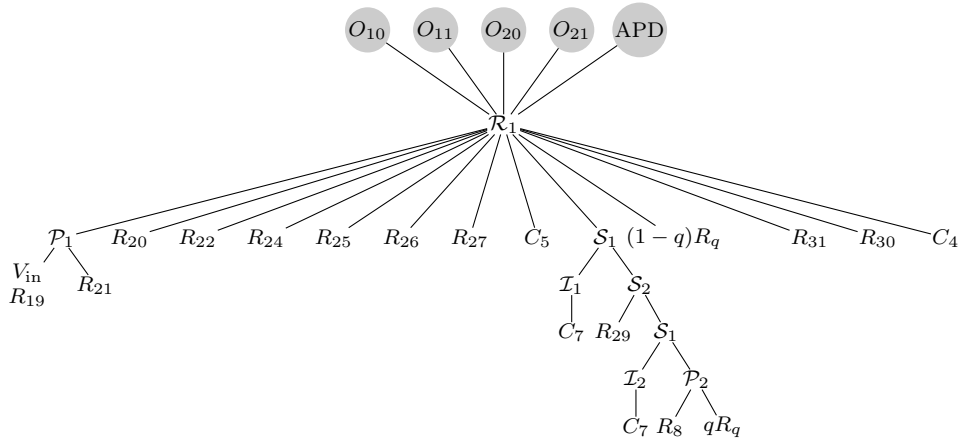

Figure 5.24 *Korg MS-20 Filter—Connection Tree*

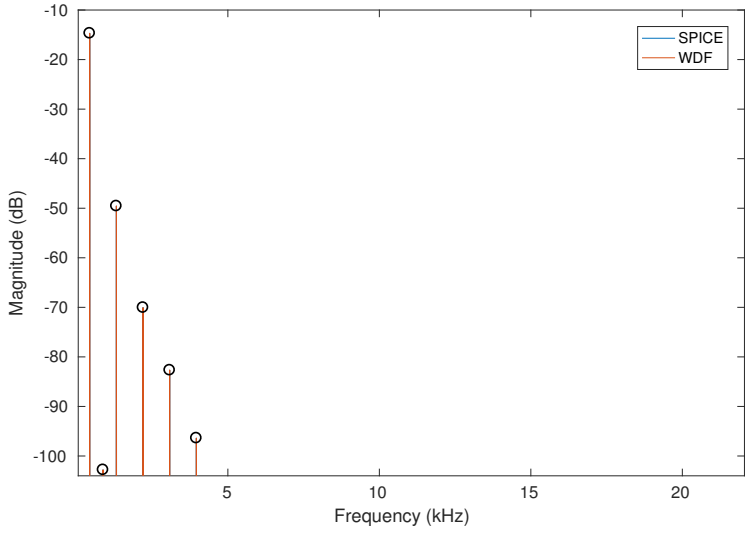

Figure 5.25 *Korg MS-20 Filter*—440 Hz *Sine Input,* $i_{ABC} = 100\,\mu\text{A}$, $q = 0.5$. *16x Oversampling.*

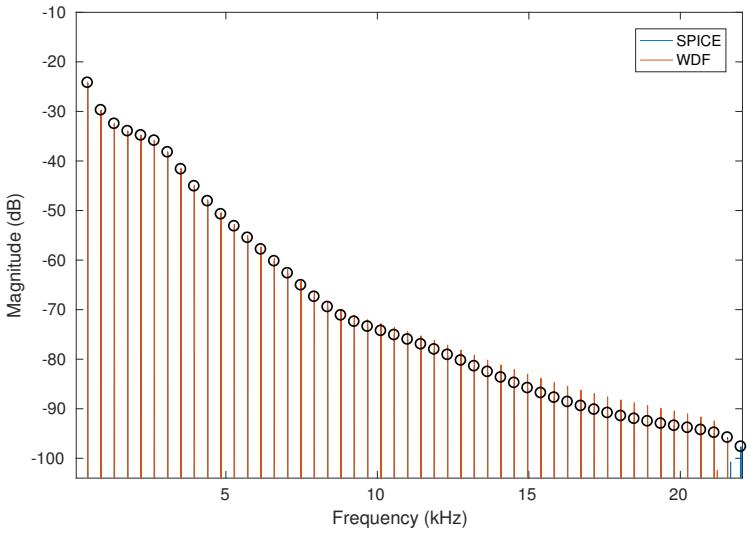

Figure 5.26 *Korg MS-20 Filter*—440 Hz *Antialiased Sawtooth Input,* $i_{ABC} = 100\,\mu\text{A}$, $q = 0.5$. *16x Oversampling.*

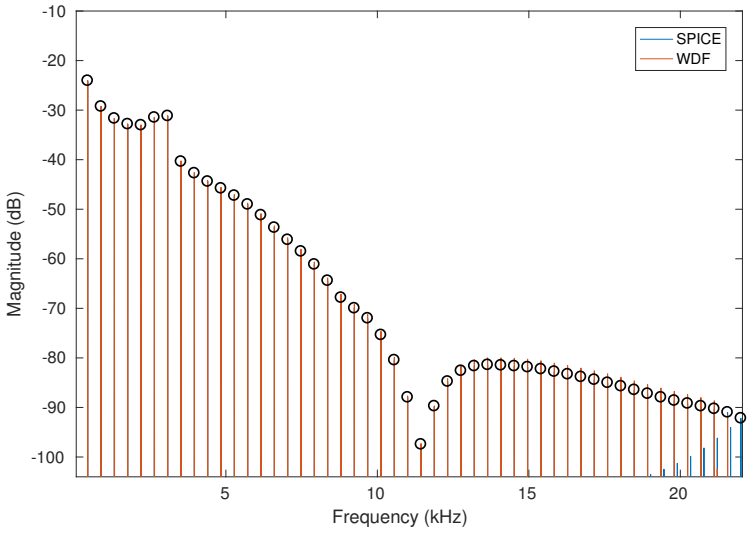

Figure 5.27 *Korg MS-20 Filter*—440 Hz *Antialiased Sawtooth Input,* $i_{ABC} = 100\,\mu\text{A}$, $q = 0.15$. *16x Oversampling.*

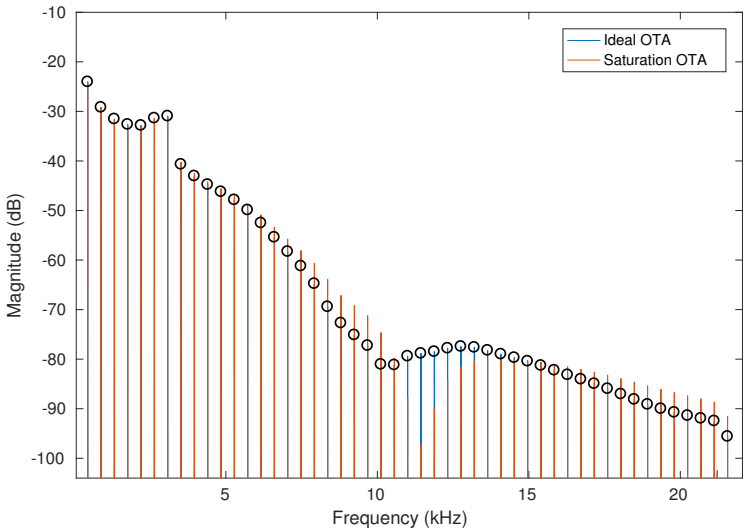

Figure 5.28 *Korg MS-20 Filter*—440 Hz *Antialiased Sawtooth Input,* $i_{ABC} = 100\,\mu\text{A}$, $q = 0.15$. *Comparing Ideal OTA vs Saturated. 16x Oversampling.*

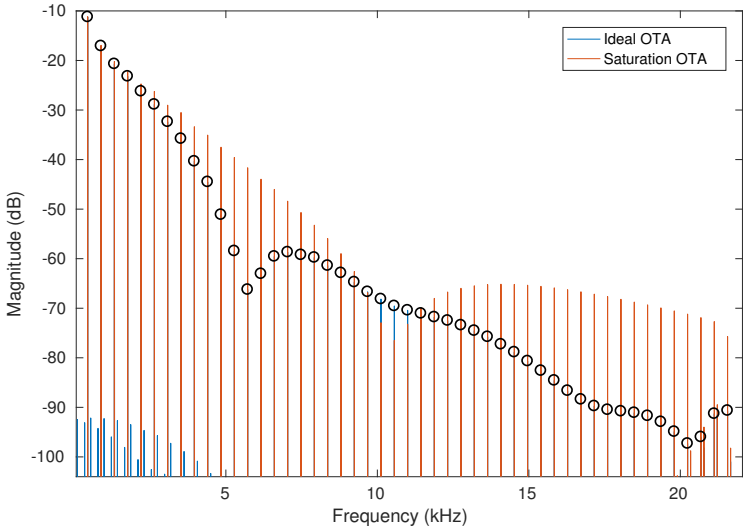

Figure 5.29 *Korg MS-20 Filter*—440 Hz *Antialiased Sawtooth Input,* $i_{ABC} = 100\,\mu\text{A}$, $q = 0.15$. *Comparing Ideal OTA vs Saturated. 16x Oversampling. High-level input signal.*

Chapter 6

Conclusion

6.1 Summary

In this thesis our main goal was to study the modeling and simulation of nonlinear circuits using the wave digital filter (WDF) formalism. We began our study by reviewing current research trends within the field of Virtual Analog. Special emphasis was placed on WDFs, their historical developments and recent advances that have opened the formalism up to model almost any audio circuits (complex topologies, arbitrary number of nonlinear elements).

We studied WDFs under time varying conditions. The WDF literature is sparse on this topic. While stability is guaranteed for passive circuits, it was shown that blindly following the WDF literature [22, 134, 135] may result in inaccurate simulations. The choice of connection tree, wave variable and discretization method were pointed out as essential pieces when developing a WDF algorithm of a time-varying circuit. Furthermore the issue of time-varying reactances and their inherent ambiguity under time-varying conditions was addressed. Models of guaranteed-passive time-varying reactive elements were also presented.

The Zener diode, FET transistor and operational transconductance amplifier, all nonlinear components ubiquitous in audio circuits were introduced into the WDF formalism to circuit modeling. Methods on how to incorporate them into WDF structures were given.

The newly derived models of the nonlinear components were put into use in the last chapter of this thesis. Three audio circuits, containing the nonlinear components, were modeled using the WDF formalism. This resulted in the first simulation of these audio circuits by use of the WDF paradigm. Simulations were shown to be in good agreement with tried-and-true circuit simulation software SPICE, both in frequency and time domains.

6.2 Future Work

There are several topics that were touched upon in this thesis that would be interesting to cover in greater depth in the future:

Time-Varying Reactive Elements As pointed out in §3.4 there is an inherent ambiguity when simulating reactive elements. This seems to arise from the derivation as achieved through the assumptions made by circuit theory §A.1. Since reactances depend on spatial dimensions it is unclear whether accurate simulations may be achieved in the lumped case.

***s*-to-*z* Plane Mappings versus Numerical Schemes** s-to-z plane mappings are only valid under LTI conditions in which case they can be shown to be equivalent to proper numerical schemes. Accuracy and stability analysis done on numerical schemes (§A.2) also assumes LTI.

Comparison to Actual Hardware Although we did not have the chance to do so in this thesis, we hope to further verify the accuracy of our derived models by comparing them to the hardware they set to model.

Plugin Development The software developed during the writing of this thesis may be easily extended to an audio plugin so that musicians can use it in real time.

Appendix A

Lumped Element Models and Their Discretization

A.1 Approximating Field Equations

In order to faithfully emulate vintage audio gear we must understand the limitations of the models we choose to use. By outlining their derivation we get a chance to understand the assumptions that go into their design [1]. Circuit theory is based on the lumped element assumption/lumped matter discipline of the Maxwell equations [99]. The fundamental laws that must hold for every electric circuit are Kirchoff's current and voltage laws (KCL and KVL).

Kirchoff's Voltage Law

It is straightforward to derive Kirchoff's current law from Faraday's law which states that the voltage induced in a closed loop is proportional to the rate of change of magnetic flux that the loop encloses. In integral form Faraday's law reads

$$\oint_{\partial A} \vec{E} \cdot d\vec{r} + \frac{d}{dt} \int_A \vec{B} \cdot d\vec{A} = 0. \tag{A.1}$$

[1] The derivation was adapted from an explanation provided on Stack Exchange

Where $\vec{E}$ is the electric field, $\vec{B}$ is the magnetic field, A is some surface and ∂A is its boundary which can be split up into partial paths $\bigcup_k C_k = \partial A$. Taking this notation into account we obtain

$$\sum_k \int_{C_k} \vec{E} \cdot d\vec{r} + \frac{d}{dt} \int_A \vec{B} \cdot d\vec{A} = 0. \tag{A.2}$$

Voltage drops are defined as $V_k \triangleq \int_{C_k} \vec{E} \cdot d\vec{r}$ and magnetic flux as $\Phi \triangleq \int_A \vec{B} \cdot d\vec{A}$

$$\sum_k V_k = -\frac{d}{dt}\Phi. \tag{A.3}$$

If $-\frac{d}{dt}\Phi \equiv 0$ we obtain Kirchoff's voltage law

$$\sum_k V_k \equiv 0. \tag{A.4}$$

That is voltage drops within a closed loop must always sum to zero.

Kirchoff's Current Law

Kirchoff's current law is derived from Ampere's law which states that the magnetic field induced around a closed loop is proportional to the electric current plus displacement current (rate of change of electric field) that the loop encloses. In integral form we have

$$\oint_{\partial A} \vec{H} \cdot d\vec{r} = \int_A \vec{J} \cdot d\vec{A} + \int_A \frac{d}{dt}\vec{D} \cdot d\vec{A}. \tag{A.5}$$

Where $\vec{H}$ is the magnetic field strength, $\vec{D}$ is the electric displacement and $\vec{J}$ is the current density. If we choose a closed surface A, the boundary ∂A becomes empty

$$\oint_{\partial A} \vec{H} \cdot d\vec{r} \equiv 0. \tag{A.6}$$

Ampere's law for the closed surface then becomes

$$\oint_A \vec{J} \cdot d\vec{A} + \oint_A \frac{d}{dt}\vec{D} \cdot d\vec{A} = 0. \tag{A.7}$$

If we now dissect the surface into two partial surfaces, A_k conductor cross-sections and A_i insulator partial boundary. The current through A_k is defined by $I_k := \int_{A_k} \vec{J} \cdot d\vec{A}$. Additionally we define *charge transfer currents* from both the conductor cross-sections $I_{C_k} \triangleq \int_{A_k} \frac{d}{dt}\vec{D} \cdot d\vec{A}$ and insulator cross-sections $I_i \triangleq \int_{A_i} \frac{d}{dt}\vec{D} \cdot d\vec{A}$. Ampere's law for the bound surface is then

$$\sum_k I_k + \sum_k I_{C_k} + I_i = 0. \tag{A.8}$$

If we now assume that there are no charge transfer currents $\sum_k I_{C_k} \equiv 0$, $I_i \equiv 0$ we obtain the familiar Kirchoff current law

$$\sum_k I_k \equiv 0. \tag{A.9}$$

Discussion

The underlying assumptions of Kirchoffs' laws are equivalent to the ones of the lumped element model. That is to say that the electric field in a circuit is stored in its entirety within capacitors while the total magnetic field is stored within inductors. This suggests that the lumped element model assumes that no energy is lost in electromagnetic radiation.

A.1.1 Dynamical Systems Analogies

Lumped dynamical systems are characterized by variable pairs known as across/through or effort/flow pairs. In the electrical context these variables are voltage/current. Examples of other types of systems that can be modeled as lumped systems include acoustical and mechanical rotational ones [30].

Equivalences among these domains can be drawn using two different kinds of analogies: the conventional analogy [30], or the Firestone analogy [29] (maintains topology). An example of a common analogy made between lumped systems is in the study and design of loudspeakers (electro-acoustic transducers) as equivalent electrical circuits [32].

A.2 Numerical Discretization Schemes

In WDF theory components are discretized locally, one component at a time. By retaining a circuit's topology through the discretization phase, energy conservation laws are inherited.

Below we will give stability and accuracy analysis for well known numerical discretization schemes, assumed to be applied locally. The notation and general procedure of [137] is adapted here. Given a differential equation

$$\frac{dy}{dt} = f(y,t) \tag{A.10}$$

we linearize it around a given operating point (t_0, y_0) and perform a two-dimensional Taylor series expansion

$$f(y,t) = f(y_0,t_0) + (t-t_0)\,\frac{\partial f}{\partial t}(y_0,t_0) + (y-y_0)\,\frac{\partial f}{\partial y}(y_0,t_0) + \cdots \tag{A.11}$$

The *model problem* is a simplification of the Taylor series expansion where constants, nonlinear terms, and terms related to the implicit time derivative are discarded. What results is a much simpler and malleable equation

$$\frac{dy}{dt} = \frac{\partial f}{\partial y}(y_0,t_0)\,y(t) = \lambda y(t). \tag{A.12}$$

This equation is arguably the simplest differential equation there is, with a solution in the form of $y(t) = y_0 e^{\lambda t}$, that leads to a discretized version that reads

$$y(t_n) = y_0(e^{\lambda T})^n = y_0\,(1 + \lambda T + \frac{\lambda^2 T^2}{2!} + \frac{\lambda^3 T^3}{3!} + \cdots)^n = y_0\,\sigma^n \tag{A.13}$$

where $y(0) = y_0$, T is the *sampling interval* and σ is known as the *amplification constant*. λ is assumed complex with a non-positive real part. The *phase error* is defined as the difference between the phase of the exact solution (A.13) and that of a particular numerical scheme [137].

When determining the phase error, λ is assumed purely imaginary $\lambda = i\,\omega$ and $y(0) = 1$. In that special case when the amplitude of the exact solution is $|y(t)| = 1$ the phase becomes $\mathrm{Arg}(y(t)) = \omega T$.

Table A.1 *Numerical Schemes*

Scheme	Stability	σ	Phase Error
Exact Solution	N/A	$e^{\lambda T} = 1 + \lambda T + \frac{\lambda^2 T^2}{2!} + \frac{\lambda^3 T^3}{3!} + \frac{\lambda^4 T^4}{4!} + \cdots$	N/A
Forward Euler	Cond. stable	$1 + \lambda T$	$\frac{(\omega T)^3}{3} + \cdots$
Backward Euler	Stable	$\frac{1}{1\ \ \lambda T} = 1 + \lambda T + \lambda^2 T^2 + + \lambda^3 T^3 + \cdots$	$\frac{(\omega T)^3}{3} + \cdots$
Trapezoidal Method	Stable	$\frac{1+\lambda T/2}{1\ \ \lambda T/2} = 1 + \lambda T + \frac{\lambda^2 T^2}{2} + \frac{\lambda^3 T^3}{4} + \cdots$	$\frac{(\omega T)^3}{12} + \cdots$
2nd-order Runge-Kutta	Cond. stable	$1 + \lambda T + \frac{\lambda^2 T^2}{2!}$	$-\frac{(\omega T)^3}{3!} + \cdots$
4th-order Runge-Kutta	Cond. stable	$1 + \lambda T + \frac{\lambda^2 T^2}{2!} + \frac{\lambda^3 T^3}{3!} + \frac{\lambda^4 T^4}{4!}$	$\frac{(\omega T)^5}{5!} + \cdots$

A.2.1 Stability

Explicit methods, such as the forward Euler method are known to be conditionally stable or not stable at all. For a numerical method to be conditionally stable means that their stability hinges on properties of the differential equation itself. In general one can derive a stability region where $|\sigma| \leq 1$ which means that the solution to (A.12) remains bounded. The resulting region of stability usually depends on the sampling interval and λ. Stability of the Forward Euler method is for example guaranteed only if $T \leq 2/|\lambda|$ and λ is not purely imaginary.

A.2.2 Accuracy

Numerical schemes are generally classified by their *order of accuracy*. A method is said to be of α-order if its amplification factor matches all terms up to and including the $\lambda^\alpha T^\alpha/\alpha!$ in A.12. Comparing the amplification factors in Table A.1 to (A.13) we see that the Euler methods are 1st-order accurate, the trapezoidal method and 2nd-order Runge-Kutta are 2nd-order accurate while the 4th-order Runge-Kutta is considered 4th-order accurate. Order of accuracy gives an upper bound on the accuracy of the numerical scheme.

The 4th-order Runga-Kutta is the most accurate numerical scheme listed here. This increase in accuracy is a result of the four function evaluations it does per time step, as

Mapping	$z \mapsto s = f(z)$	$s \mapsto z = f^{-1}(s)$
Forward Euler	$s = f_{\mathrm{FE}}(z) = \frac{1}{T}(z-1)$	$z = f_{\mathrm{FE}}^{-1}(s) = 1+Ts$
Backward Euler	$s = f_{\mathrm{BE}}(z) = \frac{1}{T}(z-1)$	$z = f_{\mathrm{BE}}^{-1}(s) = \frac{1}{1-Ts}$
Bilinear Transform	$s = f_{\mathrm{BT}}(z) = \mu\frac{1-z^{-1}}{1+z^{-1}}$	$z = f_{\mathrm{BT}}^{-1}(s) = \frac{1+s\mu}{1-s\mu}$
α Transform	$s = f_{\alpha}(z) = \frac{\frac{1+\alpha}{T}-\frac{1+\alpha}{T}z^{-1}}{1+\alpha z^{-1}}$	$z = f_{\alpha}^{-1}(s) = -\frac{\alpha s+\frac{1+\alpha}{T}}{s-\frac{1+\alpha}{T}}$
Möbius Transform	$s = f_{\mathrm{M}}(z) = \frac{a+bz^{-1}}{c+dz^{-1}}$	$z = f_{\mathrm{M}}^{-1}(s) = -\frac{ds-b}{cs-a}$

Table A.2 *s-Plane to z-Plane Spectral Mappings*

opposed to two as the trapezoidal and 2nd-order Runge-Kutta methods do.

A.3 s-Plane to z-Plane Mappings

In engineering, the (unilateral) Laplace transform is an useful tool for solving systems that are described by linear ordinary differential equations (ODE) with constant coefficients [78]. The Laplace transform is defined for a given function $f(t)$ by the integral

$$F(s) = \mathscr{L}\{f(t)\} = \int_{0^-}^{\infty} f(t)e^{-st}dt \tag{A.14}$$

where $s = \sigma + j\Omega$ is the complex frequency. Using the Laplace transform on a single-input single-output (SISO) LTI system will result in the transfer function

$$H(s) = \frac{Y(s)}{U(s)} = \frac{\sum_{m=1}^{M} b_m s^m}{\sum_{n=1}^{N} a_n s^n} \tag{A.15}$$

where $Y(s)$ and $U(s)$ are Laplace transforms of the output and input respectively. A transfer function uniquely describes the relationship between the input and output of a LTI system in the special case when the input and its derivatives are taken to be zero at $t < 0$.

In the LTI case the Forward Euler, Backward Euler and Bilinear transforms are equivalent to the Forward Euler, Backward Euler and trapezoidal numerical schemes. Where

μ is a tunable parameter for the bilinear transform ($\mu = T/2$ for the canonical bilinear transform). α is similarly the tunable parameter for the α Transform [56]. As the Laplace transform is not defined for nonlinear time-variant systems the s-to-z mappings are not defined for such systems.

A.3.1 Discussion

It is clear that choosing a numerical scheme is a trade-off between accuracy, stability as well as computational complexity (not discussed here). Although more accurate multi-step methods do exist, their increased accuracy usually comes at the price of complexity and stability.

The model problem assumes LTI and so the previous analysis is based on the assumption that the differential equation we are working with are similarly LTI. This is generally not true and the following stability and accuracy analysis should generally be thought of as an upper bound. Moin [137] states that performing analysis on the model problem does not substantially affect the result of the stability analysis.

Passivity, a central concept in WDF theory, can only be guaranteed unconditionally at a global scale if the same applies locally. A recent paper explored the application of the Möbius transform from the study of conformal mapping to numerical schemes [56]. It is shown that the explicit Euler, trapezoidal method and α-transform are all edge cases of the Möbius transform method. The authors also note that the trapezoidal method is the most accurate single-step method that is absolutely stable (A-stable) and that passivity cannot be guaranteed for multi-step methods above order 2 [167]. The Möbius transform is a generalization of the highest order linear multi-step methods applied in the WDF context that guarantee local passivity.

Appendix B

Common WDF Building Blocks

Most of the linear components and connections that we need in order to simulate audio circuits have been known in the wave-domain for a long time [35]. In this appendix we aggregate important WDF elements to the simulation of audio circuits. The discussion takes off with a presentation of one-port components followed by two-port components. Finally we discuss common adaptors and some of their properties.

B.1 Common Components

B.1.1 One-Port Components

One-port components at an arbitrary port 0 are characterized in the Kirchoff-domain by their port voltage v_0 and port current i_0. In the wave domain they are completely charac-

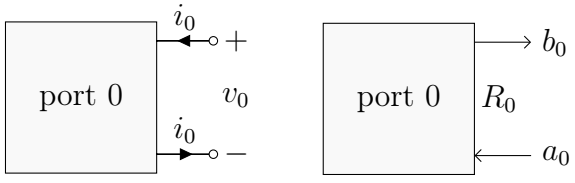

(a) *Kirchoff domain* (b) *Wave domain*

Figure B.1 *Generic One-Port*

terized by an incident wave a_0, reflected wave b_0 and a port-resistance R_0. Signal variables

at some port 0 can be transformed from the Kirchoff domain into the wave domain using

$$\begin{bmatrix} a_0 \\ b_0 \end{bmatrix} = R_0^{\rho} \begin{bmatrix} R_0^{-1} & 1 \\ R_0^{-1} & -1 \end{bmatrix} \begin{bmatrix} v_0 \\ i_0 \end{bmatrix}. \tag{B.1}$$

Note that the common wave variables are proportional up to a given constant value R_0. This proportionality relationship has been termed *quasi-equivalence* [134, 135] and is the reason why the parameter ρ does not show up in any of the one-port WDF components outlined below (except for minor scalings of Kirchoff-domain input sources).

Ideal Voltage Source supplies a voltage $v_0(t) = v(t)$ over its terminal. The port current $i_0(t)$ is sufficiently large such that the voltage over the terminals is correct. The unadapted ideal voltage source in the wave domain is

$$b_0[n] = 2R_0^{\rho-1} v[n] - a_0[n]. \tag{B.2}$$

The ideal voltage source cannot be adapted and must be placed at the root of a connection tree.

Ideal Current Source supplies an arbitrary current $i_0(t) = i(t)$ over its terminal. The unadapted wave domain equation is then

$$b_0[n] = 2R_0^{\rho} i[n] - a_0[n]. \tag{B.3}$$

The ideal current source cannot be adapted and is suitable to be included at the root of a connection tree.

Resistor is characterized by Ohm's law $v_0(t) = Ri_0(t)$ where R is the resistance. The unadapted wave domain equation is

$$b_0[n] = \frac{R - R_0}{R + R_0} a_0[n]. \tag{B.4}$$

By placing $R_0 = R$ we can adapt the resistor which yields the equation for the adapted resistor in the wave-domain

$$b_0[n] = 0. \tag{B.5}$$

Resistive Voltage Source is a series connection of an ideal voltage source supplying

voltage $v(t)$ and resistor with resistance R. It is described at its terminals by $v_0(t) = v(t) + Ri_0(t)$. The unadapted wave domain equation is then

$$b_0[n] = \frac{2R_0^\rho}{R+R_0}v[n] + \frac{R-R_0}{R+R_0}a_0[n]. \tag{B.6}$$

By placing $R_0 = R$ we can adapt the resistive voltage source. The equation for the adapted resistive voltage source in the wave-domain then becomes

$$b_0[n] = R^{\rho-1}v[n]. \tag{B.7}$$

Resistive Current Source is a parallel connection of an ideal current source supplying current $i(t)$ and resistor which has a resistance R. It is completely described at its terminals by $i(t) + i_0(t) = v_0(t)/R$ and in the wave domain by

$$b_0[n] = \frac{2RR_0^\rho}{R+R_0}i[n] + \frac{R-R_0}{R+R_0}a_0[n]. \tag{B.8}$$

Choosing $R_0 = R$ we can adapt the resistive current source just as we did for the resistor and resistive voltage source. The equation for the adapted resistive current source in the wave-domain is then

$$b_0[n] = R^\rho i[n]. \tag{B.9}$$

Capacitor is described in the Kirchoff domain by the differential equation $i_0 = C\frac{dv_0}{dt}$ and in the Laplace domain by $I_0(s) = CsV_0(s)$. The reflectance in the Laplace domain is given by $S_0(s) = \frac{1-R_0Cs}{1+R_0Cs}$. The capacitor has traditionally been discretized using the canonical bilinear transform ($\mu_0 = 2/T$, see Table A.2) which yields the unadapted wave domain relation

$$b_0[n] = -\frac{1-\mu_0R_0C}{1+\mu_0R_0C}b_0[n-1] + \frac{1-\mu_0R_0C}{1+\mu_0R_0C}a_0[n] + a_0[n-1]. \tag{B.10}$$

Letting $R_0 = \frac{1}{\mu_0 C}$ we obtain the adapted wave domain equation

$$b_0[n] = a_0[n-1]. \tag{B.11}$$

Inductor is described in the Kirchoff domain by the differential equation $v_0 = L\frac{di_0}{dt}$ and in the Laplace domain by $V_0(s) = LsI_0(s)$. The reflectance in the Laplace domain is given by

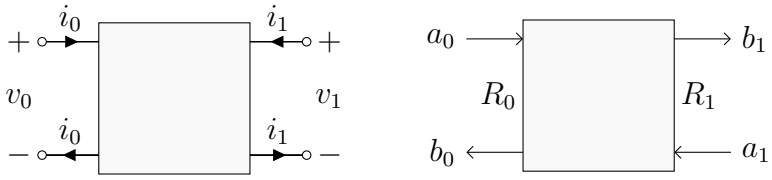

(a) *Kirchoff domain* (b) *Wave domain*

Figure B.2 *Generic Two-Port*

$S_0(s) = \frac{Ls-R_0}{Ls+R_0}$. The inductor has traditionally been discretized using the canonical bilinear transform ($\mu_0 = 2/T$, see Table A.2) which yields the unadapted wave domain relation

$$b_0[n] = \frac{\mu_0 L - R_0}{\mu_0 L + R_0} b_0[n-1] + \frac{\mu_0 L - R_0}{\mu_0 L + R_0} a_0[n] - a_0[n-1]. \tag{B.12}$$

Choosing $R_0 = \mu_0 L$ we obtain the adapted wave domain equation

$$b_0[n] = -a_0[n-1]. \tag{B.13}$$

Although the capacitor and inductor have been discretized using the canonical bilinear transform in the past, it has been shown that any implicit s-to-z mapping can be used. It has similarly been shown that fully explicit discretization schemes ruin the chance for adaptation and cannot be used to digitize WDFs [116].

B.1.2 Two-Port Components

Two-Port components at an arbitrary port 0 and port 1 are completely characterized in the Kirchoff-domain by their port voltages v_0, v_1 and port currents i_0, i_1.
Ideal Transformer is described in the Kirchoff domain as

$$\begin{bmatrix} v_0 \\ i_1 \end{bmatrix} = \begin{bmatrix} m & 0 \\ 0 & -m \end{bmatrix} \begin{bmatrix} v_1 \\ i_0 \end{bmatrix}, \tag{B.14}$$

where m is the ratio between windings in the first and second coil of the transformer. In the wave domain they are described by

$$\begin{bmatrix} b_0 \\ b_1 \end{bmatrix} = \begin{bmatrix} -\frac{R_0 - m^2 R_1}{R_0 + m^2 R_1} & \frac{2m R_0^{\rho} R_1^{1-\rho}}{R_0 + m^2 R_1} \\ \frac{2m R_0^{1-\rho} R_1^{\rho}}{R_0 + m^2 R_1} & \frac{R_0 - m^2 R_1}{R_0 + m^2 R_1} \end{bmatrix} \begin{bmatrix} a_0 \\ a_1 \end{bmatrix}. \tag{B.15}$$

Letting $R_0 = m^2 R_1$ we can adapt port 0 and similarly choosing $R_1 = m^{-2} R_0$ will adapt port 1.

Nullor, also known as a universal amplifier, is a useful theoretical tool to model operational amplifiers [164]. The two port device can be seen as a combination of a nullator and a norator [168]. A nullator is fully characterized at a port 0 by $v_0 = 0$, $i_0 = 0$, while a norator places no restrictions on its port-current or voltage.

An ideal operational amplifier is modeled by the constraint that no current flows between its input terminals or equivalently that the potential difference is zero. The output port sinks/sources enough current such that the constraints at the input port are met. By replacing an operational amplifier with a nullator between its input ports and a norator from its output terminal to ground, an ideal operational amplifier can be constructed from the theoretical one-ports.

Neither nullators nor norators can be converted to the wave-domain. For nullors, the wave-domain equations become $a_0 = b_0 = 0$, while norators place no restrictions on wave-variables at its port.

B.2 Common Adaptors

B.2.1 Two-Port Adaptors

Two-Port Series Adaptor is fully described in the Kirchoff-domain by the following equations

$$\begin{aligned} i_0 &= i_1 \\ v_0 + v_1 &= 0 \end{aligned} \tag{B.16}$$

which is simple to transfer to the wave domain

$$\begin{bmatrix} b_0 \\ b_1 \end{bmatrix} = \begin{bmatrix} -\frac{R_0-R_1}{R_0+R_1} & -\frac{2R_0^{\rho}R_1^{1-\rho}}{R_0+R_1} \\ -\frac{2R_0^{1-\rho}R_1^{\rho}}{R_0+R_1} & \frac{R_0-R_1}{R_0+R_1} \end{bmatrix} \begin{bmatrix} a_0 \\ a_1 \end{bmatrix} \tag{B.17}$$

$$\boldsymbol{b} = \Phi_{\mathcal{S}_2}\, \boldsymbol{a}. \tag{B.18}$$

Adapting port 0 is the same as adapting port 1 which can be achieved by $R_0 = R_1$, which results in the following description

$$\begin{bmatrix} b_0 \\ b_1 \end{bmatrix} = \begin{bmatrix} 0 & -1 \\ -1 & 0 \end{bmatrix} \begin{bmatrix} a_0 \\ a_1 \end{bmatrix}. \tag{B.19}$$

An adapted series adaptor is very useful as a *polarity inverter* [42]. Incorrect polarities are known to negatively alter the behavior of nonlinear circuits.

Two-Port Parallel Adaptor is fully described in the Kirchoff-domain by the following equations

$$\begin{aligned} v_0 &= v_1 \\ i_0 + i_1 &= 0 \end{aligned} \tag{B.20}$$

that is simple to transfer to the wave domain

$$\begin{bmatrix} b_0 \\ b_1 \end{bmatrix} = \begin{bmatrix} -\frac{R_0-R_1}{R_0+R_1} & \frac{2R_0^{\rho}R_1^{1-\rho}}{R_0+R_1} \\ \frac{2R_0^{1-\rho}R_1^{\rho}}{R_0+R_1} & \frac{R_0-R_1}{R_0+R_1} \end{bmatrix} \begin{bmatrix} a_0 \\ a_1 \end{bmatrix} \tag{B.21}$$

$$\boldsymbol{b} = \Phi_{\mathcal{P}_2}\, \boldsymbol{a}. \tag{B.22}$$

B.2.2 Three-Port Adaptors

Three-Port Series Adaptor is fully explained by the following constraint equations

$$\begin{aligned} v_0 &= v_1 = v_2 \\ i_0 + i_1 + i_2 &= 0 \end{aligned}. \tag{B.23}$$

In the wave domain a three-port series adaptor is characterized by the scattering matrix $\Phi_{\mathcal{S}_3}$

$$\begin{bmatrix} b_0 \\ b_1 \\ b_2 \end{bmatrix} = \begin{bmatrix} \frac{R_1 - R_0 + R_2}{R_0 + R_1 + R_2} & -\frac{2\,R_0^{\rho}\,R_1^{1-\rho}}{R_0 + R_1 + R_2} & -\frac{2\,R_0^{\rho}\,R_2^{1-\rho}}{R_0 + R_1 + R_2} \\ -\frac{2\,R_0^{1-\rho}\,R_1^{\rho}}{R_0 + R_1 + R_2} & \frac{R_0 - R_1 + R_2}{R_0 + R_1 + R_2} & -\frac{2\,R_1^{\rho}\,R_2^{1-\rho}}{R_0 + R_1 + R_2} \\ -\frac{2\,R_0^{1-\rho}\,R_2^{\rho}}{R_0 + R_1 + R_2} & -\frac{2\,R_1^{1-\rho}\,R_2^{\rho}}{R_0 + R_1 + R_2} & \frac{R_0 + R_1 - R_2}{R_0 + R_1 + R_2} \end{bmatrix} \begin{bmatrix} a_0 \\ a_1 \\ a_2 \end{bmatrix} \tag{B.24}$$

$$\boldsymbol{b} = \Phi_{\mathcal{S}_3}\,\boldsymbol{a}. \tag{B.25}$$

The i-th port can be adapted setting the i-th port resistance as the sum of the other two. Below is the scattering matrix with the 0-th port adapted.

$$\begin{bmatrix} b_0 \\ b_1 \\ b_2 \end{bmatrix} = \begin{bmatrix} 0 & -\frac{R_1^{1-\rho}}{(R_1+R_2)^{\rho-1}} & -\frac{R_2^{1-\rho}}{(R_1+R_2)^{\rho-1}} \\ -\frac{R_1^{\rho}}{(R_1+R_2)^{\rho-1}} & \frac{R_2}{R_1+R_2} & -\frac{R_1^{\rho}\,R_2^{1-\rho}}{R_1+R_2} \\ -\frac{R_2^{\rho}}{(R_1+R_2)^{\rho-1}} & -\frac{R_1^{1-\rho}\,R_2^{\rho}}{R_1+R_2} & \frac{R_1}{R_1+R_2} \end{bmatrix} \begin{bmatrix} a_0 \\ a_1 \\ a_2 \end{bmatrix}. \tag{B.26}$$

Three-Port Parallel Adaptor is fully explained by the duality of the three-port series constraint equations, that is

$$\begin{aligned} i_0 = i_1 = i_2 \\ v_0 + v_1 + v_2 = 0 \end{aligned}. \tag{B.27}$$

In the wave domain it is characterized by the scattering matrix $\Phi_{\mathcal{P}_3}$

$$\begin{bmatrix} b_0 \\ b_1 \\ b_2 \end{bmatrix} = \begin{bmatrix} -\frac{R_0\,R_1 + R_0\,R_2 - R_1\,R_2}{R_0\,R_1 + R_0\,R_2 + R_1\,R_2} & \frac{2\,R_0^{\rho}\,R_1^{1-\rho}\,R_2}{R_0\,R_1 + R_0\,R_2 + R_1\,R_2} & \frac{2\,R_0^{\rho}\,R_1\,R_2^{1-\rho}}{R_0\,R_1 + R_0\,R_2 + R_1\,R_2} \\ \frac{2\,R_0^{1-\rho}\,R_1^{\rho}\,R_2}{R_0\,R_1 + R_0\,R_2 + R_1\,R_2} & -\frac{R_0\,R_1 - R_0\,R_2 + R_1\,R_2}{R_0\,R_1 + R_0\,R_2 + R_1\,R_2} & \frac{2\,R_0\,R_1^{\rho}\,R_2^{1-\rho}}{R_0\,R_1 + R_0\,R_2 + R_1\,R_2} \\ \frac{2\,R_0^{1-\rho}\,R_1\,R_2^{\rho}}{R_0\,R_1 + R_0\,R_2 + R_1\,R_2} & \frac{2\,R_0\,R_1^{1-\rho}\,R_2^{\rho}}{R_0\,R_1 + R_0\,R_2 + R_1\,R_2} & -\frac{R_0\,R_2 - R_0\,R_1 + R_1\,R_2}{R_0\,R_1 + R_0\,R_2 + R_1\,R_2} \end{bmatrix} \begin{bmatrix} a_0 \\ a_1 \\ a_2 \end{bmatrix} \tag{B.28}$$

$$\boldsymbol{b} = \Phi_{\mathcal{P}_3}\,\boldsymbol{a}. \tag{B.29}$$

The i-th port can be adapted setting the i-th port conductance (inverse of port resistance)

as the sum of the other two port conductances. Below is the scattering matrix with the 0-th port adapted with $G_0 = G_1 + G_2$

$$\begin{bmatrix} b_0 \\ b_1 \\ b_2 \end{bmatrix} = \begin{bmatrix} 0 & \frac{R_2^\rho}{(R_1+R_2)^\rho} & \frac{R_1^\rho}{(R_1+R_2)^\rho} \\ \frac{R_2^{1-\rho}}{(R_1+R_2)^{1-\rho}} & -\frac{R_1}{R_1+R_2} & \frac{R_1^\rho R_2^{1-\rho}}{R_1+R_2} \\ \frac{R_1^{1-\rho}}{(R_1+R_2)^{1-\rho}} & \frac{R_1^{1-\rho} R_2^\rho}{R_1+R_2} & -\frac{R_2}{R_1+R_2} \end{bmatrix} \begin{bmatrix} a_0 \\ a_1 \\ a_2 \end{bmatrix}. \tag{B.30}$$

B.2.3 *N*-Port Adaptors

N-port series or parallel adaptor can be split into $N-2$ series or parallel adaptors. Decomposing larger adaptors into smaller ones has been shown to reduce computational complexity [38].

B.2.4 Norm Preservation

It is easy to see that for valid 3-port adaptors, $\text{rank}(\Phi_{\mathcal{S}_3}) = \text{rank}(\Phi_{\mathcal{P}_3}) = 3$. Since the matrices are square and nonsingular (of full rank), the columns of $\Phi_{\mathcal{S}_3}$ and $\Phi_{\mathcal{P}_3}$ form a basis. When using normalized-power waves ($\rho = \frac{1}{2}$) Kubin [134] noticed that

$$\Phi_{\mathcal{S}_3}\Phi_{\mathcal{S}_3}^* = \Phi_{\mathcal{P}_3}\Phi_{\mathcal{P}_3}^* = I \tag{B.31}$$

indicating that the scattering matrices are unitary. The column vectors form an orthonormal basis. An important property of orthonormal bases is that they are norm preserving [78]. For values $\rho \neq \frac{1}{2}$ this no longer applies and instead

$$\Phi_{\mathcal{S}_3}\widetilde{\Phi}_{\mathcal{S}_3}^* = \Phi_{\mathcal{P}_3}\widetilde{\Phi}_{\mathcal{P}_3}^* = I \tag{B.32}$$

where $\widetilde{\Phi}_{\mathcal{S}_3} = (\Phi_{\mathcal{S}_3}^*)^{-1}$ and $\widetilde{\Phi}_{\mathcal{P}_3} = (\Phi_{\mathcal{P}_3}^*)^{-1}$. The columns in $\Phi_{\mathcal{S}_3}$ form a basis and the columns in $\widetilde{\Phi}_{\mathcal{S}_3}$ form their dual. The same applies for the parallel adaptors. Together these basis form a biorthogonal bases pair. Biorthogonal basis-pairs are not generally norm preserving.

Appendix C

SPICE

Simulation Program with Integrated Circuit Emphasis, or SPICE for short, is a general purpose circuit simulation software developed at UC Berkley in the 1970s [33, 169]. It has been in continual development since then [34, 170] with various 3rd party implementations available, such as LTspice[1] or MacSpice[2]. SPICE is the de-facto software for doing circuit simulation in both industry and academia.

The SPICE2 simulator describes circuits based on Modified Nodal Analysis [51]

$$\underbrace{\begin{bmatrix} \mathbf{Y} & \mathbf{A} \\ \mathbf{B} & \mathbf{D} \end{bmatrix}}_{\text{MNA matrix } \mathbf{X}} \begin{bmatrix} \boldsymbol{v}_\text{n} \\ \boldsymbol{j} \end{bmatrix} = \begin{bmatrix} \boldsymbol{i}_\text{s} \\ \boldsymbol{e} \end{bmatrix} \tag{C.1}$$

$\mathbf{X}$ defines the relationship between node voltages $\boldsymbol{v}_\text{n}$, voltage source branch currents $\boldsymbol{j}$, current sources values $\boldsymbol{i}_\text{s}$ and voltage source values $\boldsymbol{e}$. The first row embodies Kirchoff's Current Law while the second row encode branch relationships, such that Kirchoff's Voltage Law is fulfilled. The MNA matrix $\mathbf{X}$ is automatically derived from a given circuit schematic which is written out in text form or drawn using a graphical user interface.

SPICE3, the circuit simulator employed in this thesis, works by using an implicit numerical integration method to transform nonlinear dynamic differential equations into nonlinear

[1] `http://linear.com/designtools/software`
[2] `http://www.macspice.com`

algebraic equations. These equations are then linearized using a modified Newton-Raphson iterative algorithm [171]. Finally a Gaussian elimination and sparse matrix techniques are used to obtain a solution [34]. The solution algorithm as used in SPICE3 is shown in Figure C.1.

Figure C.1 *SPICE Solution Algorithm* [34]

Appendix D

Scattering Matrices in Case Study

Below is a table containing links to the Matlab scripts that were used to derive the scattering matrices for each circuit in §5.

Table D.1 *Case Studies—Scattering Matrices*

Circuit Part	**Matlab script**
FET Booster	Link
Envelope Filter — Input Buffer	Link
Envelope Filter — Envelope Follower (Linear Section)	Link
Envelope Filter — Envelope Follower (Nonlinear Section)	Link
Envelope Filter — Filter (Linear Version)	Link
Envelope Filter — Filter (Nonlinear Version)	Link
Korg MS-20 Filter	Link

Bibliography

[1] David Te-Mao Yeh, Jonathan S. Abel, Andrei Vladimirescu, and Julius Orion Smith, "Numerical methods for simulation of guitar distortion circuits," *Computer Music Journal*, vol. 32, no. 2, pp. 23–42, 2008.

[2] Finn Agerkvist, "Volterra series based distortion effect," in *Audio Engineering Society Convention 129*, November 2010.

[3] Oliver Kröning, Kristjan Dempwolf, and Udo Zölzer, "Analysis and simulation of an analog guitar compressor," in *Proceedings of the 14th International Conference on Digital Audio Effects (DAFx-11)*, Paris, France, September 2011.

[4] Martin Holters and Udo Zölzer, "Physical modelling of a wah-wah effect pedal as a case study for application of the nodal DK method to circuits with variable parts," in *Proceedings of the 14th International Conference on Digital Audio Effects (DAFx-11)*, Paris, France, September 2011.

[5] Jaromir Macak, Jiri Schimmel, and Martin Holters, "Simulation of Fender type guitar preamp using approximation and state-space model," in *Proceedings of the 15th International Conference on Digital Audio Effects (DAFx-12)*, York, UK, September 2012.

[6] Ben Holmes and Maarten van Walstijn, "Improving the robustness of the iterative solver in state-space modelling of guitar distortion circuitry," in *Proceedings of the 18th International Conference on Digital Audio Effects (DAFx-15)*, Trondheim, Norway, November 2015.

[7] Felix Eichas, Marco Fink, and Udo Zölzer, "Feature design for the classification of audio effect units by input/output measurements," in *Proceedings of the 18th*

International Conference on Digital Audio Effects (DAFx-15), Trondheim, Norway, November 2015.

[8] Chet Gnegy and Kurt James Werner, "Digitizing the Ibanez Weeping Demon wah pedal," in *Proceedings of the 18th International Conference on Digital Audio Effects (DAFx-15)*, Trondheim, Norway, November 2015.

[9] Roope Kiiski, Fabián Esqueda, and Vesa Välimäki, "Time-variant gray-box modeling of a phaser pedal," in *Proceedings of the 19th International Conference on Digital Audio Effects (DAFx-16)*, Brno, Czech Republic, September 2016.

[10] Antonin Novak, Leo Guadagnin, Bertrand Lihoreau, Pierrick Lotton, Emmanuel Brasseur, and Laurent Simon, "Measurements and modeling of the nonlinear behavior of a guitar pickup at low frequencies," *Applied Sciences*, vol. 7, no. 1: 50, 2017.

[11] Matti Karjalainen and Jyri Pakarinen, "Wave digital simulation of a vacuum-tube amplifier," in *IEEE International Conference on Acoustics, Speech and Signal Processing (ICASSP-06)*, Toulouse, France, May 2006, vol. 5, pp. 153–156.

[12] Jyri Pakarinen and David Te-Mao Yeh, "A review of digital techniques for modeling vacuum-tube guitar amplifiers," *Computer Music Journal*, vol. 33, no. 2, pp. 85–100, 2009.

[13] Rafael Cauduro Dias de Paiva, Jyri Pakarinen, Vesa Välimäki, and Miikka Tikander, "Real-time audio transformer emulation for virtual tube amplifiers," *EURASIP Journal on Advances in Signal Processing*, 2011, Article ID 347645.

[14] William Ross Dunkel, Maximilian Rest, Kurt James Werner, Michael Jørgen Olsen, and Julius Orion Smith, "The Fender Bassman 5F6-A family of preamplifier circuits - A wave digital filter case study," in *Proceedings of the 19th International Conference on Digital Audio Effects (DAFx-16)*, Brno, Czech Republic, September 2016.

[15] Martin Holters and Udo Zölzer, "Circuit simulation with inductors and transformers based on the Jiles-Atherton model of magnetization," in *Proceedings of the 19th International Conference on Digital Audio Effects (DAFx-16)*, Brno, Czech Republic, September 2016.

[16] Tim Stilson and Julius Orion Smith, "Analyzing the Moog VCF with considerations for digital implementation," in *Proceedings of the International Computer Music Conference (ICMC-96)*, Hong Kong, August 1996.

[17] Antti Huovilainen, "Nonlinear digital implementation of the Moog ladder filter," in *Proceedings of the 7th International Conference on Digital Audio Effects (DAFx-04)*, Naples, Italy, October 2004.

[18] Thomas Hélie, "On the use of Volterra series for real-time simulations of weakly nonlinear analog audio devices: Application to the Moog ladder filter," in *Proceedings of the 9th International Conference on Digital Audio Effects (DAFx-06)*, Montreal, Canada, September 2006.

[19] Stefano D'Angelo and Vesa Välimäki, "An improved virtual analog model of the Moog ladder filter," in *IEEE International Conference on Acoustics, Speech and Signal Processing (ICASSP-13)*, May 2013, pp. 729–733.

[20] Jussi Pekonen, *Filter-based oscillator algorithms for virtual analog synthesis*, Ph.D. thesis, Aalto University, 2014.

[21] Fabián Esqueda, Stefan Bilbao, and Vesa Välimäki, "Aliasing reduction in clipped signals," *IEEE Transactions on Signal Processing*, vol. 64, no. 20, pp. 5255–5267, October 2016.

[22] Stefan Bilbao, *Wave and scattering methods for numerical simulation*, John Wiley & Sons, 2004.

[23] Julian D. Parker, *Dispersive systems in musical audio signal processing*, Ph.D. thesis, Aalto University, 2013.

[24] Vesa Välimäki, Federico Fontana, Julius Orion Smith, and Udo Zölzer, "Introduction to the special issue on virtual analog audio effects and musical instruments," *IEEE Transactions on Audio, Speech and Language Processing*, vol. 18, no. 4, pp. 713–714, 2010.

[25] Vesa Välimäki, Stefan Bilbao, Julius Orion Smith, Jonathan S. Abel, Jyri Pakarinen, and David Berners, "Virtual analog effects," in *DAFX: Digital Audio Effects*, pp. 473–522. John Wiley & Sons Ltd, Chichester, UK, 2nd edition, March 2011.

[26] Jussi Pekonen and Vesa Välimäki, "The brief history of virtual analog synthesis," in *Proceedings of the Forum Acusticum*, Aalborg, Denmark, June 2011, pp. 461–466.

[27] Jyri Pakarinen, Vesa Välimäki, Federico Fontana, Victor Lazzarini, and Jonathan S. Abel, "Recent advances in real-time musical effects, synthesis, and virtual analog models," *EURASIP Journal on Advances in Signal Processing*, 2011, Article ID 940784.

[28] Albert Smith Jackson, *Analog Computation*, McGraw-Hill, New York, 1960.

[29] Floyd A. Firestone, "A new analogy between mechanical and electrical systems," *The Journal of the Acoustical Society of America*, vol. 4, no. 3, pp. 249–267, 1933.

[30] Harry Ferdinand Olson, *Dynamical Analogies*, D. Van Nostrand Company, 1943.

[31] Vitold Belevitch, "Summary of the history of circuit theory," *Proceedings of the IRE*, vol. 50, no. 5, pp. 848–855, 1962.

[32] John Eargle, *Loudspeaker Handbook*, Springer US, Boston, MA, 2003.

[33] Laurence W. Nagel and Donald Oscar Pederson, "SPICE (simulation program with integrated circuit emphasis)," Tech. Rep. UCB/ERL M382, EECS Department, University of California, Berkeley, April 1973.

[34] Andre Vladimirescu, *The SPICE book*, John Wiley & Sons, Inc., 1994.

[35] Alfred Fettweis, "Wave digital filters: Theory and practice," *Proceedings of the IEEE*, vol. 74, no. 2, pp. 270–327, 1986.

[36] Jyri Pakarinen, Matti Karjalainen, Vesa Välimäki, and Stefan Bilbao, "Energy behavior in time-varying fractional delay filters for physical modeling synthesis of musical instruments," in *IEEE International Conference on Acoustics, Speech, and Signal Processing (ICASSP-05)*, Pennsylvania, USA, March 2005.

[37] Giovanni De Sanctis and Augusto Sarti, "Virtual analog modeling in the wave-digital domain," *IEEE Transactions on Audio, Speech and Language Processing*, vol. 18, no. 4, pp. 715–727, 2010.

[38] Matti Karjalainen, "Efficient realization of wave digital components for physical modeling and sound synthesis," *IEEE Transactions on Audio, Speech and Language Processing*, vol. 16, no. 5, pp. 947–956, 2008.

[39] Bhunesh Kumar and Naeem Ahmad, "Studies on circulator-tree wave digital filters," M.S. thesis, Linköping University, 2009.

[40] Giovanni De Sanctis and Augusto Sarti, "Virtual analog modeling in the wave-digital domain," *IEEE Transactions on Audio, Speech and Language Processing*, vol. 18, no. 4, pp. 715–727, 2010.

[41] Peter Raffensperger, "Toward a wave digital filter model of the Fairchild 670 limiter," in *Proceedings of the 15th International Conference on Digital Audio Effects (DAFx-12)*, York, UK, September 2012.

[42] Stefano D'Angelo and Vesa Välimäki, "Wave-digital polarity and current inverters and their application to virtual analog audio processing," in *IEEE International Conference on Acoustics, Speech and Signal Processing (ICASSP-12)*, Kyoto, Japan, March 2012, pp. 469–472.

[43] Kurt James Werner, Vaibhav Nangia, Julius Orion Smith, and Jonathan S. Abel, "Resolving wave digital filters with multiple/multiport nonlinearities," in *Proceedings of the 18th International Conference on Digital Audio Effects (DAFx-15)*, Trondheim, Norway, November 2015.

[44] Kurt James Werner, Julius Orion Smith, and Jonathan S. Abel, "Wave digital filter adaptors for arbitrary topologies and multiport linear elements," in *Proceedings of the 18th International Conference on Digital Audio Effects (DAFx-15)*, Trondheim, Norway, November 2015.

[45] Kurt James Werner, William Ross Dunkel, Maximilian Rest, Michael Jørgen Olsen, and Julius Orion Smith, "Wave digital filter modeling of circuits with operational amplifiers," in *24th European Signal Processing Conference (EUSIPCO-16)*, Budapest, Hungary, August 2016, pp. 1033–1037.

[46] Alberto Bernardini and Augusto Sarti, "Dynamic adaptation of instantaneous nonlinear bipoles in wave digital networks," in *24th European Signal Processing Conference (EUSIPCO-16)*, Budapest, Hungary, August 2016, pp. 1038–1042.

[47] Alberto Bernardini and Augusto Sarti, "Biparametric wave digital filters," *IEEE Transactions on Circuits and Systems I: Regular Papers*, vol. 64, no. 7, pp. 1826–1838, July 2017.

[48] R. P. Sallen and E. L. Key, "A practical method of designing RC active filters," *IRE Transactions on Circuit Theory*, vol. 2, no. 1, pp. 74–85, March 1955.

[49] David Te-Mao Yeh and Julius Orion Smith, "Discretization of the '59 Fender Bassman tone stack," in *Proceedings of the 9th International Conference on Digital Audio Effects (DAFx-06)*, Montreal, Canada, September 2006.

[50] François Germain, "A nonlinear analysis framework for electronic synthesizer circuits," M.A. Music Technology thesis, McGill University, 2011.

[51] Chung-Wen Ho, Albert E. Ruehli, and Pierce A. Brennan, "The modified nodal approach to network analysis," *IEEE Transactions on Circuits and Systems*, vol. 22, no. 6, pp. 504–509, 1975.

[52] David T. Westwick and Robert E. Kearney, *Identification of Nonlinear Physiological Systems*, IEEE Biomedical Engineering Book Series. IEEE Press/Wiley, 2003.

[53] Arie J. M. Kaizer, "Modeling of the nonlinear response of an electrodynamic loudspeaker by a Volterra series expansion," *Journal of the Audio Engineering Society*, vol. 35, pp. 421–433, 1987.

[54] Thomas Hélie, "Volterra series and state transformation for real-time simulations of audio circuits including saturations: Application to the Moog ladder filter," *IEEE Transactions on Audio, Speech, and Language Processing*, vol. 18, no. 4, pp. 747–759, May 2010.

[55] Vitold Belevitch, *Classical Network Theory*, San Francisco, Holden-Day, 1968.

[56] François Germain and Kurt James Werner, "Design principles for lumped model discretisation using Möbius transforms," in *Proceedings of the 18th International Conference on Digital Audio Effects (DAFx-15)*, Trondheim, Norway, November 2015.

[57] Korg Electronic Laboratory Corporation, "MS-20 service notes," Tech. Rep., 1978.

[58] Julius Orion Smith, "Physical modeling synthesis update," *Computer Music Journal*, vol. 20, no. 2, pp. 44–56, 1996.

[59] Michael J. Kemp, "Analysis and simulation of non-linear audio processes using finite impulse responses derived at multiple impulse amplitudes," in *Audio Engineering Society Convention 106*, May 1999.

[60] Andrea Primavera, Stefania Cecchi, Laura Romoli, Michele Gasparini, and Francesco Piazza, "Approximation of dynamic convolution exploiting principal component analysis: Objective and subjective quality evaluation," in *Audio Engineering Society Convention 133*, October 2012.

[61] Juhan Nam, Vesa Välimäki, Jonathan S. Abel, and Julius Orion Smith, "Efficient antialiasing oscillator algorithms using low-order fractional delay filters," *IEEE Transactions on Audio, Speech, and Language Processing*, vol. 18, no. 4, pp. 773–785, May 2010.

[62] Fabián Esqueda, Henri Pöntynen, Vesa Välimäki, and Julian D. Parker, "Virtual analog Buchla 259 wavefolder," in *Proceedings of the 20th International Conference on Digital Audio Effects (DAFx-17)*, Edinbugh, Scottland, September 2017.

[63] Norbert Wiener, *Nonlinear Problems in Random Theory*, The MIT Press, Cambridge, Massachusetts, USA, August 1958.

[64] Stephen Boyd and Leon O. Chua, "Fading memory and the problem of approximating nonlinear operators with Volterra series," *IEEE Transactions on Circuits and Systems*, vol. 32, no. 11, pp. 1150–1161, 1985.

[65] Angelo Farina, "Advancements in impulse response measurements by sine sweeps," in *Audio Engineering Society Convention 122*, May 2007.

[66] François Germain, Jonathan S. Abel, Philippe Depalle, and Marcelo M. Wanderley, "Uniform noise sequences for nonlinear system identification," York, UK, September 2012, pp. 15–18.

[67] Enrico Armelloni, Alberto Bellini, and Angelo Farina, "Not-linear convolution: A new approach for the auralization of distorting systems," in *Audio Engineering Society Convention 110*, May 2001.

[68] Antonin Novak, Balbine Maillou, Pierrick Lotton, and Laurent Simon, "Nonparametric identification of nonlinear systems in series," *IEEE Transactions on Instrumentation and Measurement*, vol. 63, no. 8, pp. 2044–2051, August 2014.

[69] Antonin Novak, Pierrick Lotton, and Laurent Simon, "Synchronized swept-sine: Theory, application, and implementation," *Journal of the Audio Engineering Society*, vol. 63, no. 10, pp. 786–798, 2015.

[70] Antonin Novak, Laurent Simon, and Pierrick Lotton, "Extension of Generalized Hammerstein model to non-polynomial inputs," in *24th European Signal Processing Conference (EUSIPCO-16)*, Budapest, Hungary, August 2016, pp. 21–25.

[71] Jörn Schattschneider and Udo Zölzer, "Discrete-time models for nonlinear audio systems," in *Proceedings of the 2nd International Conference on Digital Audio Effects (DAFx-99)*, Trondheim, Norway, December 1999.

[72] Antonin Novak, Laurent Simon, Pierrick Lotton, and Joël Gilbert, "Chebyshev model and synchronized swept sine method in nonlinear audio effect modeling," in *Proceedings of the 13th International Conf. on Digital Audio Effects (DAFx-10)*, Graz, Austria, September 2010.

[73] Rafael Cauduro Dias de Paiva, Jyri Pakarinen, and Vesa Välimäki, "Reduced-complexity modeling of high-order nonlinear audio systems using swept-sine and principal component analysis," in *Audio Engineering Society Conference: 45th International Conference: Applications of Time-Frequency Processing in Audio*, Helsinki, Finland, March 2012.

[74] David Te-Mao Yeh, Balázs Bank, and Matti Karjalainen, "Nonlinear modeling of a guitar loudspeaker cabinet," in *Proceedings of the 11th International Conference on Digital Audio Effects (DAFx-08)*, Espoo, Finland, September 2008.

[75] Felix Eichas and Udo Zölzer, "Modeling of an optocoupler-based audio dynamic range control circuit," in *SPIE Proceedings*, California, United States, September 2016, vol. 9948.

[76] David Te-Mao Yeh, John Nolting, and Julius Orion Smith, "Physical and behavioral circuit modeling of the SP-12 sampler," in *Proceedings of the International Computer Music Conference (ICMC-07)*, Copenhagen, Denmark, August 2007.

[77] David Te-Mao Yeh, Jonathan S. Abel, and Julius Orion Smith, "Simplified, physically-informed models of distortion and overdrive guitar effects pedals," in *Proceedings of the 10th International Conference on Digital Audio Effects (DAFx-07)*, Bordeaux, France, September 2007.

[78] Martin Vetterli, Jelena Kovačević, and Vivek K. Goyal, *Foundations of Signal Processing*, Cambridge University Press, 2014, Available online at `http://fourierandwavelets.org/`. Last accessed January 22, 2017.

[79] Jean Laroche, "On the stability of time-varying recursive filters," *Journal of the Audio Engineering Society*, vol. 55, no. 6, pp. 460–471, 2007.

[80] Aaron Wishnick, "Time-varying filters for musical applications," in *Proceedings of the 17th International Conference on Digital Audio Effects (DAFx-14)*, Erlangen, Germany, September 2014.

[81] Karl Johan Åstrom and Richard M. Murray, *Feedback Systems: An Introduction for Scientists and Engineers*, Princeton University Press, Princeton, NJ, USA, 2nd edition, 2012.

[82] Denis Matignon, Philippe Depalle, and Xavier Rodet, "State space models for wind-instrument synthesis," in *Proceedings International Computer Music Conference (ICMC-92)*, San Jose, USA, October 1992.

[83] Gianpaolo Borin, Giovanni De Poli, and Davide Rocchesso, "Elimination of delay-free loops in discrete-time models of nonlinear acoustic systems," *IEEE Transactions on Speech and Audio Processing*, vol. 8, no. 5, pp. 597–604, 2000.

[84] Kristjan Dempwolf, Martin Holters, and Udo Zölzer, "Discretization of parametric analog circuits for real-time simulations," in *Proceedings of the 13th International Conference on Digital Audio Effects (DAFx-10)*, Graz, Austria, September 2010.

[85] David Te-Mao Yeh, *Digital Implementation of Musical Distortion Circuits by Analysis and Simulation*, Ph.D. thesis, Stanford University, 2009.

[86] David Te-Mao Yeh, Jonathan S. Abel, and Julius Orion Smith, "Automated physical modeling of nonlinear audio circuits for real-time audio effects - Part I: Theoretical development," *IEEE Transactions on Audio, Speech and Language Processing*, vol. 18, no. 4, pp. 728–737, 2010.

[87] Felix Eichas, Marco Fink, Martin Holters, and Udo Zölzer, "Physical modeling of the MXR Phase 90 guitar effect pedal," in *Proceedings of the 17th International Conference on Digital Audio Effects (DAFx-14)*, Erlangen, Germany, September 2014, pp. 153–158.

[88] Martin Holters and Udo Zölzer, "A generalized method for the derivation of non-linear state-space models from circuit schematics," in *Proceedings of the 23rd European Signal Processing Conference (EUSIPCO)*, Nice, France, 2015, pp. 1078–1082.

[89] Gary D. Hachtel, Robert K. Brayton, and Fred G. Gustavson, "The sparse tableau approach to network analysis and design," *IEEE Transactions on Circuit Theory*, vol. 18, no. 1, pp. 101–113, January 1971.

[90] Arjan van der Schaft, *Port-Hamiltonian systems: An introductory survey*, pp. 1339–1365, European Mathematical Society Publishing House, 2006.

[91] Nicolas Lopes, Thomas Hélie, and Antoine Falaize, "Explicit second-order accurate method for the passive guaranteed simulation of Port-Hamiltonian systems," in *5th IFAC Workshop on Lagrangian and Hamiltonian Methods for Nonlinear Control*, Lyon, France, 2015, vol. 28, pp. 223–228.

[92] Antoine Falaize and Thomas Hélie, "Guaranteed-passive simulation of an electro-mechanical piano: A Port-Hamiltonian approach," in *Proceedings of the 18th International Conference on Digital Audio Effects (DAFx-15)*, Trondheim, Norway, November 2015.

[93] Antoine Falaize and Thomas Hélie, "Passive simulation of the nonlinear Port-Hamiltonian modeling of a Rhodes piano," *Journal of Sound and Vibration*, vol. 390, pp. 289–309, 2017.

[94] Antoine Falaize and Thomas Hélie, "Simulation of an analog circuit of a wah pedal: A port-hamiltonian approach," in *Audio Engineering Society Convention 135*, October 2013.

[95] Antoine Falaize and Thomas Hélie, "Passive guaranteed simulation of analog audio circuits: A Port-Hamiltonian approach," *Applied Sciences*, vol. 6, no. 10, pp. 273, 2016.

[96] Antoine Falaize, Nicolas Lopes, Thomas Hélie, Denis Matignon, and Bernhard Maschke, "Energy-balanced models for acoustic and audio systems: A Port-Hamiltonian approach," in *Unfold Mechanics for Sounds and Music*, Paris, France, September 2014.

[97] Antoine Falaize and Thomas Hélie, "Passive simulation of electrodynamic loudspeakers for guitar amplifiers: A Port-Hamiltonian approach," in *International Symposium on Musical Acoustics*, Le Mans, France, July 2014.

[98] Antoine Falaize, Nicolas Papazoglou, Thomas Hélie, and Nicolas Lopes, "Compensation of loudspeaker's nonlinearities based on flatness and Port-Hamiltonian approach," in *22ème Congrès Français de Mécanique*, Lyon, France, Aug. 2015.

[99] Sophocles Orfanidis, *Electromagnetic Waves and Antennas*, Rutgers University, New Jersay, 2016, Available online at `http://www.ece.rutgers.edu/~orfanidi/ewa`. Last accessed August 22, 2017.

[100] Alfred Fettweis, "German patent 2027303," First filled in West Germany, June 3, 1970.

[101] Alfred Fettweis, "Pseudopassivity, sensitivity and stability of wave digital filters," *IEEE Transactions on Circuit Theory*, vol. 19, no. 6, pp. 668–673, 1972.

[102] Alfred Fettweis, "Reciprocity, inter-reciprocity, and transposition in wave digital filters," *International Journal of Circuit Theory and Applications*, vol. 1, no. 4, pp. 323–337, 1973.

[103] Alfred Fettweis and Klaus Meerkötter, "On adaptors for wave digital filters," *IEEE Transactions on Acoustics, Speech, and Signal Processing*, vol. 23, no. 6, pp. 516–525, December 1975.

[104] Alfred Fettweis and Klaus Meerkötter, "Suppression of parasite oscillations in multidimensional wave digital filters," *IEEE Transactions on Circuits and Systems*, vol. 25, no. 12, pp. 1060–1066, 1975.

[105] Alfred Fettweis, "Multidimensional wave digital filters," in *European Conference on Circuit Theory and Design*, Genova, Italy, 1976, pp. 409–416.

[106] Alfred Fettweis, *Digital Signal Processing*, chapter Principles of multidimensional wave digital filtering, pp. 261–282, Western Periodicals, California, USA, 1978.

[107] Julius Orion Smith, "Waveguide filter tutorial," in *International Computer Music Conference (ICMC-87)*, Köln, Germany, 1987, pp. 9–16.

[108] Julius Orion Smith, "Physical modeling using digital waveguides," *Computer Music Journal*, vol. 16, no. 4, pp. 74, 1992.

[109] Scott A. Van Duyne, John R. Pierce, and Julius Orion Smith III, "Traveling wave implementation of a lossless mode-coupling filter and the wave digital hammer," in *Proceedings of the International Computer Music Conference (ICMC-94)*, Aarhus, Denmark, 1994, pp. 411–418.

[110] Stefan Bilbao, Julien Bensa, Richard Kronland-Martinet, and Julius Orion Smith, "The wave digital piano hammer: A passive formulation," in *Proceedings of the 144th meeting of the Acoustical Society of America*, Cancun, Mexico, December 2002.

[111] Maarten van Walstijn and Gary Scavone, "The wave digital tonehole model," in *Proceedings of the International Computer Music Conference (ICMC-00)*, Berlin, Germany, 2000, pp. 465–468.

[112] Stefano D'Angelo, Jyri Pakarinen, and Vesa Välimäki, "New family of wave-digital triode models," *IEEE Transactions on Audio, Speech and Language Processing*, vol. 21, no. 2, pp. 313–321, 2013.

[113] Tim Schwerdtfeger and Anton Kummert, "A multidimensional processing approach to wave digital filters with topology-related delay-free loops," in *IEEE International Conference on Acoustics, Speech and Signal Processing (ICASSP-14)*, Florence, Italy, May 2014, pp. 389–393.

[114] Alberto Bernardini, Kurt James Werner, Augusto Sarti, and Julius Orion Smith, "Modeling nonlinear wave digital elements using the Lambert function," *IEEE Transactions on Circuits and Systems I: Regular Papers*, vol. 63, no. 8, pp. 1231–1242, 2016.

[115] Bernard D. H. Tellegen, "A general network theorem with applications," *Philips Research Reports*, vol. 7, pp. 259–269, 1952.

[116] Kurt James Werner, *Virtual analog modeling of audio circuitry using wave digital filters*, Ph.D. thesis, Stanford University, 2016.

[117] Stefan Bilbao, *Wave and Scattering Methods for the Numerical Integration of Partial Differential Equations*, Ph.D. thesis, Stanford University, 2001.

[118] Tristan Needham, *Visual Complex Analysis*, Oxford University Press, 1998.

[119] Vesa Välimäki, Jyri Pakarinen, Cumhur Erkut, and Matti Karjalainen, "Discrete-time modelling of musical instruments," *Reports on Progress in Physics*, vol. 69, no. 1, pp. 1–78, 2005.

[120] Dietrich Fränken, Jörg Ochs, and Karlheinz Ochs, "Generation of wave digital structures for connection networks containing ideal transformers," in *Proceedings of the 2003 International Symposium on Circuits and Systems (ISCAS-03)*, May 2003, vol. 3, pp. 240–243.

[121] Dietrich Fränken, Jörg Ochs, and Karlheinz Ochs, "Generation of wave digital structures for networks containing multiport elements," *IEEE Transactions on Circuits and Systems I: Regular Papers*, vol. 52, no. 3, pp. 586–596, March 2005.

[122] Augusto Sarti and Giovanni De Sanctis, "Systematic methods for the implementation of nonlinear wave-digital structures," *IEEE Transactions on Circuits and Systems I: Regular Papers*, vol. 56, no. 2, pp. 460–472, February 2009.

[123] G. O. Martens and Klaus Meerkötter, "On N-port adaptors for wave digital filters with application to a bridged-tee filter," in *Proceedings of the IEEE International Symposium on Circuits and Systems (ISCAS-76)*, Munich, Germany, April 1976, pp. 514–517.

[124] Klaus Meerkötter and Reinhard Scholz, "Digital simulation of nonlinear circuits by wave digital filter principles," in *IEEE International Symposium on Circuits and Systems (ISCAS)*, Portland, Oregon, May 1989, vol. 1, pp. 720–723.

[125] Stefan Petrausch and Rudolf Rabenstein, "Wave digital filters with multiple nonlinearities," in *Proceedings of the 12th European Signal Processing Conference (EUSIPCO-04)*, Vienna, Austria, September 2004, pp. 77–80.

[126] Jyri Pakarinen and Matti Karjalainen, "Enhanced wave digital triode model for real-time tube amplifier emulation," *IEEE Transactions on Audio Speech and Language Processing*, vol. 18, no. 4, pp. 738–746, May 2010.

[127] Klaus Meerkötter and Thomas Felderhoff, "Simulation of nonlinear transmission lines by wave digital filter principles," in *IEEE International Symposium on Circuits and Systems (ISCAS-92)*, May 1992, vol. 2, pp. 875–878.

[128] Tim Schwerdtfeger and Anton Kummert, "Newton's method for modularity-preserving multidimensional wave digital filters," in *2015 IEEE 9th International Workshop on Multidimensional (nD) Systems (nDS)*, September 2015.

[129] Michael Jørgen Olsen, Kurt James Werner, and Julius Orion Smith, "Resolving grouped nonlinearities in wave digital filters using iterative techniques," in *Proceedings of the 19th International Conference on Digital Audio Effects (DAFx-16)*, Brno, Czech Republic, September 2016.

[130] Adi Ben-Israel, "A Newton-Raphson method for the solution of systems of equations," *Journal of Mathematical analysis and applications*, vol. 15, no. 2, pp. 243–252, 1966.

[131] Ólafur Bogason and Kurt James Werner, "Modeling circuits with operational transconductance amplifiers using wave digital filters," in *Proceedings of the 20th International Conference on Digital Audio Effects (DAFx-17)*, Edinburgh, UK, September 2017, pp. 130–137.

[132] Hans Werner Strube, "Time-varying wave digital filters for modeling analog systems," *IEEE Transactions on Acoustics, Speech, and Signal Processing*, vol. 30, no. 6, pp. 864–868, December 1982.

[133] Hans Werner Strube, "Time-varying wave digital filters and vocal-tract models," in *IEEE International Conference on Acoustics, Speech, and Signal Processing (ICASSP-82)*, Paris, France, May 1982, pp. 923–926.

[134] Gernot Kubin, "Wave digital filters: Voltage, current, or power waves?," in *IEEE International Conference on Acoustics, Speech, and Signal Processing (ICASSP-85)*, Tampa, Florida, April 1985, pp. 69–72.

[135] Gernot Kubin, "On the stability of wave digital filters with time-varying coefficients," in *Proceedings of the European Conference on Circuit Theory and Design (ECCTD-85)*, Prague, Czecho-Slovakia, September 1985, pp. 499–502.

[136] Stefan Bilbao, "Time-varying generalizations of all-pass filters," *IEEE Signal Processing Letters*, vol. 12, no. 5, pp. 376–379, 2005.

[137] Parviz Moin, *Fundamentals of Engineering Numerical Analysis*, Cambridge University Press, Cambridge, 2nd edition, 2010.

[138] François Germain and Kurt James Werner, "Joint parameter optimization of differentiated discretization schemes for audio circuits," in *Audio Engineering Society Convention 142*, May 2017.

[139] Julius Orion Smith, *Physical Audio Signal Processing*, W3K Publishing, 2010.

[140] Bengt Lindberg, "On smoothing and extrapolation for the trapezoidal rule," *Bit*, vol. 11, no. 1, pp. 29–52, 1971.

[141] Wenzhong Gao, Eugene Solodovnik, Roger Dougal, George Cokkinides, and A. P. Sakis Meliopoulos, "Elimination of numerical oscillations in power system dynamic simulation," in *19th Annual IEEE Applied Power Electronics Conference and Exposition (APEC-03)*, Miami Beach, Florida, February 2003, pp. 790–794.

[142] Alfred Fettweis, "Robust numerical integration using wave digital concepts," in *Proceedings of the 5th DSPS Educators Conference*, Tokyo, Japan, September 2003, pp. 23–32.

[143] Kurt James Werner, Vaibhav Nangia, Alberto Bernardini, Julius Orion Smith, and Augusto Sarti, "An improved and generalized diode clipper model for wave digital filters," in *Audio Engineering Society Convention 139*, October 2015.

[144] Maximilian Rest, William Ross Dunkel, Kurt James Werner, and Julius Orion Smith, "RT-WDF - a modular wave digital filter library with support for arbitrary topologies and multiple nonlinearities," in *Proceedings of the 19th International Conference on Digital Audio Effects (DAFx-16)*, Brno, Czech Republic, 2016, pp. 287–294.

[145] Roland Corporation, "SH-101 service notes," Tech. Rep., 1982.

[146] Julian Parker and Stefano D'Angelo, "A digital model of the Buchla Lowpass-Gate," in *Proceedings of the 16th International Conference on Digital Audio Effects (DAFx-13)*, Maynooth, Ireland, September 2013.

[147] Adel S. Sedra and Kenneth C. Smith, *Microelectronic Circuits*, Oxford University Press, New York, 6th edition, 2015.

[148] Rafael Cauduro Dias de Paiva, Stefano D'Angelo, Jyri Pakarinen, and Vesa Välimäki, "Emulation of operational amplifiers and diodes in audio distortion circuits," *IEEE Transactions on Circuits and Systems II: Express Briefs*, vol. 59, no. 10, pp. 688–692, October 2012.

[149] W. Shockley, "Transistor electronics: Imperfections, unipolar and analog transistors*," *Proceedings of the IRE*, vol. 40, no. 11, pp. 1289–1313, 1952.

[150] Michael Deveney, "A temperature dependent SPICE macro-model for Zener and avalanche diodes," in *Proceedings of the 34th Midwest Symposium on Circuits and Systems*, Monterey, CA, USA, May 1991, vol. 2, pp. 592–596.

[151] Silphy Wong and Chen Min Hu, "SPICE macro model for the simulation of Zener diode i-v characteristics," *IEEE Circuits and Devices Magazine*, vol. 7, no. 4, pp. 9–12, 1991.

[152] Antti Huovilainen, "Enhanced digital models for analog modulation effects," in *Proceedings of the 8th International Conference on Digital Audio Effects (DAFx-05)*, Madrid, Spain, September 2005, pp. 155–160.

[153] Eric Barbour, "The cool sound of tubes," *IEEE Spectrum*, vol. 35, no. 8, pp. 24–35, 1998.

[154] Timothy E. Stinchcombe, "A study of the Korg MS-10 and MS-20 filters," Tech. Rep., 2009, Available online at `http://www.timstinchcombe.co.uk/synth/MS20_study.pdf`. Last accessed October 8, 2017.

[155] Harold Shichman and David Hodges, "Modeling and simulation of insulated field-effect transistor switching circuits," *Solid-State Circuits*, vol. 3, no. 3, pp. 285–289, 1968.

[156] Tahira Parveen, *Textbook of Operational Transconductance Amplifier and Analog Integrated Circuits*, I.K. International Publishing House Pvt Ltd., New Dehli, India, 2009.

[157] C. Acar, F. Anday, and H. Kuntman, "On the realization of OTA-C filters," *International J. Circuit Theory and Appl.*, vol. 21, pp. 331–341, 1993.

[158] Hakan Kuntman, "Simple and accurate nonlinear OTA macromodel for simulation of CMOS OTA-C active filters," *International Journal of Electronics*, vol. 77, no. 6, pp. 993–1006, 1994.

[159] Texas Instruments, "LM13700 datasheet," Tech. Rep., 1999.

[160] Randall L. Geiger and Edgar Sanchez-Sinencio, "Active filter design using operational transconductance amplifiers: A tutorial," *IEEE Circuits and Devices Magazine*, vol. 1, no. 2, pp. 20–32, 1985.

[161] Achim Gratz, "Operational transconductance amplifiers," Tech. Rep., 2008, Available online at `http://synth.stromeko.net/diy/OTA.pdf`. Last accessed April 1, 2017.

[162] Ray Marston, "Understanding and using OTA op-amp ICs, part 1," *Nuts and Volts*, , no. April, pp. 58–62, 2003.

[163] Alex Petrini, "DOD FX25 - Autowah," Blog Post, January 2006, Available online at `http://topopiccione.atspace.com/PJ11DODfx25.html`. Last accessed September 19, 2017.

[164] Leonard T. Bruton, *RC-Active Circuits*, Prentice-Hall Inc., Englewood Cliffs, New Jersey, 1980.

[165] Ali Bekir Yildiz, "Modified nodal analysis-based determination of transfer functions for multi-inputs multi-outputs linear circuits," *Automatika*, vol. 51, no. 4, pp. 353–360, 2010.

[166] Maximilian Rest, Julian D. Parker, and Kurt James Werner, "WDF modeling of a Korg MS-50 based non-linear diode bridge VCF," in *Proceedings of the 20th International Conference on Digital Audio Effects (DAFx-17)*, Edinburgh, UK, September 2017, pp. 145–151.

[167] Germund G. Dahlquist, "A special stability problem for linear multistep methods," *BIT Numerical Mathematics*, vol. 3, no. 1, pp. 27–43, 1963.

[168] H. Carlin, "Singular network elements," *IEEE Transactions on Circuit Theory*, vol. 11, no. 1, 1964.

[169] Laurence W. Nagel, *SPICE2: A Computer Program to Simulate Semiconductor Circuits*, Ph.D. thesis, EECS Department, University of California, Berkeley, 1975.

[170] Thomas L. Quarles, *Analysis of Performance and Convergence Issues for Circuit Simulation*, Ph.D. thesis, EECS Department, University of California, Berkeley, 1989.

[171] Richard L. Burden and John Douglas Faires, *Numerical Analysis*, Brooks/Cole Cengage Learning, Boston, MA, USA, 9th edition, 2011.